Diplomarbeit

Advanced Regenerator

A Countercurrent fluidized Bed Regenerator utilizing a Pressure Gradient for Powder Transport

Ausgeführt zum Zwecke der Erlangung des akademischen Grades eines Diplom-Ingenieurs

unter der Leitung von

Univ.Prof. Dipl.Ing. Dr.techn. Markus Haider

E302

Institut für Energietechnik und Thermodynamik

eingereicht an der Technischen Universität Wien

Fakultät für Maschinenwesen und Betriebswissenschaften

von

David Wünsch

E 066 445 - 0925954

Dempschergasse 9/12, 1180 Wien

Wien, am 20. Oktober 2016

I would like to thank Prof. Markus Haider for his trust and tireless support in spite of his own overworked state, Dipl.Ing. Verena Sulzgruber for her incredible help in translating even my most horrid ideas into an actual apparatus layout, Dr. Karl Schwaiger for sharing his indispensable know-how regarding the topic at hand and thus enabling a fast start that would have been impossible otherwise, Dr. Heimo Walter for his taciturn but impressively clever inputs and ideas, Dr. Andreas Werner for sharing his grave experience and thus cutting long thoughts pleasantly short, Dipl.Ing. Peter Steiner for a patient and stable link to an exhausted *SandTES* team and it's knowledge, the rest of that exact team for their patience, Ing. Andreas Hofer for *just doing his job*, my parents for reasons I do not need to explain and last but not least Mag. Katharina Trieb for her *Love*

Abstract

Renewables should become more continuously available, reliable and cost efficient, while conventional sources and large consumers of heat and electricity should be more flexible and energy efficient - in turn relieving sources - to overcome the energy revolution. *Thus process and constructional layouts of two test benches for experimental validation of a concept called the* Advanced Regenerator - *a highly flexible, short to long term fluidized bed regenerative heat storage utilizing a pressure gradient for hot powder transport and hence enabling minimal losses, high energy densities, compact construction and countercurrent heat exchange - are performed in this thesis. Such devices in decentralized setup - being included in every energy- and especially heat-intensive industry, storing heat or power-to-heat while electricity prices are low and again returning heat to temporally displaced processes or returning* ≈ 30 % *electricity with Stirling engines, where heat is not needed - can well achieve above stated goals.*

The means for those steps performed are analytic process and thermodynamic rough layout calculations, Computational Particle Fluid Dynamics (CPFD) software and the programming languages Matlab *and* Python *for coding. In the process a method enabling a convenient co-simulation of an* Advanced Regenerator *with a controller script adjusting a CPFD software is developed forming the basis for design geometry and execution of further partially automated and controlled simulations.*

Contents

1. Introduction

In the course of the energy transition the european electrical energy industry and especially older and conventional power plants suffer from ever higher efficiency, flexibility and emission demands posed by the public and in growing measure also by legislation. As the two-degrees-scenario (2DS), formerly proposed by the *International Energy Agency* (IEA), that is to limit global warming to a maximum of two degrees celsius (preferably 1.5 $°C$) was approved by the vast majority of CO_2 producing countries on December 12th 2015, reinforced efforts to reduce emissions (especially CO_2) are expected. The *European Union* (EU) set a total reduction of greenhouse gas emissions goal of 20 percent until 2020 and 80 percent until 2050. A worldwide comparison of the energy mix today with a possible 2DS Scenario in 2050 including a massive increase of temporally unreliable renewable energy sources is to be seen in **figure 1.1**.

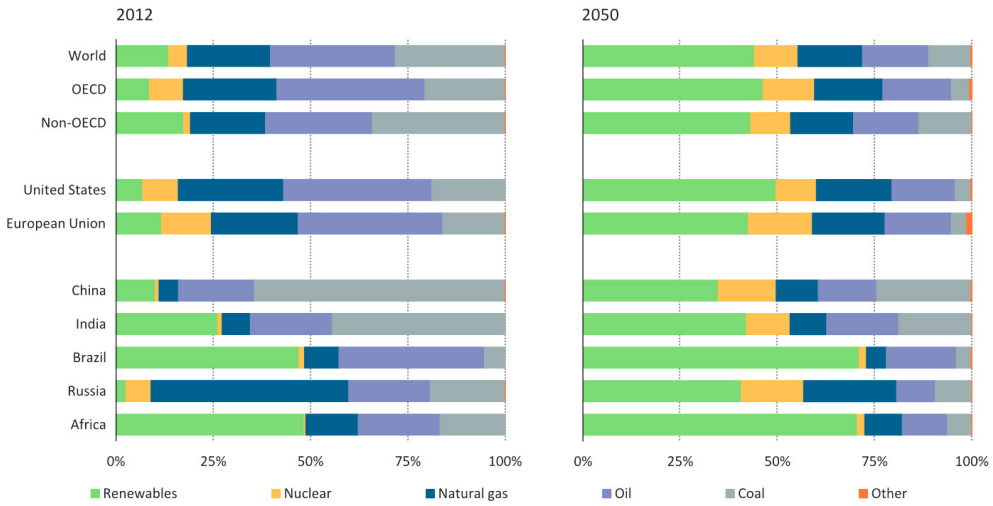

Figure 1.1.: Comparison of the energy mix today with a possible 2DS Scenario in 2050, the massive increase of renewable energy sources is to be seen, IEA [1]

All of this has to be achieved, while world wide electrical energy consumption is ever increasing at high rates, as shown in **figure 1.2**, thus a grave technological and economical impact is to be expected, no matter if the goal will be actually accomplished or not. This inter alia means the energy-intensive industries have to become more flexible and more efficient in terms of energy storage and heat integration to maintain a stable grid and decrease CO_2 emissions at the same time. See **section 1.2** for a more detailed explanation. Thus the subject of this thesis is the procedural, fluidic and constructional layout of a concept called the *Advanced Regenerator* - a short to long term, low to medium capacity heat storage with fast reaction times. Furthermore this work has the goal of developing a method enabling a convenient co-simulation of the *Advanced Regenerator* with a controller script and a CPFD software. The focus is on the fluidic, procedural and constructional layout of a test bench geometry for cold (not heated or cooled) experimental validation of the AR concept as well as simulation results and a convenient method for co-simulation enabling future work by colleagues. The means for these steps were analytic procedural and thermodynamic rough layout calculations, *Computational Particle Fluid Dynamics* (CPFD) software and the programming languages *Matlab* and *Python* for coding. The Concept itself will be explained in **section 1.1** and mainly consists of a procedural patent.

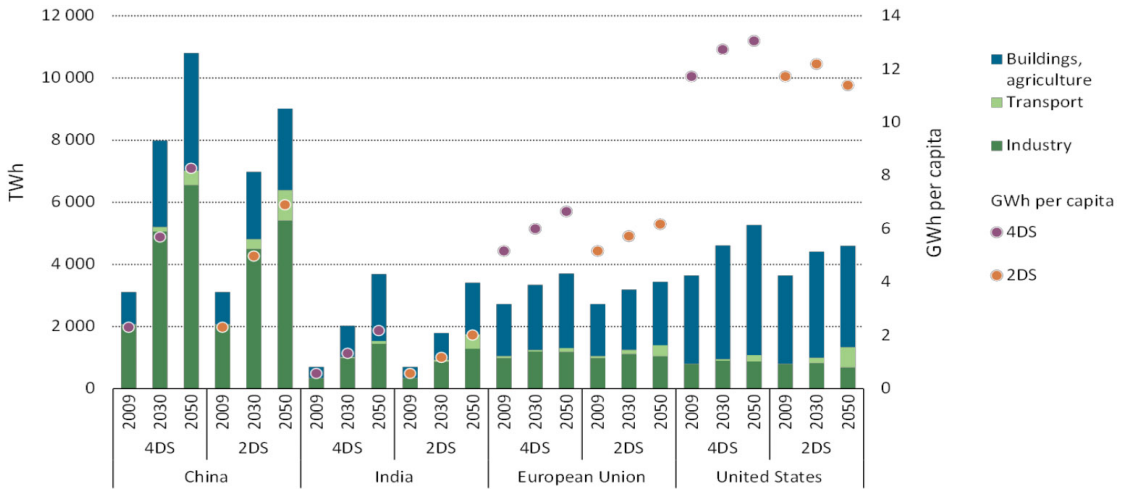

Figure 1.2.: Worlds rising electricity demands by example of China, India, the EU and the USA, IEA [2]

1.1. The Advanced Regenerator - a Concept

The conceptual background and starting point of this work was the patent sketch for a novel technology called the *Advanced Regenerator* (AR). The concept idea itself was invented by Dr. Karl Schwaiger, a dear colleague. Please see his master and doctoral theses [3] and [4] for deeper insights into the topic of fluidized bed heat exchangers, storages and reactors. A conceptual sketch from Dr. Schwaiger - the very cornerstone of this thesis - can be seen in **figure 1.3**.

The AR is meant to function as an ordinary regenerative heat exchanger (also regenerator; like a *Cowper* stove for instance) with the more specific goals of a short to long term heat storage ability yielding minimal losses, high energy density, a countercurrent HEX and an option for power to heat to power (P2H2P) in combination with Stirling engines. This is to be achieved by storing heat in low cost powders (like quartz sand or corundum powder, [5], [6]) and transporting those powders through a *heat exchanger* (HEX) containing a tube bundle (possibly from a Stirling engine, an evaporator etc.) and/or electrical heating rods from a hot storage to a cold one or the other way round. Another application among many could be the heating and cooling of powders in the chemical industries. To make all of this possible in an energy efficient way, a countercurrent regime in the HEX is to be realized. This is implemented by fluidizing the powder with air and transporting it by applying a pressure gradient. The main capacity limiting factor for this technology is expected to be the maximum stable height of the fluidized bed in the storage hoppers (somewhere around four meters) and also the impossibility of fully emptying them, at least in the early stage showed in **figure 1.3**.

Figure 1.3 indeed depicts the essential process layout and the very crux of the matter: The chambers seen in the figure are geometrically and procedurally separated by baffles reaching below the levels of fluidized powder. Those separated chambers enable the build up of a pressure gradient by simply throttling the fluidizing air, entering from below, at it's exits at the top sections of those chambers, permitting a potentially very compact design.

A similar technology has been researched and a prototype for bench tests has been developed

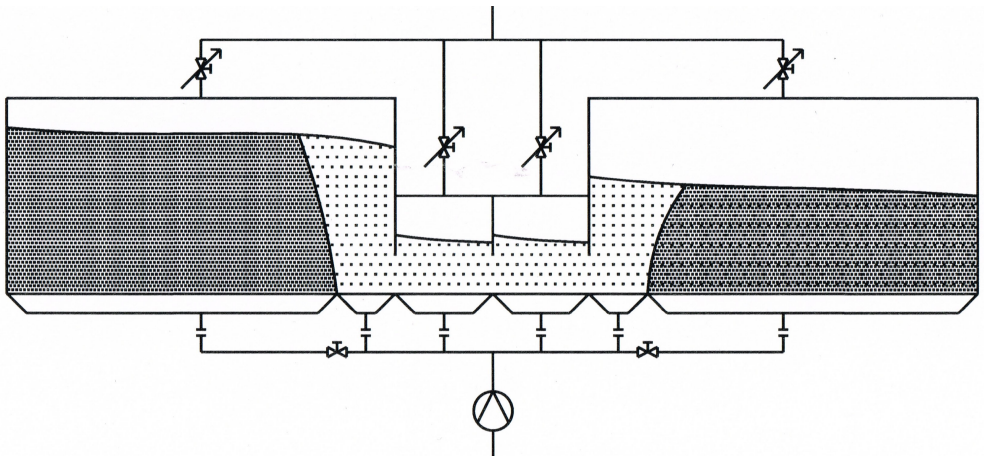

Figure 1.3.: Early conceptual sketch of the Advanced Regenerator from Dr. Karl Schwaiger

during the last years at the *Institute for Energy Systems and Thermodynamics* (IET) at the *Technical University of Vienna* under the project title *SandTES* (see **figure 1.4**, [3], [4], [6], [7] and [8]). The name incorporates quartz sand and the term *Thermal Energy Storage* (TES). *SandTES* is a larger scale TES also including the fluidization of the sand in a HEX to achieve countercurrent flow though it makes use of mechanical transportation devices for the quartz sand (or any suitable powder) at high temperatures. It also features large energy densities and therefore compact storage of large amounts of energy in the form of heat at similarly low heat losses over time rendering it a genuine large scale storage solution for thermal and especially solar power plants. The only grave downside with this technology is its dependence on mechanical conveyor concepts. See **section 1.2** for further information on the importance of fast reacting, small capacity energy storages for today's energy industry.

As a consequence a concept for a Regenerator with good long *and* short term heat storage capability, the ability of fast charging and discharging of that heat and even the possibility of a quick exchange between those modi has been developed at the IET. To make it short the AR could be described as a highly flexible, fast reacting TES with small to medium storage capacity and the bonus of P2H2P. Other powders might even enable larger storage capacities in the near future (see [5] and [6]).

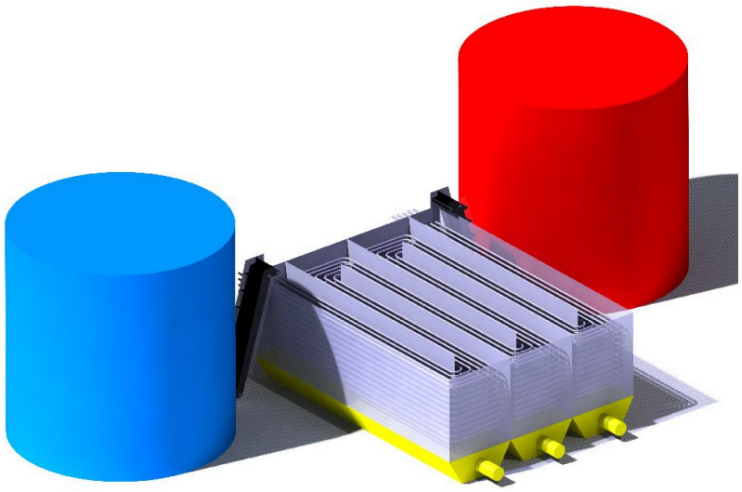

Figure 1.4.: A simple principle sketch of the basic setup of a *SandTES*, [3]

1.2. Motivation

In the year 2000, as an extraordinary example for progressive acting but also for the problem we are facing, Germany brought into force the *Renewable Energy Sources Act*, encouraging innovative technologies by lowering feed-in tariffs for newer plants and basically fixing the feed-in price for renewables, while forcing network operators into preferring renewable feed-in, again penalizing costly conventional plants (especially those with low efficiencies). Basically the country did what had to be done, but that measure still forced enormous changes upon the German and in consequence, as Germany is one of Europe's major industrial players, the Central European energy industry. Germany's renewable energy fraction evolved from below ten percent in the year 2000 to almost 30 percent in 2014, proving the efficacy of the act. However about ten respectively five percent of the German energy mix comes from wind respectively photovoltaics (PV) today and this poses one of the most impressive examples for a basic problem with many renewable energy sources, especially wind and solar power - *temporal unreliability*. This situation actually did not only destabilize Germany's energy industry and grid but also those of all it's neighbouring countries, even forcing Germany to pay them for compensating net frequency fluctuation on windy days, as they were not able to do so on their own - with genuine energy storage technologies (see **figure 1.5**). The German *Renewable Energy Sources Act* of 2000 was later followed by the European Union's *Energy Efficiency Directive* (2012/27/EU) encouraging respectively

forcing further efficiency increases on the European energy intensive industries, inter alia and especially including improved heat recovery, as could be provided by heat storages.

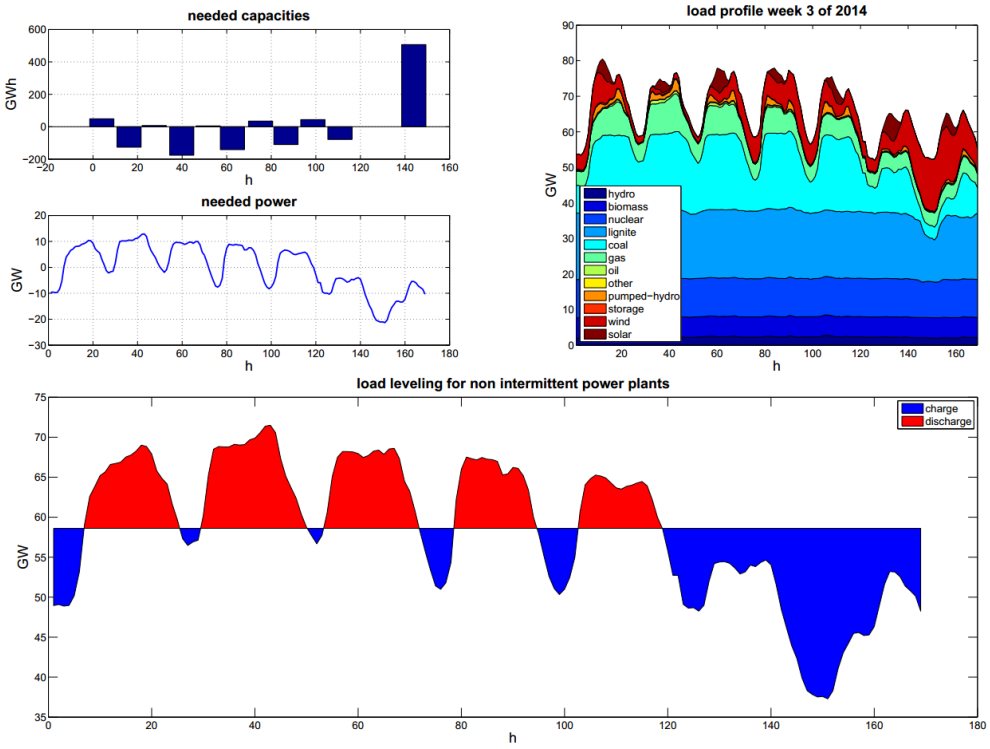

Figure 1.5.: Germany's energy storage potential (week 12, 2014), [4]

Indeed there is up to date no feasible way to store wind or PV energy other than with centralized pumped-storage hydroelectricity or flywheel storages in each and every unit (suitable for wind), because those technologies involve no heat, that could be rather efficiently stored in *thermal energy storages* (TES). Pumped-storages enable very good round trip efficiencies (electrical energy –> stored potential energy –> electrical energy) of well beyond 80 % but are obviously subject to grave topological restrictions and the EU's potentials for hydropower are almost exhausted. Integrated flywheel setups for wind turbines on the other hand might indeed be a decent solution, but individual retrofitting is expensive. Thus was demonstrated the impregnable impossibility of the large scale integration of renewable energies without genuine energy storage capacities by far surmounting today's enabling drastically enhanced flexibility of base load plants and industries. In this context even P2H2P (e.g. with a turn around efficiency of about 30 % in case of the AR) - formerly regarded as sheer wastefulness - has become a realistic and even economically feasible alternative, taking in account vastly fluctuating electricity prices and the simply put "cost-free"

nature of renewables.

In other words, renewables should become more continuously available, reliable and cost efficient, while conventional sources and large consumers (industries) of heat and electricity would need to be more flexible and energy efficient - in turn relieving sources - to overcome the energy revolution. Simple and compact devices like the AR in decentralized setup - being included in every energy- and especially heat-intensive industry, storing heat (or P2H while electricity prices are low) and again returning heat to temporally displaced processes or returning electricity, where heat is not needed - could well achieve that.

2. Method

In this chapter it will be explained what the essential challenges in the layout of the *Advanced Regenerator* are and which methods and tools are needed to overcome those challenges. Obviously a lot of work has been done by the *SandTES* project team and a relevant portion of this know-how found it's way into this thesis. Indeed this masters thesis would not have been possible in the relatively short time period of hardly six months without the hard work of those colleagues.

Section 2.1 will thus point out above mentioned challenges regarding this work and separate them into those to be addressed analytically and those that need to be taken care of in a numerical approach (respectively CPFD simulation). It will be pointed out which software and programs were applied (including a rough introduction in their functionality) and also why those very programs were applied. **Section 2.2** on the other hand will give an overview on which major tasks were performed, utilizing which programs and tools and how they were connected - effectively presenting the overall method to this work.

2.1. Approach

In the process of the procedural, fluidic and constructional layout of the AR several key issues occurred. Some of those were possible to be described with an essentially analytic approach and some required a numerically based approach by utilization of rather powerful CPFD software. Which software was required and which analytic methods were needed will be explained in the next two sections.

2.1.1. Analytic Approach

In this section the problems in context with AR layout, which could be addressed by analytic means will be listed with their matching methods. Furthermore the reader will learn in which cases those methods would not suffice and numerical software was needed. Thus this section primarily concerns the procedural and constructional AR layout, as the fluidic design of the HEX and hopper geometry and the validation of the analytically laid out procedural transport principle for the contained powders as well as the actually needed pressure gradients in dependence of desired particle mass fluxes demanded the simulation of the fluidization regimes in those very units.

The software chosen for the documentation of analytic calculations is *Mathcad*, for its clearly represented formulas and evaluations, perfectly suitable for once the presentation in this thesis but also and especially the dissemination to colleagues for future work regarding the AR. Print-outs of the *Mathcad* calculation files can be found in **appendix A**.

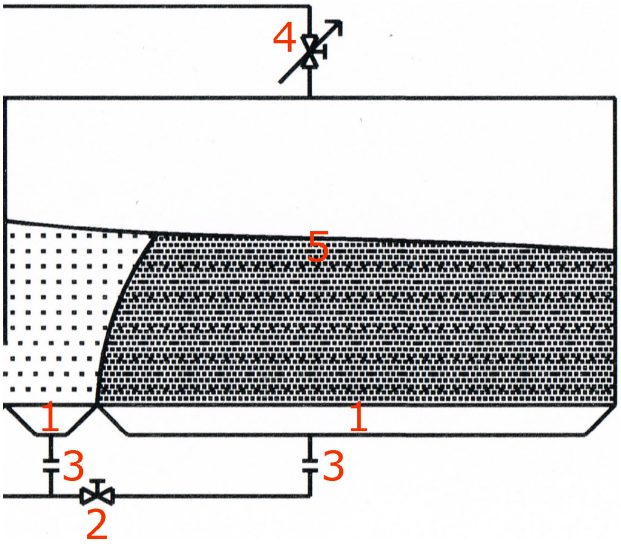

Figure 2.1.: Basic components needed to realize the AR transport principle: **1** windboxes topped with distributor floors; **2** throttle valve for control of the fluidization grade; **3** distributor nozzles; **4** actuated control valve for pressure regulation; **5** fluidized black box

Figure 2.1 shows the basic components needed for the fluidization of an exemplary AR chamber and the control of the pressure in such a chamber with the help of an excerpt of

the above shown patent principle sketch. Those components and their essential calculation will be explained in the following.

The windboxes (early concepts needed two windboxes per hopper base for two different fluidization zones) are primarily empty chambers, providing the necessary space for the entering fluidization air jet(s) to expand and predistribute below the distributor floor. Said distributor floor topping the windbox has the task to homogeneously deliver the fluidization air across the whole floor segment it represents to the fluidized bed. Further details regarding this floor will be given in **chapter 4**. The rule of thumb for the necessary pressure loss of a distributor floor is 20 to 40 % of the vertical pressure difference over the fluidized bed's height. For fluidization with air this means

$$\Delta p = h_{bed}(1 - \psi)(\rho_p - \rho_a)g \tag{2.1}$$

where ρ_p is the particle density, ρ_a the density of the fluidization air and ψ the porosity, representing the fraction of air in the fluidized bed. Fluidization starts at superficial bed velocities just above the so called *minimum fluidization velocity* (u_{mf}). This velocity is dependant on the particles' fluidization air's properties, defined with the velocity which renders concerned particles floating weightless and can be calculated [3, 4, 9]:

$$u_{mf} = \frac{((\rho_p - \rho_a)g)^{0.934} d_p^{1.8}}{1100 \mu_a^{0.87} \rho_a^{0.066}} \tag{2.2}$$

Where ρ_p and ρ_a are again the densities of particles and fluidization air, both in kg/m^3, d_p is the mean particle diameter in μm and μ_a is the dynamic viscosity of the fluidization air in Pas. In this case the so called correlation of *Baeyens* is applied because the powders considered in this work do all show $50\ \mu m \leq d_p \leq 100\ \mu m$ and are localized near the border of Particle groups A and B in the *Geldart* classification of fluidized bed regimes. Further theoretical content regarding the fluidization regime of interest for the AR and *SandTES* concepts - bubbling fluidized beds - can again be found with Karl Schwaiger's work (see [3] and [4]) and also in a very detailed approach with the *Handbook of Fluidization and Fluid-Particle Systems* [9]. This work will incorporate only a minimum of fluidization theory in an attempt not to exceed it's framework.

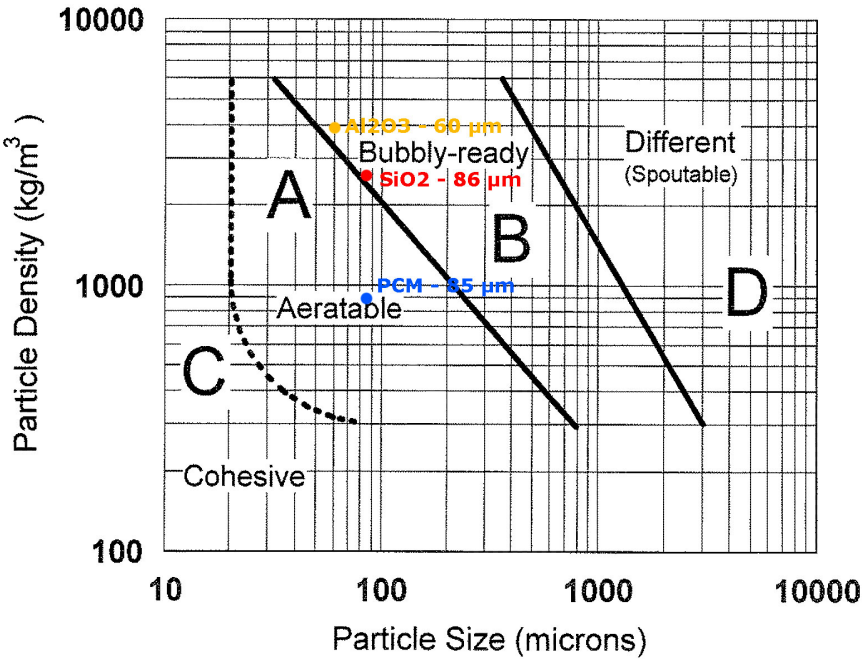

Figure 2.2.: Geldart Diagram with points and mean particle diameters added, matching powders addressed to in this theses, [9]

To achieve a state of fluidization the actual superficial bed velocity obviously has to be a multiple of applied u_{mf}, defining the *fluidization grade* FG:

$$u_t = FGu_{mf} \tag{2.3}$$

There can be found many guidelines for FG depending on the desired fluidization regime (bubbling, turbulent, fast etc.; see [9]), but to effectively identify needed FGs for the different sections of an AR (HEX, hoppers etc.) again CPFD simulations were necessary. Based on that it can be stated that relevant fluidization grades for this technology range roughly between 6 and 16.

The so called distributor nozzles in **figure 2.1** are primitive static nozzles, laid out to present the needed pressure loss for the desired distribution between wind boxes respectively a homogeneous distribution between several inlets located in the same windbox at any FG applied (see **figure 1.3**). In the case of **figure 2.1** the right hand side wind box has it's own throttle valve enabling manual control of FG. These nozzles are also analytically calculated (see [10]). They are only rendered useless, if every windbox has it's own control

valve and a single inlet, as distribution would hence be governed directly and only by the valves. Nevertheless, as long as the windboxes are physically large compared to air inlet diameters, several evenly spread points of air inlet would be advised.

The throttle valves themselves are calculated and laid out from needed FGs respectively resulting fluidization air mass fluxes (and their thermodynamic properties) and possible occurring pressure gradients and absolute pressures, both extracted from the CPFD simulations. Obviously two different functions of valves are applied. Actuated valves at the top of every chamber are meant to control the chambers' pressures by throttling the fluidization air mass flow. This flow is dosed by the valves supplying the wind boxes. An empirical formula found in a manual [11] presented by *Samson* (one of the the chosen valve suppliers of this work besiders *Bürkert*) is utilized to thereby calculate the so called K_{vs} values presented in the data sheets of common valves. It has to be stated here, that in the desired case of a stable AR operation, the fluidization air leaves the device mostly in the same chamber it has entered (see **section 3.3** for possible instabilities).

To achieve some kind of understanding and control of the simulations and especially the co-simulations, an approach for the relation of hopper pressures had to be prepared in terms of coding a controller. *Matlab* was chosen as the platform for coding, as it is highly flexible in linking a versatile programming language with multitudinous functions with genuine plotting options and can itself be operated by a *Python* script for co-simulation. Additionally *Matlab* provides many operations for file management, as output of information from the CPFD simulations would be realized via log-files and Matlab would obviously have to process and rewrite this information for control. Thus a program - moreover referred to as *controller* - was written in *Matlab*, reading and interpreting essential data from simulations, calculating fluidization parameters, printing part of the acquired information for the user and rewriting the simulation's boundary conditions based on that information for co-simulation. See **section 2.2** for further information on software tasks and connections between programs and **chapter 3** for a more detailed description of the *Matlab controller* itself.

A known Problem with bulk materials like sand is the determination of their properties, as this can only be achieved by experimental means like ring shear tests, laser particle

sizers or old fashioned screening - such essential properties as the mean particle diameter (d_p), characteristic angles and porosities (ψ) respectively bulk densities (ρ_{bulk}). Those parameters are needed for the calculation of u_{mf} (d_p), the hopper layout, to achieve genuine emptying behavior (angles) and the system mass, to estimate the actual heat stored (ρ_{bulk}). Conveniently the quartz sand that will be utilized in the first AR bench tests is identical with the particles used for the SandTES prototype and a similar quartz powder (though not the exact same) had already been thoroughly tested. See **figure 2.1** for the particle size distribution of said sand and **appendix ??** for a full report on this study performed by *FH OÖ Forschungs & Entwicklungs GmbH*.

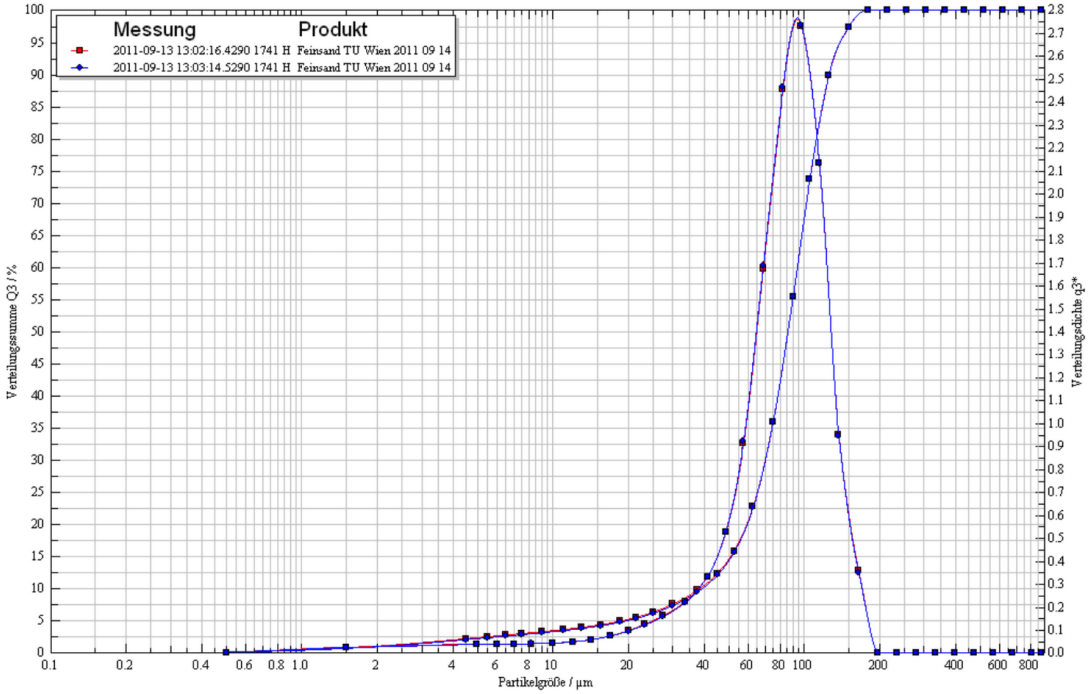

Figure 2.3.: Particle size distribution of the quartz sand used in *SandTES* and *Advanced Regenerator* cold bench tests

Finally the procedural and thermodynamic layout of the AR in whole was also analytically calculated with MathCAD. This concerns the energy density ($\epsilon = \rho_{bulk} c_p$) and possible maximum amount of storable energy in the form of heat (Q), calculated from geometries, bulk densities, storage temperatures and polynomials for isobaric heat capacities (c_p). Also concerned is the manageable heating respectively cooling power (P_{th}) of the HEX, being derived from planned temperature difference (ΔT), again heat capacity and the minimum

and maximum manageable particle mass fluxes (Φ_p) from the simulations. Another important parameter is the maximum time of operation without change of transport direction in dependence of the power P_{th}. Besides the geometry of a tube bundle enabling a heat transfer matching the maximum heating respectively cooling power of the HEX will have to be designed and recalculated for several possible heat transfer meadia at some point and another tube bundle for cold bench tests with a geometry enabling later on scale-up of test results, again requiring values for mass fluxes Φ_p extracted from the simulations.

Said methods and approaches might confuse but they will be summarized in context to each other in **section 2.2** to make understood the overall method applied in the layout process. Although it can be stated right now, that the simulations take the vital role of fulcrum and capstone regarding this work, as they link all of the other parts and can not be cleanly separated from the rest. This will become obvious with **chapter 3** *Simulations*, for it contains a lot more than just simulations.

2.1.2. Numerical Approach

As stated in the last chapter the processes taking place in the fluidized domain *inside* the AR are highly complex and could not be addressed with an analytic or known empirical approach. This is caused by the fact, that hundreds of billions of particles (about 170 billion to be precise) are being lifted, dragged and colliding with walls and each others at the same time. However those very processes are dimensioning necessary fluidization grades FG, pressure gradients Δp and manageable particle mass fluxes Φ_p, as well as the continuous pressure variations above the distributor floors, needed to layout the floors' pressure losses enabling homogeneous air distribution across those surfaces. As stated above, there is a rule of thumb for those values, but as will be shown below (see **section 4.1.1**), that rule of thumb failed in at least one case, due to the atypical character of the AR's *communicating fluidized beds*.

As has been hinted at, the IET at TU Vienna had already amassed noteworthy know-how concerning the simulation of fluidization regimes by the time this thesis was started, concentrated in the person of Dr. Schwaiger and there were two basic methods he proposed.

The first were strict simulations set up with *Matlab*, generating very precise results at very slow rates and thus suitable for applications with comparatively few particles - especially detail simulations. The second one was the utilization of the rather powerful CPFD software *Barracuda* enabling simulations incorporating billions of particles. Dr. Schwaiger had been able to achieve rather impressive validation of Barracudas calculation results in his laboratory fluidized bed trials and later on first bench tests regarding *SandTES* (see [3] and [4]). Obviously *Barracuda* was a genuine choice as simulation software for the layout of the *Advanced Regenerator*.

On first sight CPFD simulations can seem rather similar to CFD simulations, because when fluidized - nomen est omen - particles do act like fluids in many aspects. Nevertheless *particles*, fluidized or not can never mathematically (and thus numerically) be treated as fluids. Apparently particles in a fluidized bed do have deviating size and geometry and they can not be subdivided - only the *fluid* carrying them - but they *displace* fluid and they can never actually *fill* a space and thus will have to share any space (barring a vacuum) with a fluid. Moreover and probably most important particle beds can support shear stresses and will collide with walls and each others. That is just to list some reasons why particles are unlike fluids and why CPFD and CFD do utilize different numerical approaches.

Barracuda for example applies a two phase approach. The calculation of particle and fluid phase in *Barracuda* can be thought of as two separate solvers communicating with each other regarding local boundary conditions (lift, drag, displacement etc.). Furthermore the fluid phase is described with the help of a *Eulerian* coordinate grid, while the discrete particle phase benefits more from a gridless *Lagrangian* formulation. Even so calculation would be impossibly slow for large amounts of particles (billions) if they were not clustered to so called computational particles, which are basically differing amounts of particles with (ideally) similar properties regarding material, density, size and temperature. The amount of particles in a computational particle pimarily depends on local boundary conditions and the overall number of discrete particles in the modeled system.

2.2. Method

This chapter will summarize above-mentioned tasks with their matching software and most importantly explain the way those programs and scripts are meant to work together, as they would each depend on some values being an output of one of the others. At the start stands the analytic approach, as described above. A Mathcad calculation is utilized for the determination of some important baseline boundary conditions, primarily regarding the geometry, including a fair amount of educated guesses and experimental values from *sandTES* but also economic positions. From those early assumptions and calculations first simulations were deduced, validating guesses and experimental values but also step by step enabling the definition of a crude geometry. After achieving a basic geometry (again roughly validated in simulations) the first more detailed simulations were performed.

Those more detailed simulations (containing a larger amount of computational particles) are subject of the actual concept - the method - to this work: They are monitored by the *Matlab* controller by writing any data of interest to log files and then reading those files with *Matlab*. Exchanged data involves: pressures (p) at simulation's pressure checkpoints, particle volume fractions ($V_{frac} = 1 - \psi$) again from checkpoints and effective particle mass flows from fluxes and the flux planes' cross sections ($\dot{m}_p = \Phi_p A_{flux}$). Thus conditions needed for both the simulation and the *Matlab* calculation are obviously to be identical (particle and fluid properties etc.; e.g. for calculation of u_{mf}) and therefore also to be exchanged - manually - at least once per simulation. Additionally some parameters like desired pressure gradients, fluidization grades or modes of calculation and output are always to be set by the user. For detailed information regarding simulations and subsequent insights see the next chapter.

The controller itself has the tasks of continuously reading and interpreting said data from simulations and given by the user. First the controller reads and processes (simple calculations to convert data to needed formats and expressions) the data from said log files (p, V_{frac} and Φ_p) and plots and prints part of the acquired information for the user (p, V_{frac} and $\dot{m}_p$). Then it calculates u_{mf} from particle and fluid parameters to later translate given FGs into air mass fluxes through distributor floors set in *Barracuda*'s so called *flow boundary*

conditions (at the bottom of each AR chamber). A function database, implemented into *Matlab* and enabling the controller to call u_{mf} for several fluids and most importantly particle materials was donated to this work by Dr. Schwaiger. The next step is the calculation and setting of *Barracuda*'s *pressure boundary conditions*, meaning the *controlled* pressures at the top of each chamber. Those are derived from the desired pressure gradients set by the user, corrected with varying hopper pressure differences (due to varying fluidized bed levels in the hoppers). See **figure 2.4** for a most elementary and descriptive AR geometry with boundary conditions, as taken from *Barracuda*. Finally the controller writes the exact simulation time at the start of it's execution to another log file to enable comparison of the current simulation time in Barracuda with the time of the last controller execution for co-simulation.

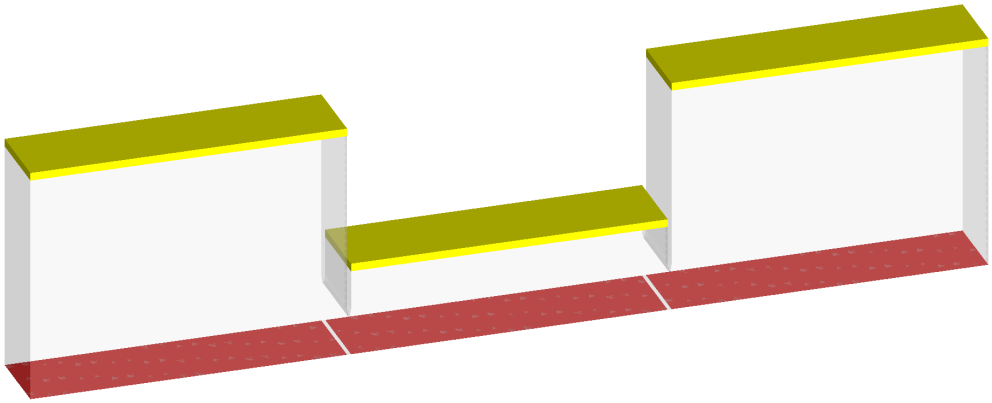

Figure 2.4.: First primitive AR geometry implemented into *Barracuda*: yellow areas represent *pressure boundary conditions* (controlled pessure), red areas represent *flow boundary conditions* (controlled flow)

To actually enable co-simulation, meaning the control of Barracuda by the *Matlab* controller based on above mentioned parameters set by the user, another script has been utilized. It was coded in *Python* and is based on a template for the call of simulation times and reread of *Barracuda*'s boundary conditions received from the *Barracuda* (among many others) distributor and troubleshooter *AixProcess*. Unfortunately the implementation of that template with above mentioned software meant for AR co-simulation incorporated some severe difficulty due to varying software versions. This script however then reads the current simulation time from a *Barracuda* log and compares it to the time of last execution written by the controller. If a certain ΔT (again given by the user) is exceeded it first

starts *Matlab*, executing the controller, again closes it and then initiates a new read-in of boundary conditions by *Barracuda*. To achieve a co-simulation, this process is repeated continuously.

Finally, in the case of successful simulation, data like achieved minimum or maximum mass flow respectively thermal power, modified FGs or startup durations is again (manually) passed back to Mathcad for further calculations like overall performance, layout of tube bundles or response times.

3. Simulations

In this chapter the simulations and later on the co-simulation will be the central topic. Although, as has been explained above, the simulations can not be cleanly separated from the general layout process especially concerning the geometry in context with the fluidic layout. Indeed the first simulations have very primitive geometry and most changes in AR geometry were indeed directly derived from simulation results. Thus this chapter will connect the simulations and their results with the evolution process of AR geometry, thereby enabling a deeper understanding of the AR layout process, described in the next chapter as would be possible by artificially separating those topics. Actually even the transition from this chapter to the next focusing on the actual constructional design of a test bench is expected to be smoother that way, as the reader will gain basic understanding of fluidized bed HEX behavior and the transport of powders following a pressure gradient in this chapter. As it is, lessons learned from drawbacks are in the majority of cases the most intense.

In advance, regarding simulation results and their reliability for real-world application some points are to be set now. Although it will not be stated each and every time those are mentioned and conclusions are derived from them, that the results of simulations are in general to be regarded with some proper caution, the reader is hereby warned of confusing them with real bench tests (which will be definitely necessary and subject of future work). Still *Barracuda* simulation results regarding fluidized bed HEX technology can be seen as trustworthy in a qualitative way and even in a quantitative way to a certain degree, as has been proven by Karl Schwaiger in his experiments (see [3, 4]). Indeed it is hoped, that the authors of future work regarding the AR will mostly be able to validate the simulation results presented in this work.

3.1. First Drafts

This section shortly summarizes the first simulations performed in context of this work, explaining the very reasons that led to the, on first view maybe peculiar AR geometrical design. This *essential geometry* will then be the central content of the next section, **section 3.2**, as it will later on generate some of the most challenging problems in constructional design. It is not goal of this section to calibrate mass flows or perform a quantitative approach of any kind, thus there will be few numbers or units involved here - just comparisons. For more detailed simulation results incorporating actual numerical values see the next two sections, especially **section 3.3**.

The first simple simulation setup was meant to roughly validate the AR transport principle, is again shown in **figure 3.1** and will be referred to as *setup 1* from this point. As all simulations featured in this thesis, these simulations were performed at a constant temperature (850 $°C$ in this case), because actual thermal CPFD simulations are even slower than isothermal simulations. Taking in account the fact that heat transfer coefficients in fluidized beds can be calculated (see [4, 9]) and will hopefully also be well known to the *IET* from hot *SandTES* bench tests soon, this would have been a bad trade-off in such early development stages. Furthermore it should be stated here, that the only baffles installed in *setup 1* are those indispensable *upper* baffles separating differently pressurized AR chambers, as explained above. *Lower* baffles are completely missing at this point.

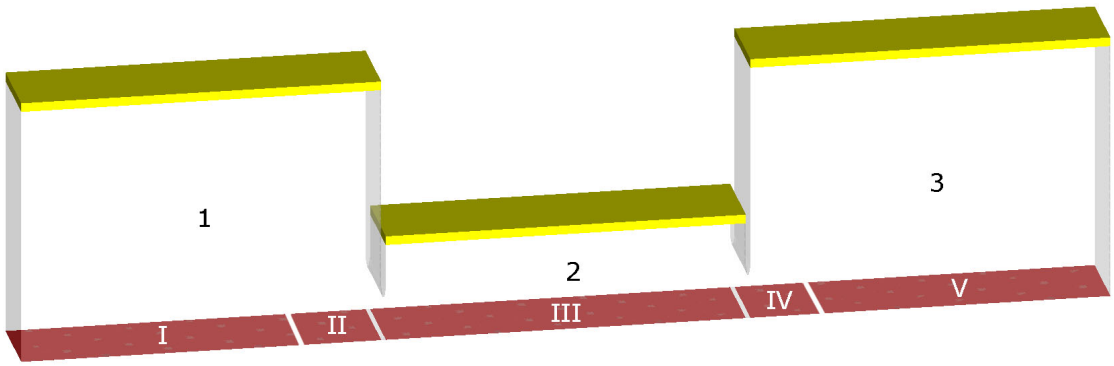

Figure 3.1.: First simple simulation setup

With the exception of material injection and thermal boundary conditions there are only

two kinds of boundary conditions (BCs) that can be defined in *Barracuda*. As a reminder, yellow areas represent pressure boundary conditions and were generally implemented at the top of each AR chamber as chamber pressure control would be realized by a throttling control valve at the top of every chamber. Red areas as depicted in **figure 3.1** on the other hand represent flow boundary conditions, because below the floor of each chamber, air flow would be controlled by throttle valves to then be distributed homogeneously via the chamber's floor. The chambers numbered 1 and 3 represent primitive hoppers or powder storages, while chamber 2 stands for the HEX. Particle flow is meant to be directed from chamber 1 to chamber 3 or from left to right, as will be generally preferred where possible. This shall be achieved by applying a pressure gradient. Thus at the ceiling in chamber 1 pressure is set to 1.06 bar, in chamber 2 it is set to 1.03 bar and in chamber 3 to 1 bar. In this simple approach hydrostatic pressure increase from the particle bed level to it's floor is neglected, though of course it generally can not be ignored and will play an important role later on.

There are five distinct distributor floor sections numbered from I to V in **figure 3.1**. Fluidization grades counting from I to V were set to $FG = 7, 0, 11, 7$ and 3.5, as it was experienced that fluidization zone II needed to take the role of a kind of buffer or brake to prohibit explosive pressure equalization between the chambers 1 and 2. With hindsight this phenomenon occurred due to a too high working pressure gradient in the wake of a neglected hydrostatic pressure increase. Furthermore $FG = 11$ in the HEX is very high and can be one reason for increased vertical mixing, which is an undesired process in a fluidized bed HEX as it potentially reduces exergetic efficiency and renders residence times and effectively temperatures and (introducing a tube bundle) heat transfer in the HEX harder to predict. Nevertheless some degree of vertical mixing is always expected to occur. This will get more clear later on in this section.

Figure 3.2 depicts the particle species distribution over time between 0 and 20 s, altered due to the applied pressure gradient and clearly demonstrates a basic functionality of the AR transport principle. Nevertheless significant vertical mixing (and even back mixing in the upper HEX areas) occurs in any simulation performed based on *setup 1.* A black stroke has been added to **figure 3.2** for a better visibility of this phenomenon, as a perfect HEX

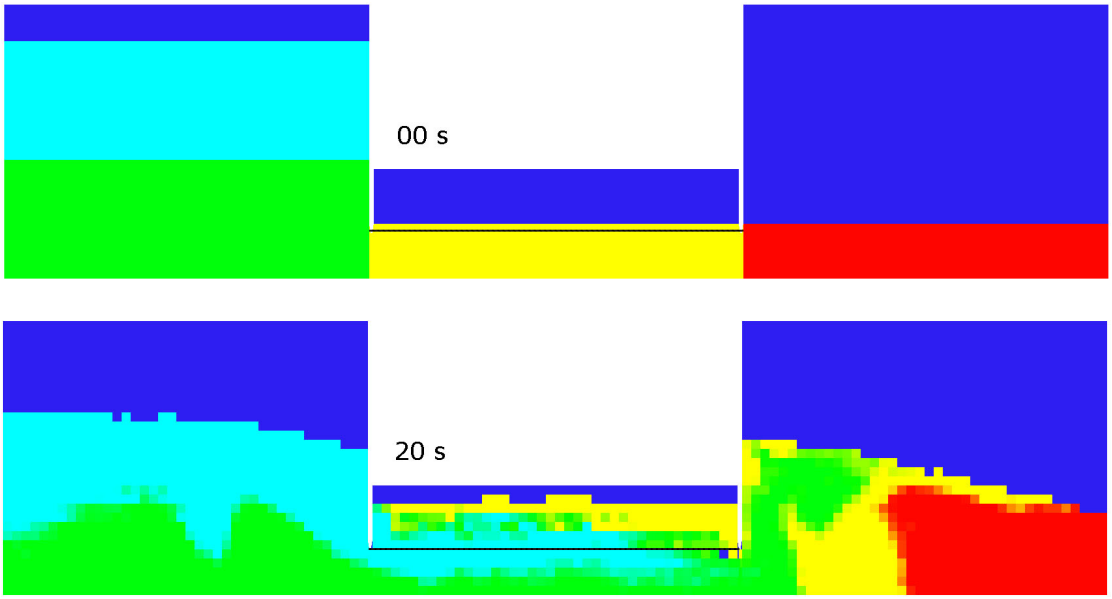

Figure 3.2.: Particle species distribution in *setup 1* at sim-times of 0 and 20 *s*, baffle lower edges are marked with a black stroke for better visibility

regime would be a so called *plug flow*, meaning a constant (flat) velocity profile in each and every cross section with no back mixing, below (and later on between) baffle edges. Thus it is desired to prohibit particles from flowing above the upper baffles' lower edges (respectively above the black stroke) and below lower baffle edges - meaning to force them to flow only in the *channel* between baffles. This also explains why only averaged mass flows will be shown in this section to monitor if any noteworthy particle flow occurs in said undesired regions and finally find a genuine HEX geometry. As stated above the *IET* had some noteworthy know-how concerning fluidized bed HEXs at the time this work started and consequentially it became obvious rather fast, finding such a HEX geometry would involve experimenting with baffles in the next few simulations.

Another more obvious disadvantage with *setup 1* was the impossibility of a satisfactory emptying of hoppers, meaning there would be a large dead volume of powder unable to take part in the process, thus representing mere dead freight. This problem and vertical mixing were decided to be of primary importance at this point. In team work with Dr. Schwaiger an advanced geometry including raised rectangular hoppers with sloped floors enabling genuine emptying was introduced. Thus *setup 2* evolved (including some negligible intermediate steps without symmetry of rotation) featuring more baffles and rotationally

symmetric raised hoppers, as rotational symmetry enables better stability under internal pressure (due to process pressures and powder loads). It is depicted in **figure 3.3**, features the same options regarding pressure control and was simulated with Alumina powder (also corundum, Al_2O_3). Alumina powders ranging at the border between Geldart classes A and B are rather fine (about 60 μm) and fine powders tend to *bridging* and *ratholing* (building bridges over respectively a shaft above the lower hopper exit instead of flowing out) - therefore above mentioned powder properties are essential for hopper layout (see **section 5.3.1**). The sphericity and sharpness of powders do also have an influence on these phenomena because they influence characteristic angles. Consequentially flow BCs (fluidization zones) VI and VII were introduced to help emptying, although they were hoped to be avoided through proper hopper design later on. Ratholing will also play an important role later on (see **section 3.3** and **chapter 4**).

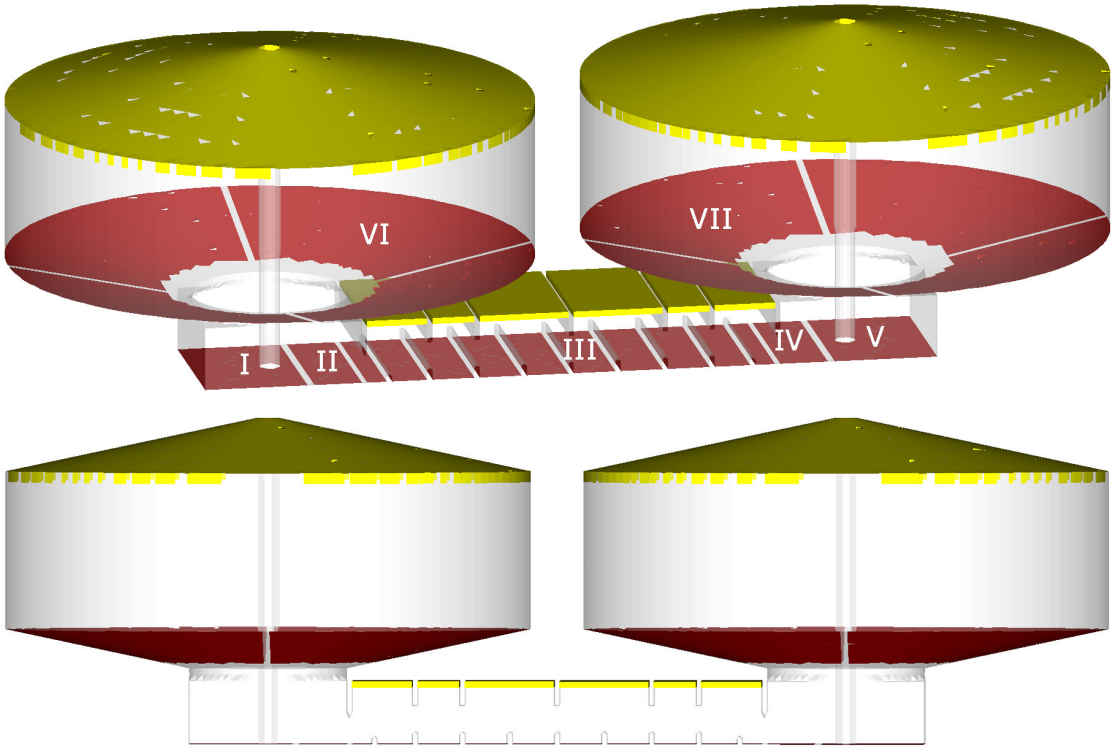

Figure 3.3.: *Setup 2*, featuring advanced emptying ability, rotational symmetry, *lower baffles* in the HEX and more baffles in general

But those problems are to be addressed in detail later, as the transport into and out of the hoppers is a very complex problem in general, that will be a major focus of in-depth simulations. Just now it will suffice to state that utilized corundum (alumina) powders do

mostly tend to ratholing and quartz (SiO2) sand does not. One can therefore ignore the flow into and out of the storages at this point, but the footprints of the risers became soon obvious to need to be reduced, as larger footprint in general means larger air mass flows at the same FG and thus larger power consumption (at least for a fluidized bed with fixed bed height rather than volume, as is the case with the risers). Furthermore the large boxes beneath the hoppers did still need flow BCs II and IV to prevent unstable particle mass flow and it was hoped a smaller footprint would also restrict and thus stabilize those flows. Moreover larger riser footprints also cause larger dead volumes. Anyway, those problems were first to be dealt with in *setup 6* (see **section 3.2**). Another trait of the early *setups 2* to *5* are the poles in the center of the large risers. Those poles seem to benefit transport out of but especially into the hoppers, as the rising particle mass flow circulates and adheres around them forming some kind of more intensly fluidized boundary layer, but this is a phenomenon demanding further investigation to be truly validated and understood.

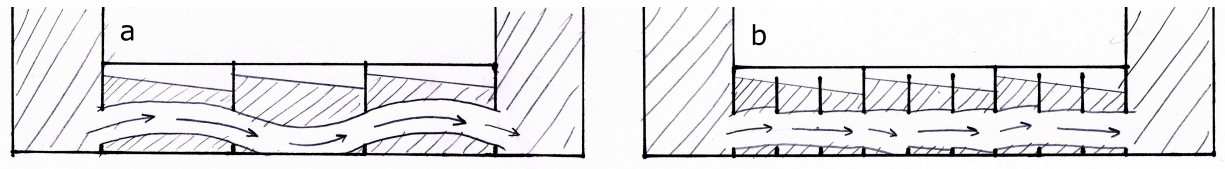

Figure 3.4.: Particle mass flow oscillation in the HEX, schematic illustration as observed in the simulations

Most importantly though several baffle geometries had to be tested at this point to stabilize HEX particle flow and as far as possible restrict mixing to be done with those problems. In this aspect irregular distances between baffles were applied with *setup 2* and did indeed help limit mixing but were also quickly decided to still be too few. Another phenomenon was discovered on the way as the HEX's particle mass flow oscillated in vertical direction while passing through the HEX. This phenomenon is suspected to be induced by hopper-HEX transition and HEX-baffles themselves, seems related to (or actually the reason for) vertical mixing and would thus require and justify further scientific examination for actual understanding. It is depicted in **figure 3.4**, as it was observed in the simulations and can also clearly be seen in **figure 3.8** - further below - where it is mostly under control. *Setup*

2 introduced lowered HEX entry and exit upper baffles, while missing HEX entry and exit lower baffles, as this had also been observed to reduce oscillation. Taking a closer look at **figure 3.4** it should be taken into account, that the oscillation can be broken (or shaped and thus controlled, seemingly in dependency of the particle mass flow's magnitude, **figure 3.4**) by introducing even more baffles - thus representing the simplest approach (as known in this work) of dealing with the problem. Hence *setup 3* introduced more baffles, (**figure 3.5**), while keeping lowered HEX entry and exit upper baffles.

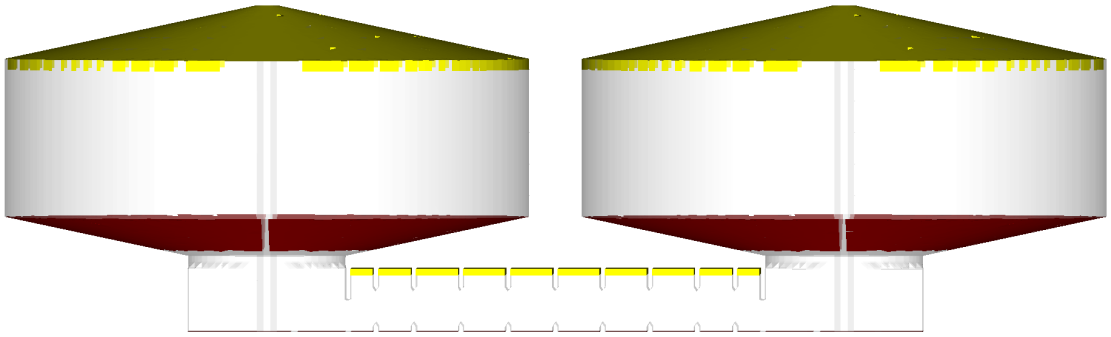

Figure 3.5.: *Setup 3*, introducing more baffles but keeping lowered HEX entry and exit upper baffles, while missing HEX entry and exit lower baffles

Regrettably, the displaced HEX entry and exit baffles also produced lowered HEX in- and outflow, which was undesired, as the tube bundle(s), to be placed in the HEX later on, were obviously meant to be straight (preventing higher cost and pressure loss). Thus a fourth and fifth setup were introduced provided with baffles standing in line. *Setup 4* is not shown in this thesis as it missed lower HEX entry and exit baffles, which were later discovered to not only stabilize and control particle flow oscillation but also to help separating pressures above the distributor floors from chamber to chamber (thus easing hopper fluidization during start-ups). *Setup 5* on the other hand is depicted in **figure 3.6** and additionally features cylindrical risers, which were hoped to further improve emptying behavior by enabling a smoother hopper-HEX transition. Futhermore cylindrical risers would again provide better material stability under internal pressure.

Now, with all baffle edges located at the same height, particle flow oscillation returned, but in a stable, controlled manner. This can be observed in **figure 3.8** together with straighter HEX in and especially outflow. Furthermore vertical mixing was reduced to a reasonable

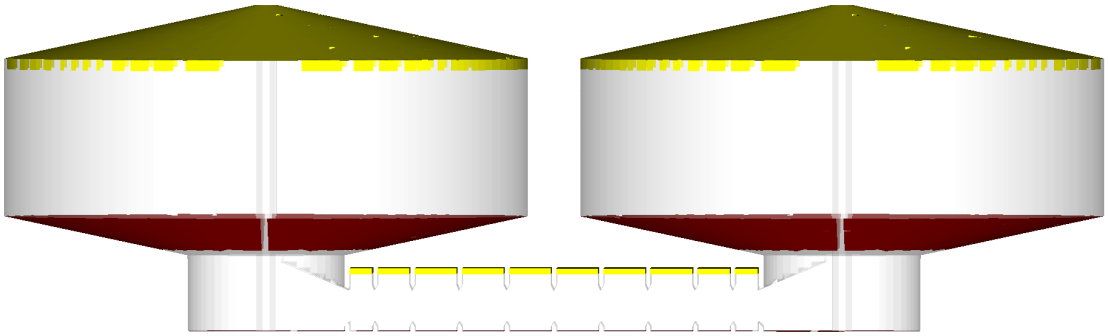

Figure 3.6.: *Setup 5*, discarding lowered HEX entry and exit upper baffles, while additionally introducing lower baffles at the same spots and cylindrical risers

amount, hence concluding overall HEX design. The sharp edges and vast thickness of the baffles were, by the way, not desired but a side effect of *Barracuda*'s grid generator, as it uses the same grid for geometry and fluid calculation, again defining fineness of computational particle BCs. This causes an impossibility of separation concerning the degree of detail in geometry and fluid calculation grid and consequentially forces the user to ever compose the geometrical grid as crude as possible with the desired degree of detail regarding results. This is caused by the above mentioned huge complexity of CPFD, as *Barracuda*'s computation rates are rather slow at the very best of times (10 simulated seconds take between 3 and 20 hours of real time for most simulations performed in this work). Baffle distances were still irregular at this point, although it would subsequently show, that the large number of baffles (as seen with *setup 5*) rendered those irregular distances dispensable. Thus were defined the most important geometrical characteristics of the *Advanced Regenerator's* HEX regarding fluidic design and the most essential concepts regarding the risers.

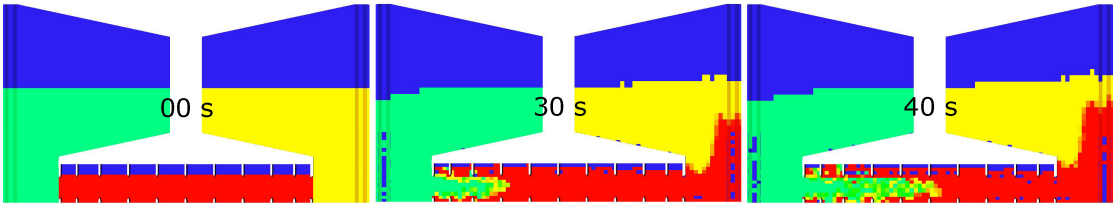

Figure 3.7.: *Setup 5* simulation, particle mass flow with improved HEX mixing behavior, depicted with the help of differently colored species at the times of 0, 30 and 40 s

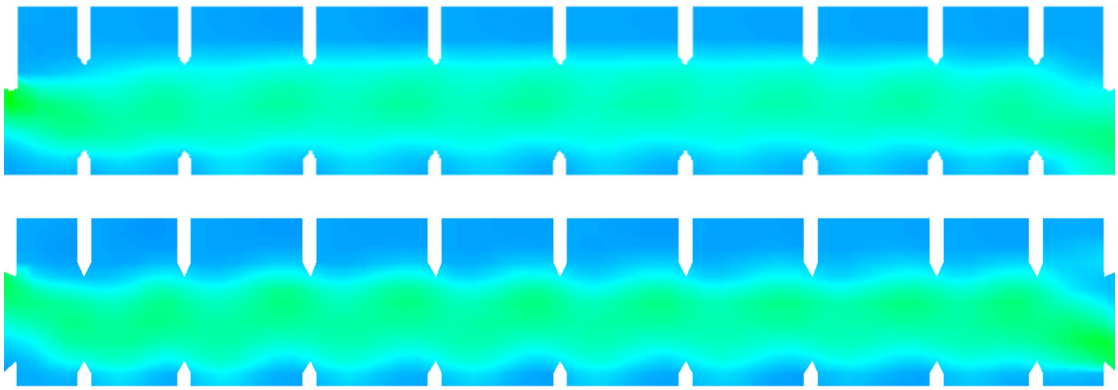

Figure 3.8.: Averaged particle mass flow comparison of the *setups 3* and *5*, averaged over 200 respectively 100 seconds

3.2. Essential Geometry

Setup 5, as seen in **figure 3.6** does already hint at the final shape of the AR concerning this work. It incorporates almost all components and aspects, soon to define the *Advanced Regenerator* and subsequently being referred to as *essential geometry*. It features two elevated hoppers shaped as rotationally symmetric silos above cylindrical risers, connecting the hoppers to a HEX. The HEX is basically an elongated box with many periodically aligned lower and upper baffles, potentially rendering it a still simple, yet highly flexible setup with the ability of rapid changes of direction of transport. It enables a plug flow with little back or vertical mixing between those storages. This is not to say it is *the one* geometry obligatory in terms of overcoming all challenges regarding the AR obviously, but it is very much *the* geometry that is hoped to do so in this thesis. As it was *one* setup *had* to be chosen for further enhancement in the simulations to come. Moreover it has to be kept in mind, that the only seemingly stationary mass flow to this point had been achieved with this setup (utilizing corundum powder with $d_{pm} = 60\ \mu m$). Consequentially in this section such *essential geometry* will be accomplished by what can be seen as a progression of several distinct improvement steps from *setup 5* and additionally those very steps are to be explained in detail on the next pages.

Concerning baffles *setup 5* provides genuine spacing with rather low but sufficient lower baffles. As a reminder, irregular spacing has been shown to decrease particle flow oscillation

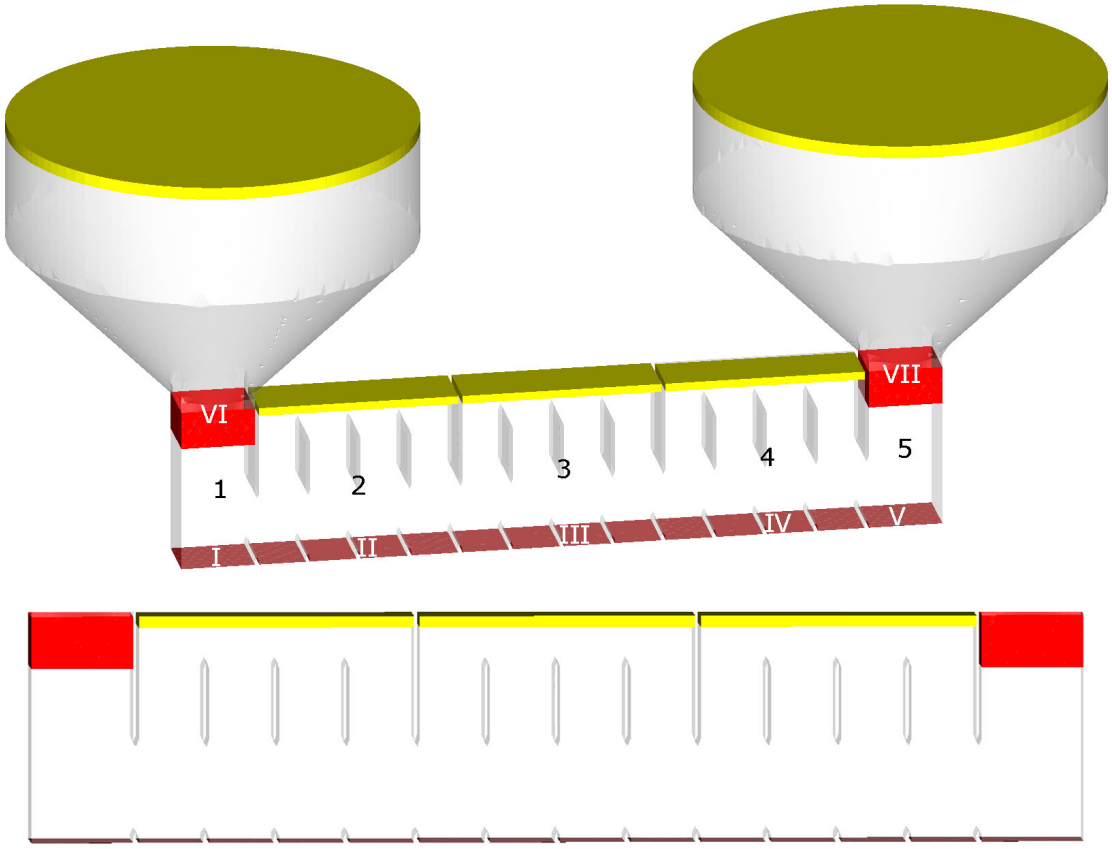

Figure 3.9.: *Setup 6*, introducing quadratic riser footprints (I and V), three-chamber HEX (chambers 2 to 4, fluidized via floors II to IV) and circular fluidization in the risers (VI and VII)

(mixing) though being redundant to the effect of a higher number of baffles. The upper baffles on the other hand are too low in a procedural sense, as the HEX tends to fill up almost to the top or even overflows (clogging and blocking air outlet filters and valves), due to the absence of an adequate buffer, able to compensate particle mass flow fluctuations. The HEX has basically been one large chamber with artificial and essentially pointless separating baffles, that would lead to an unreasonable count of outlet valves. Consequentially *setup 6* provides only three distinct HEX chambers (chambers 2 to 4) to be separately fluidized and able to hold varying pressures enabling the application of a pressure gradient along the HEX. As the baffles inside those chambers are not reaching all the way up to the top, leaving space for the air to flow free thus balancing pressure along the chamber, one valve per such segment suffices.

Nevertheless the most important and momentous procedural and fluidic change with the

introduction of *setup 6* are two new, circular fluidized surfaces enclosing both risers just below the hoppers referred to as *nozzle rings* or later on *sinter rings*. Those *rings* initially were the solution to a specific problem occurring while starting up. As has been explained above fast reaction times are an important part of the AR's concept. Riser (respectively hopper) fluidization time represents a manifest bottle neck in terms of flexibility. In the first attempts to achieve startup as fast as possible all chambers were fluidized at the same time with no sinter rings for additional fluidization. In retrospection consequences are obvious: the HEX's bed, being much more shallow, was fluidized long before the risers (especially the riser below the fuller hopper) and the air mass flows meant to fluidize the risers were sidetracked taking the way of least resistance - through the HEX (**figure 3.10 (a)**).

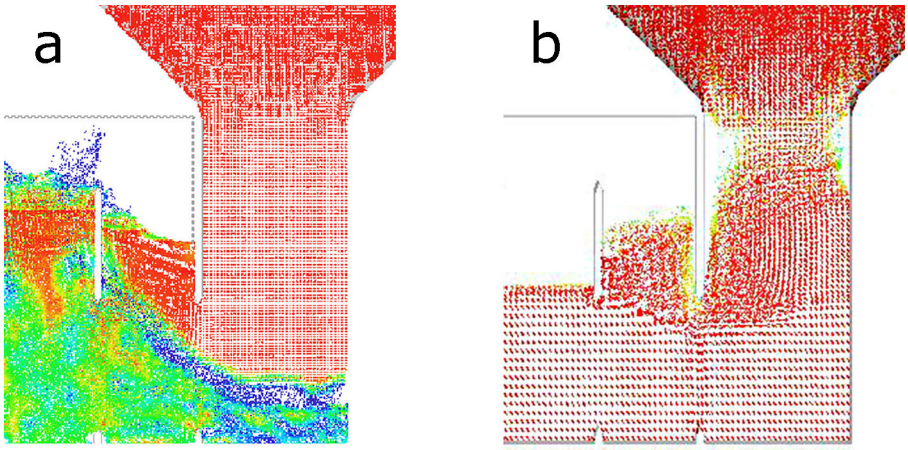

Figure 3.10.: Fluidization of risers, two extremes: HEX fluidized without nozzle rings **(a)**; HEX not fluidized with nozzle rings **(b)**

This problem had to be addressed or it would render fluidization of especially full hoppers difficult and slow at significant cost of overall flexibility. Thus a first approach was to perform fluidization of risers before fluidizing the HEX and indeed full hoppers could be fluidized that way, especially when higher HEX than riser pressures were applied (closing HEX outlet valves and applying a low $\dot{m}_a$). Nevertheless fluidization of full hoppers' risers was still slow because $\dot{m}_a$ was restricted by the pressure above the distributor floor, being restricted by the maximum system pressure defined by applied compressor power and the desire to stay below 1.5 *bar* absolute in an attempt to avoid application of the pressure equipment directive at least for a cold test bench (and also to limit material stresses). Thus a second step to overcome such challenge was the introduction of said *nozzle rings*, as their

application enabled the admission of maximum pressure and the larger part of $\dot{m}_a$ fed to the riser above the level of the HEX, thus using the sand filled lower riser as a buffer and brake (**figure 3.10 (b)**). **Figure 3.10** demonstrates the problem depicting both extremes.

With *setup 6* utilizing corundum powder the erection of stable fluidized *pillars* within hoppers, able to perform transport into but also out of those storages, without being forced to shut down fluidization in the to-be-emptied hopper's riser and thus suffering long reaction times when switching direction of transport, was achieved for the first time. The stability of and the transport within those *pillars* will be central recurring issues in **section 3.3** and throughout this work as they form probably *the* biggest challenges concerning this thesis. Although it has to be stated here with every emphasis that those stability problems did only occur with larger bed heights ($h_{bed} \geq 0.91\ m$). However those larger bed heights are (even if never achieved) to be tested in cold bench tests, as the maximum bed height enabling stable transport is a major limiting factor regarding the AR's application. The fluidization via sinter rings seems to additionally stabilize pillars, enshrouding them with a shaping air mantle, only slowly to be mixed with the fluidized powder forming the pillar itself while progressing further up into the hopper and moreover reducing viscous friction between pillar and actual hopper fill. **Thus broadly speaking the *major challenge* regarding the AR layout in this work is the difficulty of *transportation into and out of powder storages located above the level of the HEX*, necessary to enable total emptying of those storages.** This topic would be a genuine starting point for further examination and research indeed, as it would go beyond the scope of this work.

Additionally *setup 6* reduced the riser footprints as demanded above and further explained below and presents a square base, as it enables better symmetry of hopper-HEX transition and thus more desirable emptying behavior than an elongated rectangular footprint. Furthermore as the square prism presents maximized area-to-girth ratio (A/G) it was expected to offer a maximized fluidized pillow stabilizing effect per unit of $\dot{m}_a$. The HEX's transport cross section itself was chosen to be identical to the riser's footprint with the dimensions of 150 mm x 150 mm to enable at least three vertical rows of staggered tubes later on. Moreover *setup 6* was the first setup to be controlled by the Matlab controller script mentioned above (**section 2.2**) although it was still a long way to go before actual co-simulation. To

keep this section manageable for the reader the controller will be introduced in detail with **section 3.3**.

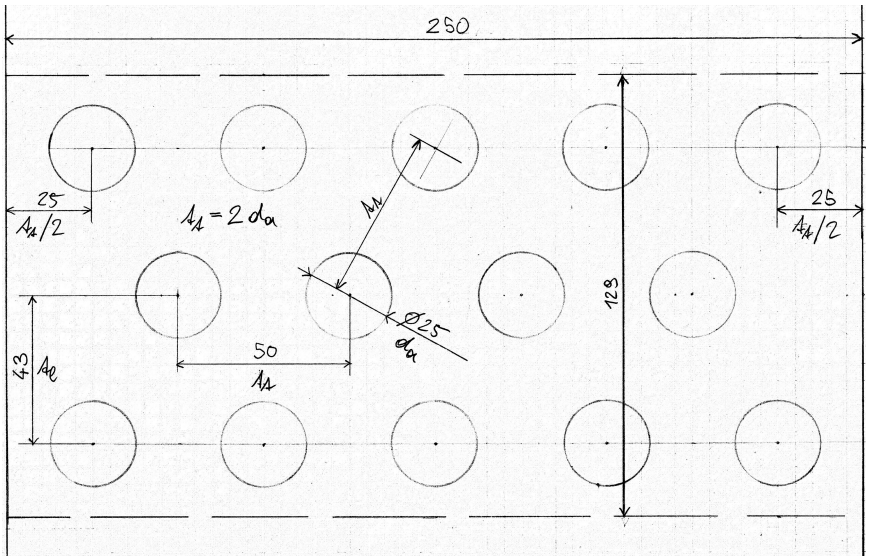

Figure 3.11.: Cross section of a staggered tube bundle dimensioned for genuine scaleability of results with a fluidized bed HEX; dashed lines represent the HEX's lower respectively upper baffles' edges

$$P_s = \dot{m}_a \frac{\kappa}{\kappa - 1} \frac{p_1}{\rho_1} \left(\left(\frac{p_2}{p_1} \right)^{\frac{\kappa-1}{\kappa}} - 1 \right) \tag{3.1}$$

Equation 3.2 shows the isentropic (and adiabatic) power consumption of a compression or expansion of an ideal gas, where the indices 1 and 2 represent states before and after such process. κ is the isentropic exponent of dry air. The relation is utilized to gauge and compare power demand of air compression in this work. Obviously for the risers' fluidized beds with given heights (depending on hopper levels) and temperatures (depending on mode) and consequentially given air pressure and density above the distributor floor, the only way of reducing such power consumption is the reduction of air mass flow $\dot{m}_a$. Moreover, maintaining desired fluidization grades ($FG = u_t/u_{mf}$) the only way to reduce $\dot{m}_a$ is to reduce the riser footprints as was done with the introduction of *setup 6*. In the heat exchanger on the other hand, not bed height, but its horizontal cross section is given, as certain desired particle mass flows $\dot{m}_p$ have to be achieved via possible mass fluxes Φ_p and a resulting cross section in flow direction. This means HEX compressor power can only

be reduced through optimization of the beds' height-to-breadth ratio h_{bed}/b_{bed} as the HEX's length is given by the needed tube bundle's surface and consequentially length. Leaving out further details such optimization (in dependence of the beds pressure loss per unit of height and thus density and fluidized porosity) leads to a shallow and broad bed in the present case. Furthermore as staggered tube bundles should consist of at least three vertical layers of a minimum tube diameter ($d_a \approx 25\ mm$) and spacing (roughly $t_t \geq 2d_a$) to later on enable genuine scaling of results (see **figure 3.11**), a minimum bed height is deduced. The bed's breadth can hence be written as

$$b_{bed} = A_\Phi / h_{bed,min} \tag{3.2}$$

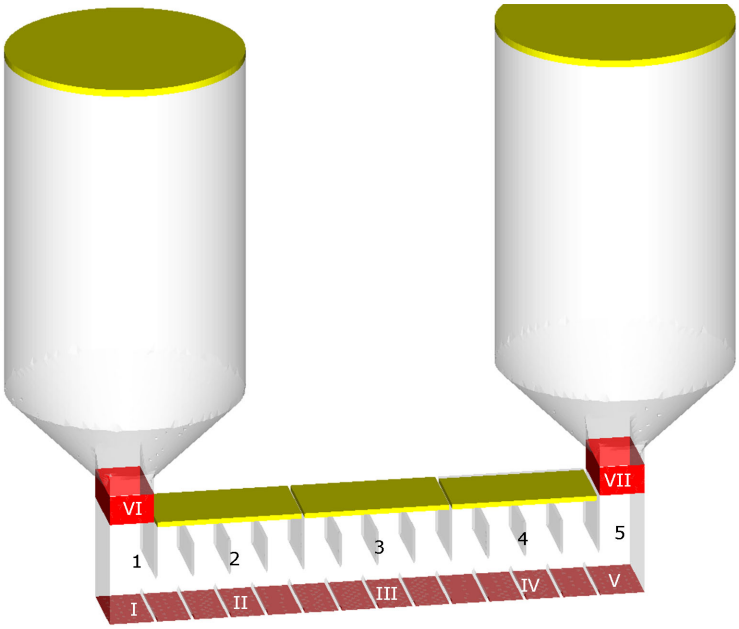

Figure 3.12.: *Setup 7*, introducing shallow broad HEX bed (leading to rectangular riser footprints) and higher hoppers

where A_Φ is the cross section in transport direction, necessary to achieve desired range of $\dot{m}_p$ with the possible range of Φ_p extracted from simulations. For the AR HEX this procedure resulted in a height-to-breadth ratio $h_{bed}/b_{bed} \approx 0.5$ with a transport cross section of roughly 130 mm x 250 mm. This HEX cross section was first introduced into the simulations with *setup 7* including resulting non-quadratic rectangular riser footsteps, as their bases should be minimized, as mentioned above. This considerably elongated rectangular footstep how-

ever again led to an asymmetric hopper-HEX transition respectively unfavorable emptying behavior (especially in combination with corundum powder) and most importantly to unstable fluidized pillar geometry as this structure is charged with a surface load (surrounding powder hopper fill). Thus, as explained above, the footprint to girth ratios of the risers had to be optimized again and as a square base would have led to unnecessarily large riser footprints, cylindrical risers were re-introduced with *setup 8*. Thus completing the *essential setup* of the AR barring installations inside the hoppers addressing emptying and charging issues (see **section 3.3**).

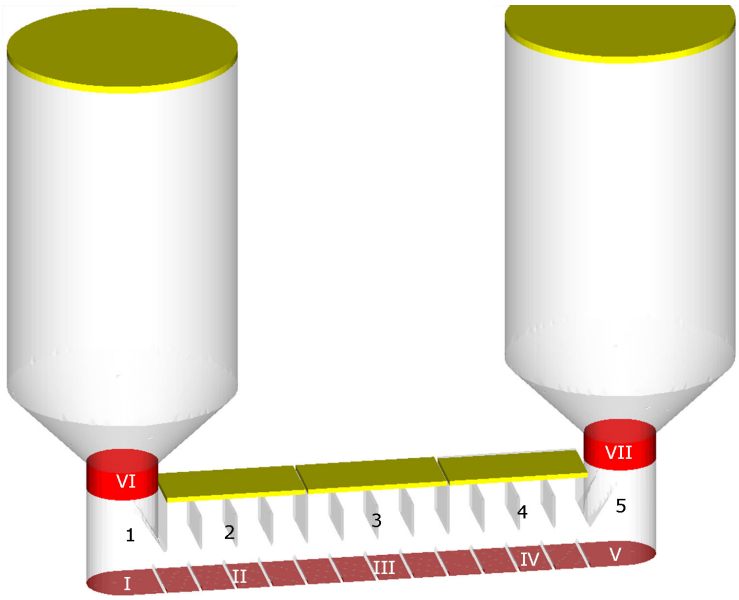

Figure 3.13.: *Setup 8* referred to as *essential geometry*, reintroducing cylindrical risers

As stated above *setup 8* referred to here as *essential geometry* is not *the one* geometry needed to solve all problems regarding the AR, but *the* geometry that is hoped to do so in this thesis, as a setup had to be chosen for further simulations. To indicate manifold possibilities of varying hopper design an exemplary setup (deemed to be worthwhile some further examination) is introduced with **figure 3.14**. It should be obvious from the equivalent numbering of chambers (1 to 5) and fluidization areas (I to VII) the proposed alternative setup follows the same basic principles as the *setups 6* to *8* introduced above. However it could be hoped that this setup would provide better fluidized *pillar* stability due to those pillars being supported by walls from 3 sides. Nevertheless further simulations would be needed to validate whatever hopes regarding this setup. Especially taking in

account very slow calculation times (10 simulated seconds taking between approximately 5 and 10 hours of real time for this setup with a minimum amount of computational particles) at this level of detail concerning geometry and number of modeled particles simulated, such further simulations were not to be achieved in the time frame of this theses, as simulations were running day and night from the time co-simulation was first achieved (with *setup 8*, see **section 3.3**).

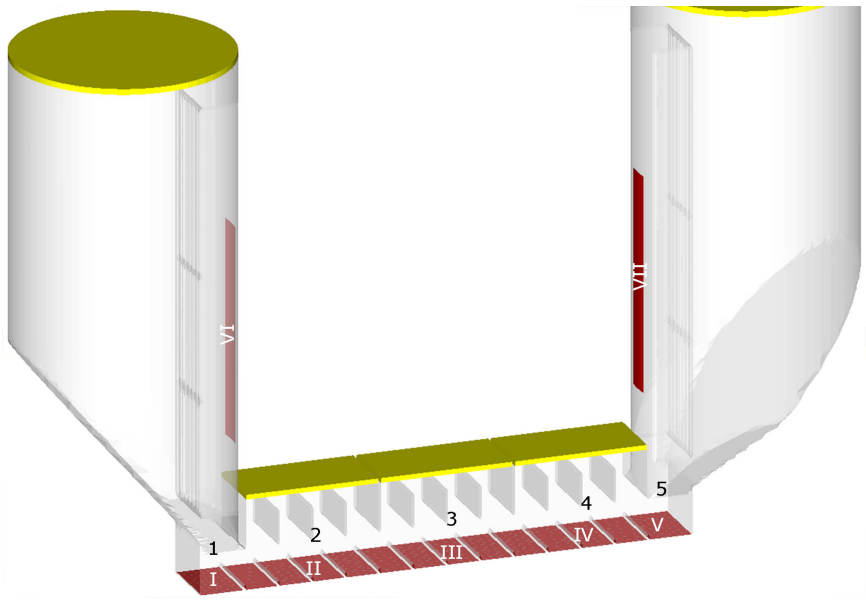

Figure 3.14.: Exemplary setup with non rotationally symmetric hoppers, indicating varying approaches to AR geometry could be successful

To this point only setups with BCs and node fields interpolated from cell values (eularian data) have been shown. Though matching the duality in the solver *Barracuda*'s post processor is also able to process particle fields (lagrangian data), enabling two rather different views on any simulation performed. This is stated to explain the obvious differences in appearance of figures presenting particle data here in comparison to those above, showing only cell data or node data interpolated from cell values and hence will also be denoted in the next few figures' underlines, to call the readers attention on that aspect. In the following some exemplary screenshots from *Barracuda*'s post processor are shown, featuring some essential fields regarding the transport of corundum powders (from the left hopper to the right) in a simulation performed with *setup 8* geometry and BCs as shown in **figure 3.13**.

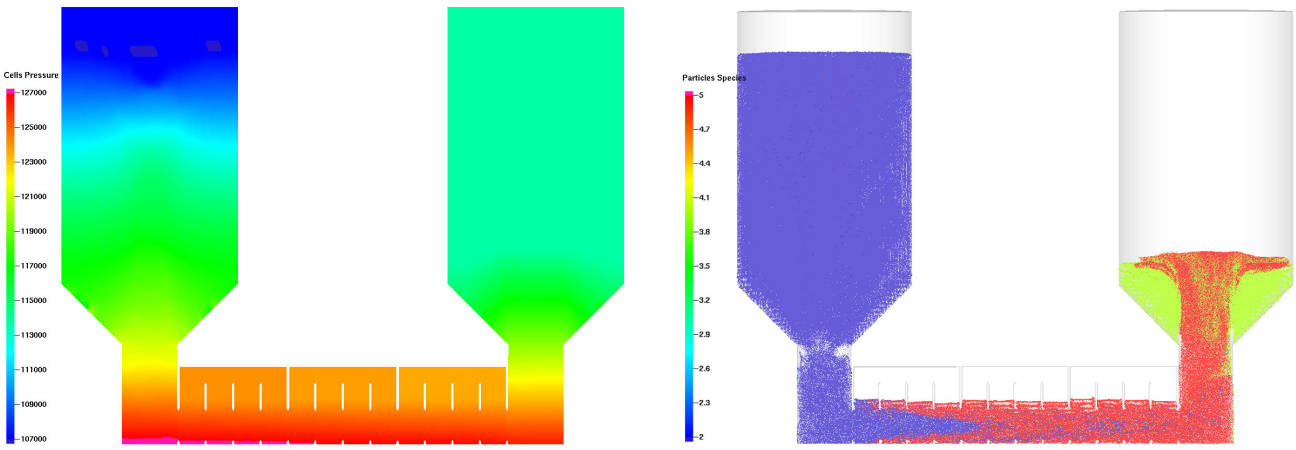

Figure 3.15.: *Setup 8* simulation, corundum powder fill, transport from left to right hopper - pressure (left hand side, node data) and particle species (right hand side, particle data) - check legend to find numeric values for pressure in Pa

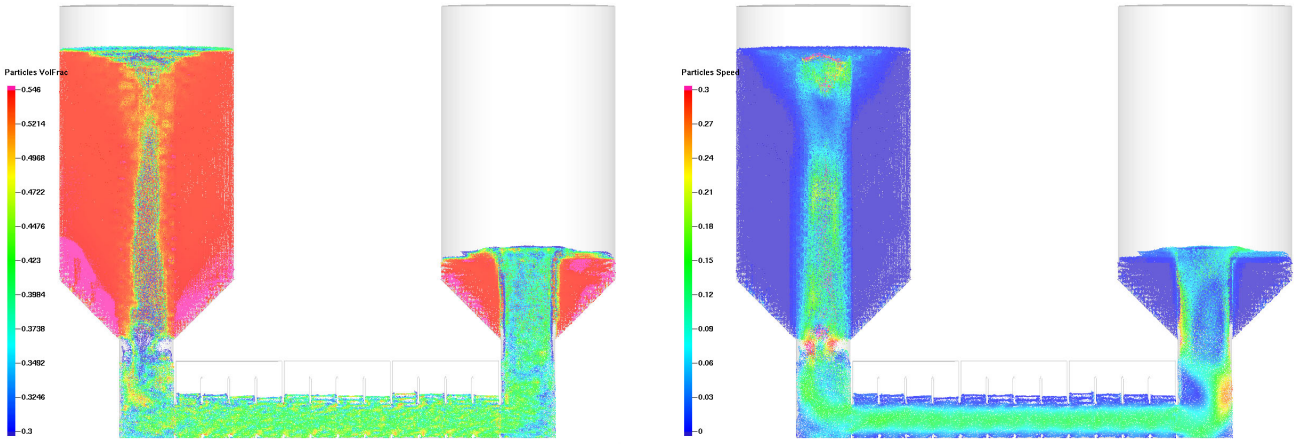

Figure 3.16.: *Setup 8* simulation, corundum powder fill, transport from left to right hopper - volume fraction (left hand side, particle data) and absolute particle velocity (right hand side, particle data) - check legend to find numeric values for volume fraction (dimensionless) and absolute velocity (m/s)

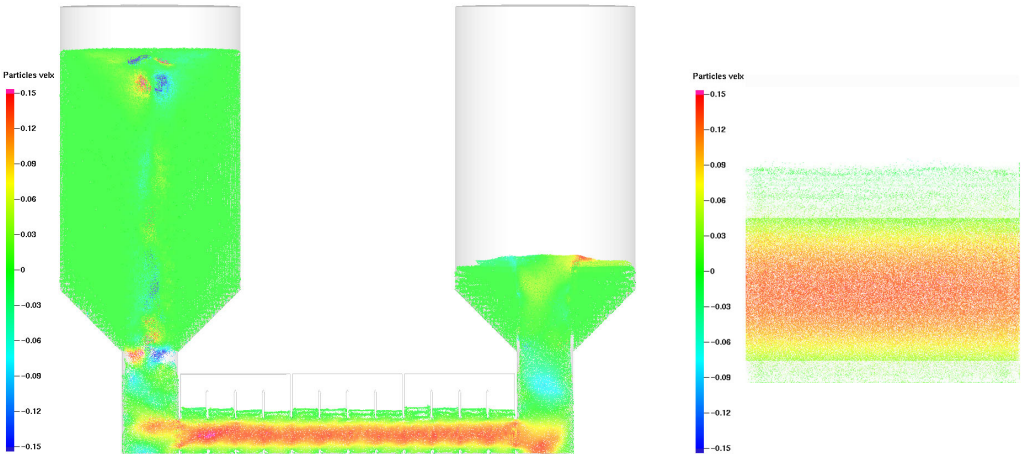

Figure 3.17.: *Setup 8* simulation, corundum powder fill, transport from left to right hopper - particle velocity in positive x direction or from left to right (left hand side, particle data) and particle velocity distribution in a HEX cross section (right hand side, particle data) - check legend to find numeric values for velocities in m/s

3.3. In-Depth Simulations

After achieving an *essential geometry* in the last section, this section will finally introduce exemplary in-depth controlled simulations with that very *setup 8* and small variations from it, but also *setup 7*. In addition to further observations regarding a variety of stability problems, actual numerical values regarding applied pressure gradients Δp, fluidization grades FG and hence achieved particle mass fluxes Φ_p will be presented, as they will form the basis for the final test bench layout addressed to in the next chapter. As a reminder, quantitative simulation results are to be considered with some proper caution regarding their accuracy. This is one major reason for a two step test bench layout (first cold then hot), because the process factors gauged from the cold test bench (hopefully mostly validating CPFD results) will be utilized for the hot bench's final layout, as it will be much more expensive.

3.3.1. Co-Simulation

To output data from barracuda many *transient data points* (virtual checkpoints) for volume fraction respectively pressure logging and several flux planes had to be defined within *Barracuda*. The data points would then directly output V_{frac} and pressure data and the flux planes would output flux data to be multiplied with the matching cross sections later on. As explained above, this data is then written to log files, read by the *Matlab controller* script, processed for rewriting *Barracuda*'s BCs to achieve actual control of the simulation and finally plotted for the user. The **figures 3.18** and **3.19** depict those flux planes respectively checkpoints. Again conveniently secified directions *left* respectively *right* do always indicate *negative* respectively *positive* x-axis direction.

Each riser (and hopper) holds 456 V_{frac} data points in a plane, to somewhat limit computation time while enabling high resolution regarding V_{frac}, as pressure fluctuations in the risers due to V_{frac} variation range in roughly the same scale as applied gradients for transport and thus are to be decided critical for control. It has been tried to achieve control that way and it would have been preferred compared to the strict pressure control applied in

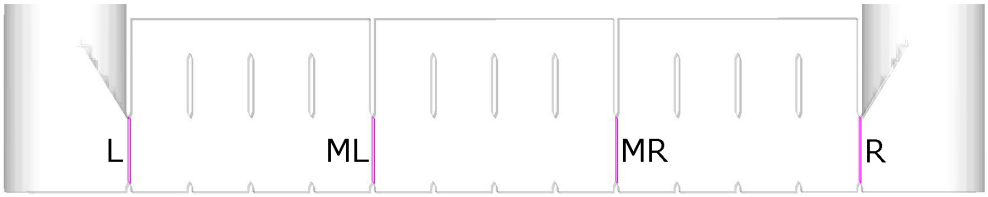

Figure 3.18.: Flux planes for logging of absolute particle mass fluxes, as set in *Barracuda* - 4 flux planes located at in- respectively outlets of HEX segments with 500 mm length each (black characters represent identifiers to be used in controller plots below)

the end, because it could have delivered at least an understanding and at best an empirical correlation for the link between fluidization / V_{frac} and resulting pressure variation in the risers respectively pressure loss occurring with particle mass in- and outflow. Unfortunately, as has been mentioned, with bed heights greater than approximately 1 m fluidized *pillars* within risers / hoppers become unstable inter alia due to occurrence of many (large) bubbles, being subject to uplift and produced by air acceleration due to pressure respectively air density reduction while progressing in positive z-direction through a fluidized bed. To achieve said control respectively correlation those bubbles would have to have been treated separately to the homogeneously fluidized areas being subject to downthrust. On the other hand a high resolution in V_{frac} (though maybe not necessarily as high as deemed needed for control) would enable plots precise enough to render continuous monitoring of post processor data (and consequential cost in real and simulation time) potentially obsolete.

Pressure check points on the other hand do count 25 all-in-all, as only actual transport channel pressures were of interest for control. Those checkpoints are reaching up into the risers to an approximate height just below the sinter rings' air injection zones, as minimum respectively maximum occurring pressures were often located in the risers. Those pressures were corrected according to their height difference to the channel and matching V_{frac} values ($\Delta p = V_{frac\Delta h}\Delta h(\rho_p - \rho_a)g$) and are calibrated with a constant ranging around 0.9 due to viscous wall friction. Furthermore the relation between hopper (and HEX) pressures, needed to consistently write pressure gradients set by the user (for an exemplary left to right hand side transport) to *Barracuda*'s pressure BCs (yellow areas in setup figures) was

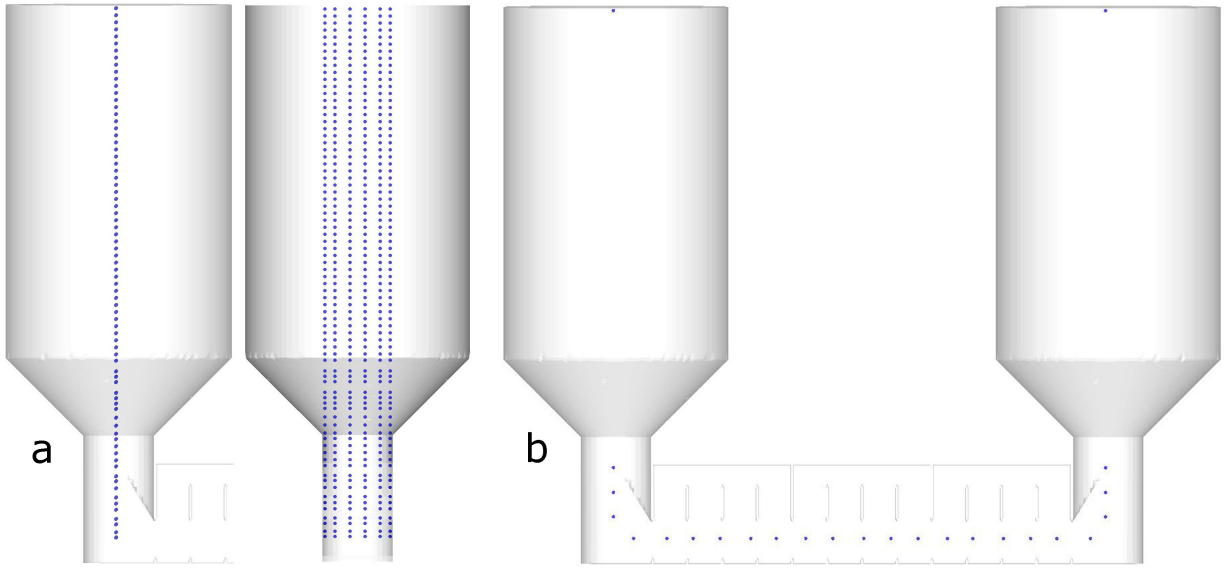

Figure 3.19.: 456 data points per hopper for logging of V_{frac} **(a)** and 25 data points overall for pressure **(b)**, as set up in *Barracuda*

set up as

$$p_{hopR} = p_{hopL} + \Delta p_{hopL} - \Delta p_{edgeL} - 2\Delta p_{HEX} - \Delta p_{edgeR} - \Delta p_{hopR} \tag{3.3}$$

where p_{hopL} and p_{hopR} represent the pressures at the tops of the storage hoppers measured by the uppermost pressure checkpoints depicted in **figure 3.19**. Thus p_{hopL} or p_{hopR} respectively is always to be set to the minimal pressure allowed to occur (p_{min}), which is the ambient pressure plus an air pressure drop in filters and tubes before final air outlet, in terms of calculating the other. This is set by an if-else term, hence prohibiting occurrence of a pressure below p_{min}. Δp_{hopL} and Δp_{hopR} on the other hand are the pressure drops in said hoppers' fluidized beds obtained from evaluation of matching pressure checkpoints. For a pure V_{frac}-control, as has been stated above, Δp_{hopL} and Δp_{hopR} would be calculated from mean V_{frac} along the hopper height (e.g. $\Delta p_{hopL} = V_{frac\Delta hL}\Delta h_L(\rho_p - \rho_a)g$). Δp_{edgeL}, Δp_{HEX} and Δp_{edgeR} are the desired gradients set by the user from left hopper to HEX, from one HEX segment to the next and again from HEX to the right hopper in this order. **Equation 3.3** presents the same pressure gradient Δp_{HEX} twice (for three HEX segments as shown with the latest setups), though two different values could also have been applied.

Figure 3.20 finally depicts one exemplary *Matlab controller* plot and lists all included

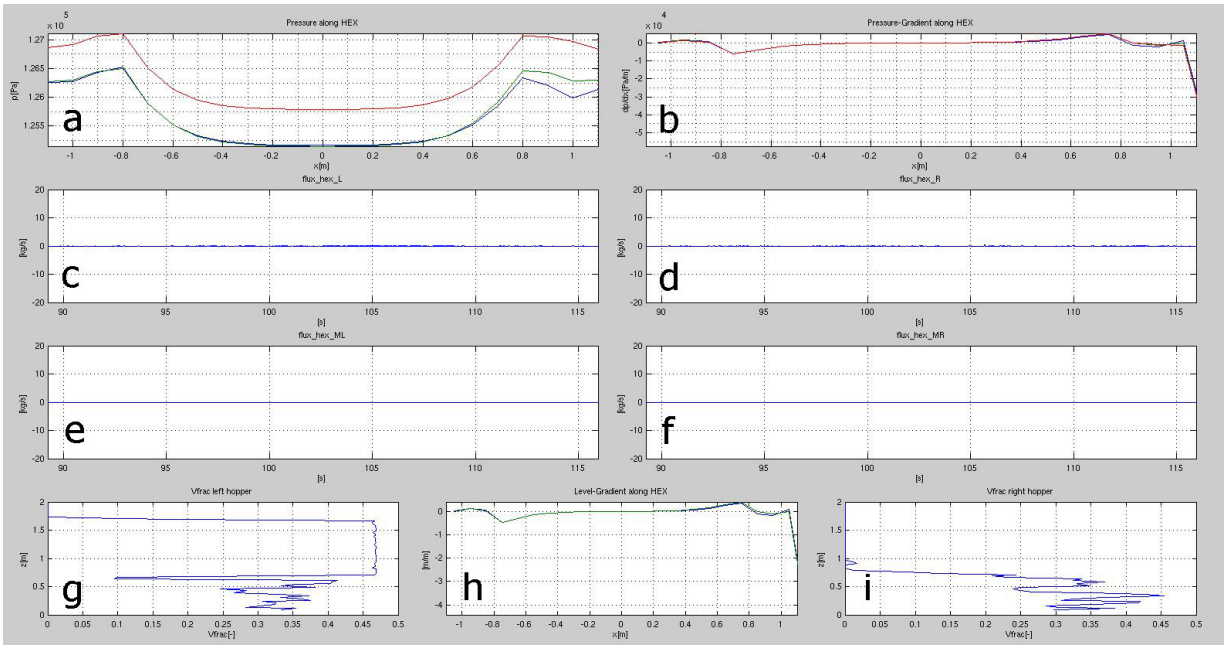

Figure 3.20.: Exemplary *Matlab controller* plot during startup - absolute pressure along HEX (and some way up into the risers, blue: current values, green: mean for the last $\approx 0.15\ s$, red: mean for 80 % of performed simulation time) **(a)**, pressure gradient along HEX (and some way up into the risers) **(b)**, particle mass flow at the first **(c)**, last / fourth **(d)**, second **(e)** and third **(f)** flux plane (from left to right), V_{frac} along left riser height **(g)**, level gradient along HEX (and some way up into the risers) **(h)**, V_{frac} along right riser height **(i)**

diagrams. It can be observed that the pressure gradient and level gradient along the HEX are somewhat redundant. As it is a typical startup plot it shows little to no particle mass flow and a bowl-like pressure curve (**figure 3.20 (a)**, blue: current values, green: mean for the last $\approx 0.15\ s$, red: mean for 80 % of performed simulation time) due to applied pressure gradients directed from the hoppers into the HEX, because while starting up low mass flows in that directions are less critical taking in account sufficient buffer volume in the (not yet fluidized) HEX. Mass flows in the opposite direction on the other hand would be problematic, potentially lowering the HEX border bed level below upper baffles and thus disabling the pressure separation between hopper and HEX. The plots showing V_{frac} along riser height are especially useful for any mode as they show progression of fluidization while starting up as well as oscillating V_{frac} and large bubbles while transporting. In some cases *pillar* instability might even lead to a collapse of the fluidized bed enforcing comparably

long re-fluidization times. The biggest advantage of the controller plots though is the ability to check on the simulation at *any* time, as transient data is logged with each and every time step of the solver. *Barracuda*'s post processor on the other depends on secific files, that are dropped in discrete time intervals and those are mostly set as long as possible by the user, as those files tend to consume a lot of disk space. The right *pillar* in **figure 3.20** for instance can be interpreted as follows: The riser is fluidized to a height of about 0.7 m, while at the top of the fluidized volume sits a large bubble and the hopper is filled to a level of about 1.75 m.

The necessary script (coded in *Python*) to connect the controller with *Barracuda* and thus achieve co-simulation would only have to alternately call the *controller* script and force the CPFD solver to reread BCs rewritten by the *controller* with a period set by the user. Unfortunately several difficulties in context with concurring software versions and system operations called by the *Python* script in combination with the server's *Linux* operations system hindered and delayed the process. The method needed for rereading BCs from the side of *Barracuda* was conveniently provided by *AixProcess*. At the point co-simulation was achieved and the efficiency of simulations was thus multiplied as they could now run with scheduled BCs and minimal maintenance enabling simulations during nights and over weekends the time assigned to this work had almost run out. It was thus one goal of this thesis to enable further simulations with the presented co-simulation method *before* running the first bench tests.

3.3.2. *Setup 7* Simulations - Corundum

Most simulations were carried out utilizing corundum powder, as it is expected to be one especially genuine choice for the AR as it offers high densities and very good bulk specific heat and thus excellent bulk energy (respectively heat) densities of around $\epsilon_{bulkAl2O3} \approx 2.7\ MJ/m^3K$ compared to quartz sand ($\epsilon_{bulkSiO2} \approx 1.4\ MJ/m^3K$). It was only later decided to run cold trials with quartz sand, as it would be easily available from the $SandTES$ prototype. Thus only the latest simulations were performed with SiO_2. *Setup 7* simulations were set up with following initial conditions (ICs) and properties:

Table 3.1.: *Setup 7* isothermal simulations' initial conditions and properties

T_{iso}	ψ_{bulk}	Min. d_p	Mean d_p	Max. d_p	Sphericity S	u_{mf}
650 $°C$	0.45	50 μm	60 μm	70 μm	1	$\approx 3\ mm/s$

All simulations presented in this work were isothermal simulations, first at minimum storage temperature ($T_{iso} = 650\ °C$) and later on at atemperature in between ambient and approximate blower outlet temperature ($T_{iso} = 37\ °C$). Thermal simulations would produce significantly lower computation rates and were decided premature as pronounced problems regarding powder transport especially in vertical direction consisted throughout this work. The same reason postponed the implementation of a tube bundle, though this should urgently be made up for in future work. For lack of precise values from literature particle sphericity was set to 1, which is not decided ideal in hindsight due to it's influence on hopper emptying. It should rather have been set to about 0.8 as was done in subsequent simulations. The value given for u_{mf} is an approximate value as it slightly (about 10 %) varies with ρ_a which is dependent on pressure.

As announced above to hopper respectively riser fluidized bed levels (left and right) of up to roughly 0.91 m particle mass fluxes were rather predictable and stable. **Figure 3.21** shows a corresponding controller plot. Due to little to no bubbling in the risers control was achieved with frequent channel pressure corrections utilizing V_{frac}-values only as explained above and respectively without the utilization of pressure differences derived from pressure checkpoints' output values. Δp_{edgeL}, Δp_{HEX} and Δp_{edgeR} were set to 3500 Pa, 0 Pa and 1000 Pa at 18.4 s simulation time and not changed afterwards. The fluidization grades (FGs) were set to (Roman numerals as depicted with each setup above) constant $FG_{VI} = 0$, $FG_I = 8$, $FG_{II} = FG_{III} = FG_{IV} = 6$, $FG_V = 8$ and $FG_{VII} = 11$ at the same time. To keep things simple, those values will be written in an abbreviated form in the following. For the stated pressure gradients and FGs that would be: Δp: |3500 0 1000| and FG: |0 8 6 8 11|. The right hand side mass flow leaving the HEX is, it seems, partially dependent on the left hand side, though delayed. This makes sense considering the particle flow's inertia. Actually a slight lowering of the left hand side pressure gradient would have been reasonable, though any change of gradients would produce some degree of unwanted

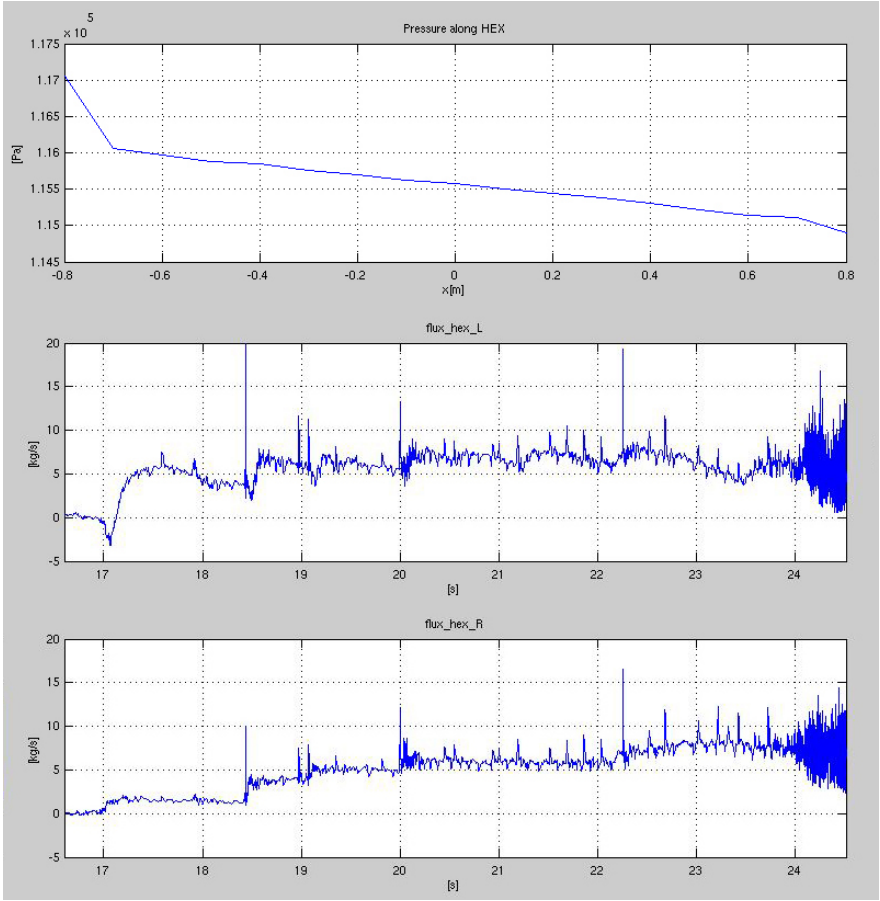

Figure 3.21.: Controlled mass flows, as obtained with *setup 7* and hopper bed levels of approximately 0.91 m, Δp: |3500 0 1000|, FG: |0 8 6 8 11| from 18.4 s

oscillation. Thus in this context and quite generally regarding those simulations, patience is feasible more often than not.

Obviously total FG regarding the left hand hopper and riser is distinctly lower than right hand side FG and still a much higher gradient is needed to transport particles out of the left hopper than into the right one. This is an observation with general validity regarding simulations presented in this work. The fact is attributed to the lift the particles receive in the risers, which is is a function of the fluidization grade (too high FG will even carry out particles and render hopper outflow impossible). Apparently this lift is directed against or into direction of transport depending on the hopper. Hence FGs for the to be emptied hopper should be set as low as possible, though it soon showed, that with higher bed levels minimum FGs of around 6 were needed to prohibit a possible collapse of the bed in consequence of oscillations according to the particle masss flow's amount due to (heavier)

bubbling. Furthermore it should be noticed, that a pressure gradient applied between HEX segments is not necessarily needed to achieve a smooth overall gradient. Nevertheless it is expected to be obligatory for a longer or curved (for example horseshoe-shaped) HEX and thus should be implemented for (modular) test benches. The reason for the rather short transport period shown in **figure 3.21**, by the way is the occurance of ratholing (it can be observed as heavy mass flow fluctuation starting at roughly 24 s). This phenomenon will be addressed in the following, as it represents a serious issue.

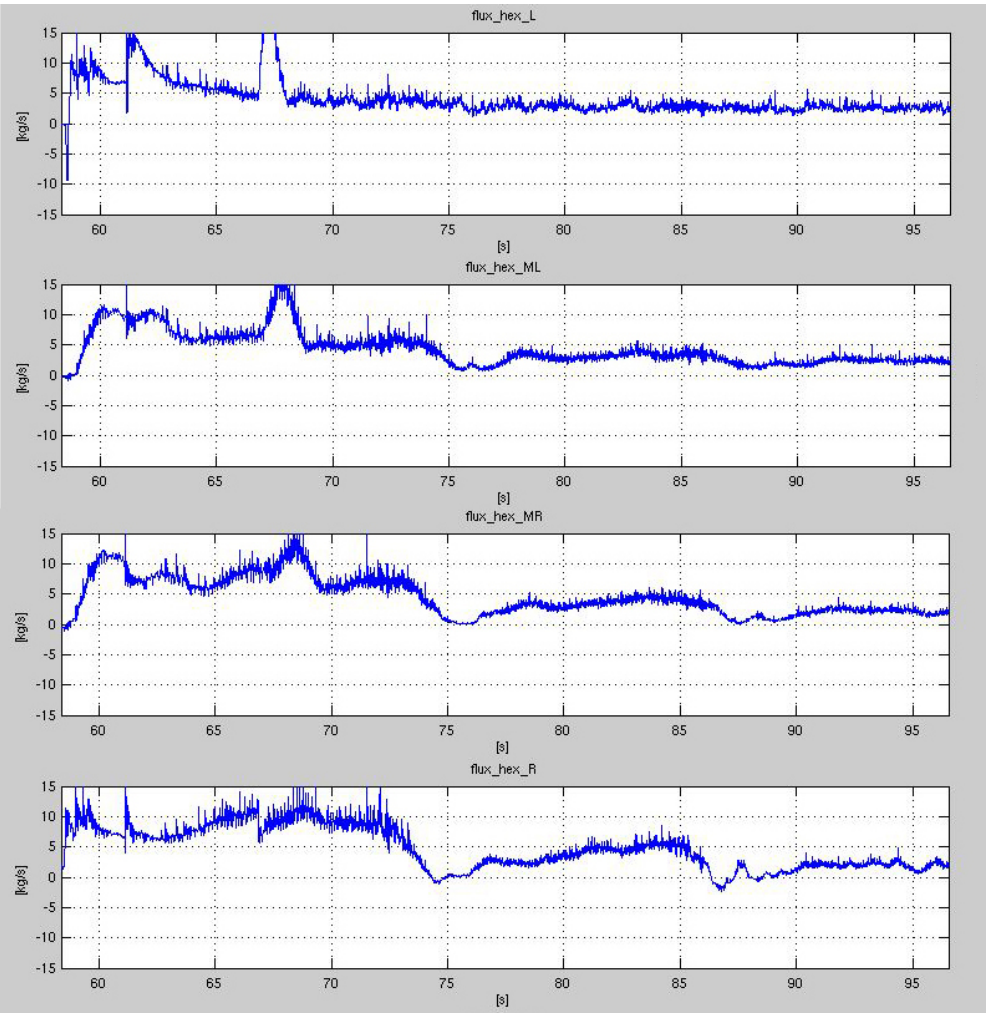

Figure 3.22.: Slow funnel flow enabling small particle mass flows, *setup 7*, $h_{L0} = 0.91\ m$, $h_{R0} = 1.7\ m$; Δp: |4200 0 6000|, FG: |6 8 6 8 12| from 66 s

It has to be stated, that small particle mass flows (roughly $\leq 3\ kg/s$) are problematic with the chosen AR HEX cross section, although the implementation of a tube bundle might have changed this. Ironically the smallest mass flows to this point were achieved as a

consequence of the occurring of another problem, namely ratholing respectively very slow funnel flow. The concerned simulation was fluidized with FG: |6 8 6 8 12| and gradients were set to Δp: |4200 0 6000| at 66 s. The resulting (left hand side) mass flow is roughly $\dot{m}_p \approx 2.4\ kg/s$ which yields a mass flux of $\Phi_p \approx 74\ kg/m^2 s$. After the observation of very slow funnel flow the simulation was continued without any control interventions, see **figure 3.22**. Though interesting this phenomenon is still useless as long as the same small mass flows can not be achieved with the other hopper as well. The scenario is shown here because it enables the illustration of two important points regarding AR particle transport. But first the mechanism of funnel flow should be shortly explained. In the theory of storage hopper and silo emptying *two* mechanisms are distinguished - *mass flow* and *funnel flow* (see [12], [13]). Which mechanism will occur depends on the powder's properties - especially it's friction angles, the silo's main and outlet diameters and the packed bed's level. The principles of both are depicted in **figure 3.23**. If funnel flow stagnates and forms a stable shaft around and above the hopper's exit it is referred to as *ratholing*.

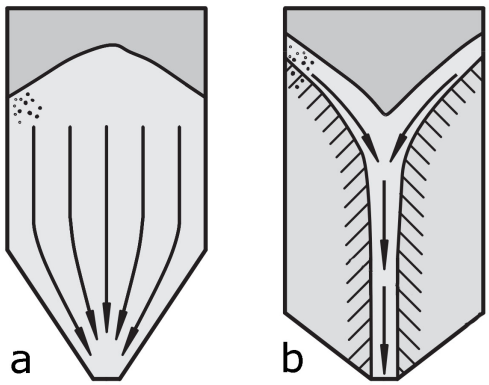

Figure 3.23.: Hopper emptying mechanisms, mass flow **(a)** and funnel flow **(b)**, [12]

For powders with rather narrow d_p-distribution, as utilized in the AR, segregation is not a major concern. Thus a funnel flow would always suffice and definitely be preferred, as in this case the fluidized powder pillar in the centre of the hopper would not interact too much with the large mass of surrounding powder. It is suspected that a mass flow regime in the hopper might even render fluidization in the desired sense impossible as the fluidized bed could be perpetually choked by not fluidized powders crashing down from all sides into the fluidized cross section. Consequentially the hoppers for the AR were designed for funnel flow with above mentioned quartz sand, as the properties of this powder were well known.

Unfortunately the properties of a matching corundum powder were not available but it was anticipated to show roughly the same behavior. It can be observed from **figure 3.24** though, there will be a difference. One might observe a funnel flow, but it is so low it should probably rather be referred to as ratholing. Moreover the hopper's level does not actually drop, as the funnel is only further hollowed out (black strokes were added to highlight this fact).

The necessary calculations for hopper emptying design were performed by Dipl.Ing. Verena Sulzgruber in accordance with two different methods from *Jenike* (upper bound) [12] respectively *Molerus* [13]. Both methods base on the calculation of a critical diameter, that has to be exceeded in order to prohibit ratholing and thus enable funnel flow. It should be remarked that this diameter is significantly larger than the critical diameter associated with *bridging* and thus the possibility of bridging was eliminated in the same step. The calculated critical diameters are $\approx 198\ mm$ (*Jenike*, upper bound) respectively $\approx 145\ mm$ (*Molerus*). The applied hopper exit diameter with the *Advanced Regenerator*'s powder silos is $250\ mm$. Furthermore with those calculations it was verified, that (as was desired) the occurrance of *mass* flow would be impossible with said quartz sand and the hopper geometry on hand, because the necessary silo cone angle is missed by almost $10\ °$. *Setup 7* though is the last setup, that was introduced before above-mentioned hopper layout calculations and thus can not be expected to empty that well, even if said quartz sand was applied. Moreover it has an elongated rectangular riser cross section with an equivalent diameter of only $\approx 218\ mm$.

To make clear above announced points above-shown simulation will be compared to a second one. They can be easily distinguished by direction of particle mass flow, as the first simulation has positive horizontal direction flow and the second simulation for once negative horizontal direction flow, as can be observed from **figure 3.25**. Firstly emptying behavior is considered. The right hand side hopper depicted in **figure 3.25** does not show a very slow funnel flow, as was shown above, but its flow does completely stop at the moment the powder formed shaft's diameter meets the diameter of the riser below. This seems irrational on first view, because the walls of the funnel are higher and steeper. On second view though it seems the only possible explanation for this case of ratholing has to be hopper associated

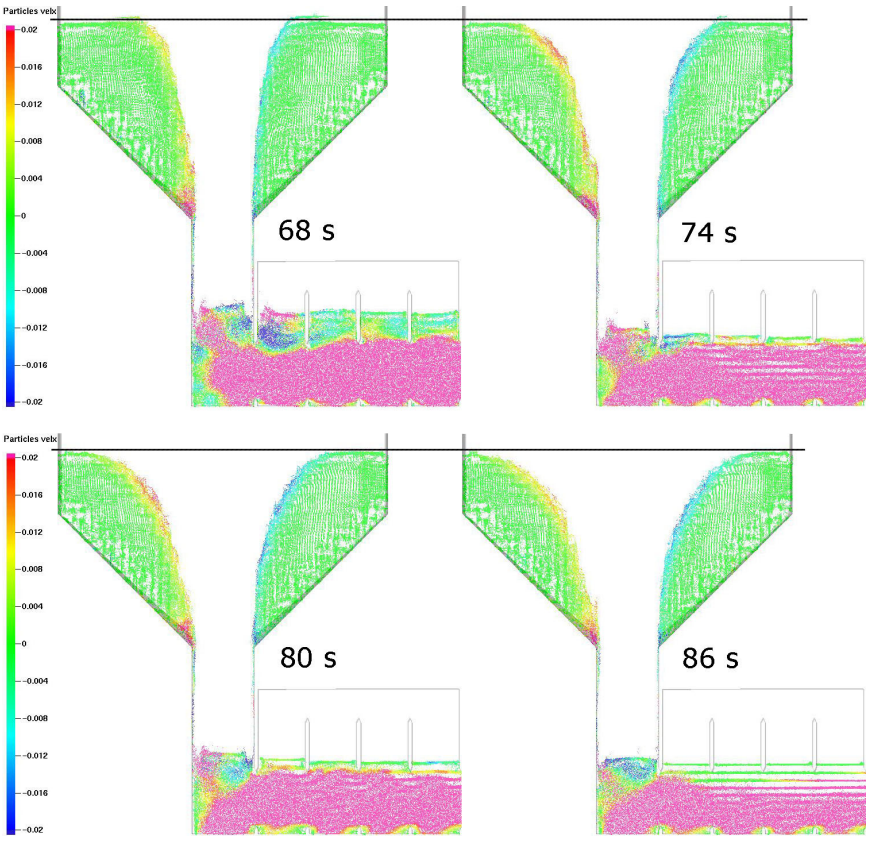

Figure 3.24.: Slow funnel flow respectively ratholing - particle velocity in horizontal direction (scale in m/s), as observed with *setup 7*, corundum and 0.91 m left hand hopper bed height, FG: |6 8 6 8 12|

fluidization grades (FG: |12 8 6 8 8| compared to FG: |6 8 6 8 12| above). It has been stated that the rising air forces a lift upon particles located in the riser, and the hopper shown in **figure 3.25** receives a roughly 14 % higher $\dot{m}_a$, which might not sound much. Although considering $\dot{m}_p$ leaving the lower funnel was already that small it might well be, those additional 14 % of air make the difference between a slow funnel flow and actual ratholing. This was observed in other simulations too and has to be kept in mind as an important fact regarding the AR's layout in general - fluidization does significantly influence emptying behavior. Indeed this shows up an additional way of controlling hopper outflow besides applied pressure gradients and also restricts hopper fluidization to certain (unknown) values depending on powder properties and desired emptying mechanism. This correlation should thus be investigated in further simulations and bench tests or alternatively a way to negate this influence has to be found.

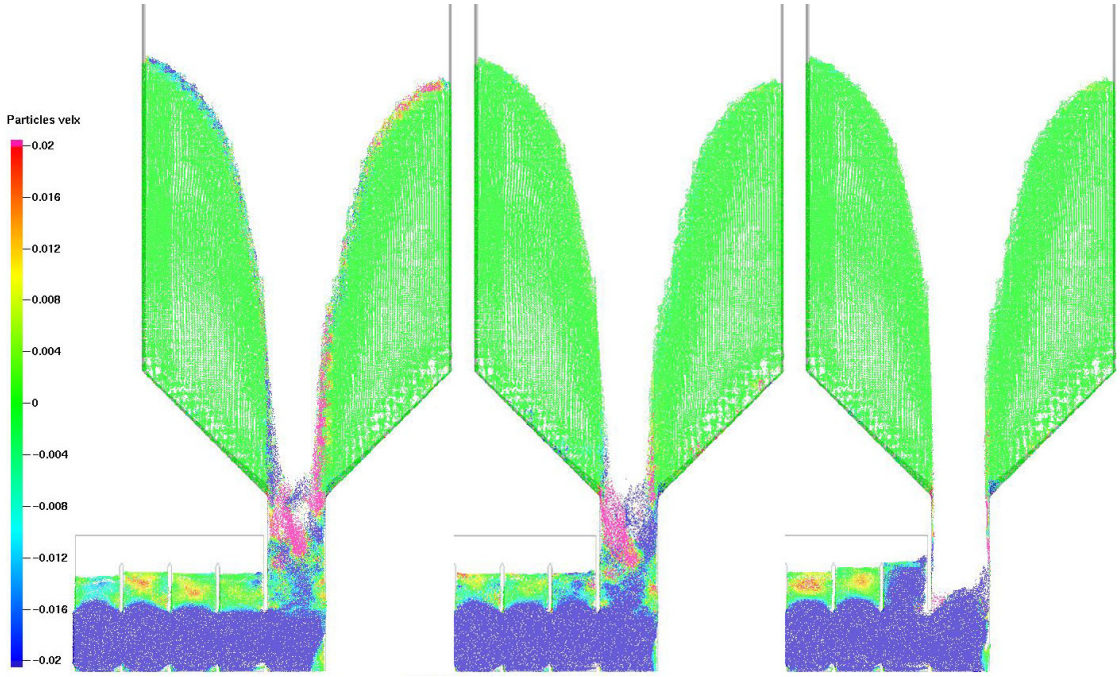

Figure 3.25.: Ratholing - particle velocity in horizontal direction (scale in m/s), as observed with *setup 7*, corundum and 1.7 m right hand hopper bed height, FG: |12 8 6 8 8|

Addressing the second point announced above, x-direction particle velocity distributions in the HEX from both simulations are compared in **figure 3.26**. Both states of flow are asymmetrical and HEX levels are partially critical, which is undesired, but that is not the point, although it is fascinating how little to nothing of the upper baffles is submerged and pressure separation is still achieved. The point is that the lower mass flux **(a)** $\Phi_p \approx 70\ kg/m^2s$ is not able to fill out the whole channel's cross section any more which means potentially inhomogeneous flow and mass flow oscillation, whereas the higher flux **(b)** $\Phi_p \approx 300\ kg/m^2s$ nicely fills up the channel. Introducing a tube bundle things might look different and lower flows could still fill the channel but nevertheless this seems to indicate that there is a range of reasonable mass fluxes Φ_p and every AR HEX's channel cross section should thus be laid out in a way that enables the desired range of nominal mass flows $\dot{m}_p$ to match this very range of fluxes.

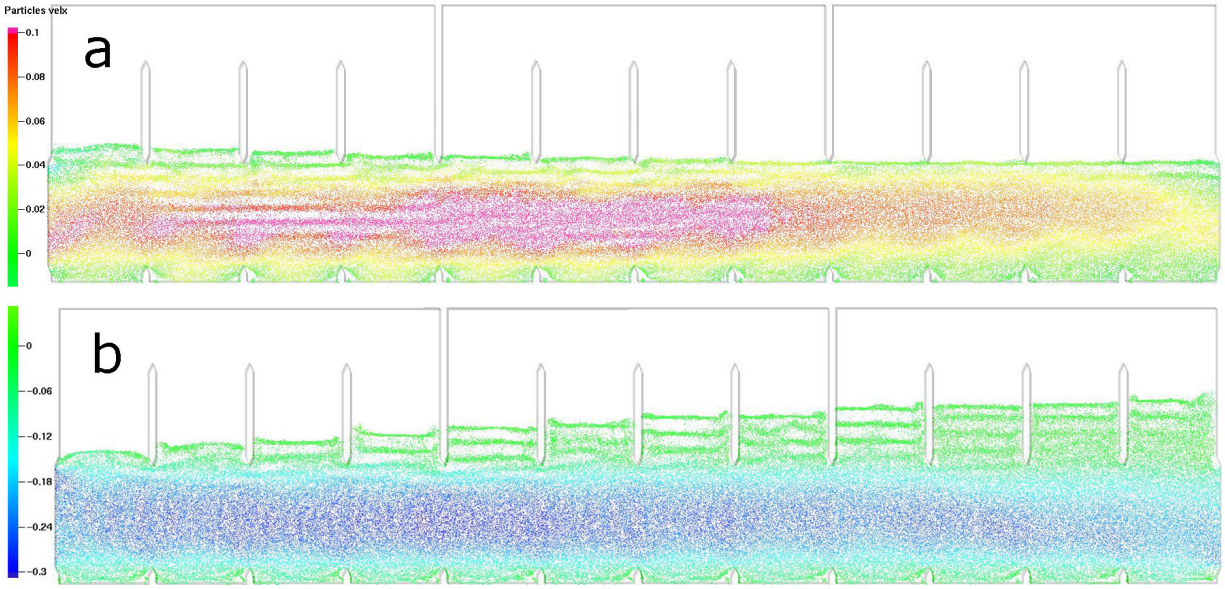

Figure 3.26.: Comparison of x-direction particle velocity distributions with $FG = 6$: $\Phi_p \approx 70\ kg/m^2s$ and Δp: |4200 0 6000| **(a)**, $\Phi_p \approx 300\ kg/m^2s$ and Δp: |-4000 0 -7000| **(b)** (reverse direction compared to a **a**)

3.3.3. *Setup 8* Simulations - Corundum

Due to reasons explained above a significant part of *setup 8* simulations were also performed utilizing corundum powders. This is convenient, as simulation results obtained with this setup, referred to as *essential geometry*, can thus be compared to results from *setup 7* on an (qualitatively) equal basis and are expected to inter alia highlight some advantages introduced by this setup. Moreover this time all simulations were performed with the same initial hopper levels h_{L0} and h_{R0}. *Setup 8* simulations were set up with the following initial conditions and properties:

Table 3.2.: *Setup 8*, corundum simulations' initial conditions and properties

T_{iso}	ψ_{bulk}	Min. d_p	Mean d_p	Max. d_p	Sphericity S	h_{L0}	h_{R0}	u_{mf}
650 $°C$	0.45	50 μm	60 μm	70 μm	0.9	$\approx 1.77\ m$	$\approx 0.72\ m$	$\approx 3\ mm/s$

As *setup 8* is expected to offer better hopper emptying behavior, due to a roughly 31 % larger *circular* riser base ($(250\ mm)^2\pi/4 \approx 0.049\ m^2$ compared to 250 mm x 150 $mm \approx 0.038\ m^2$) respectively larger equivalent hopper exit diameter, this aspect will be considered

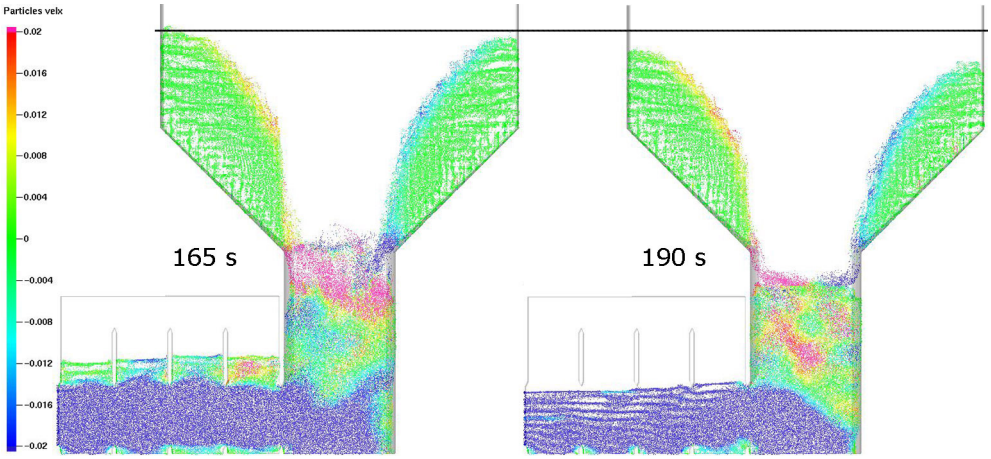

Figure 3.27.: Fast funnel flow - particle velocity in x-direction (scale in m/s), as observed with *setup 8*, corundum, *FG*: |12 10 6 10 12|

first. **Figure 3.27** depicts a hopper emptying scenario with expected funnel flow. Again a black line has been added to the figure to demonstrate the hopper level is actually falling this time (not just being hollowed out). Considering the quadratic increase of area and thus comprised mass with linear progression of the radius, it is clear that significantly higher funnel flow is offered and thus better emptying behavior. This becomes even more obvious, if the higher fluidization grades *FG*: |12 10 6 10 12| applied in this simulation are considered, as they tend to support the funnel's walls and thus reduce funnel flow, as has been stated above. So it seems that the riser's shape and diameter are another genuine way to influence AR hopper emptying behavior. It has to be kept in mind though, that a larger diameter does also mean bigger girth causing larger sinter ring $\dot{m}_a$ and also wider base causing larger riser base $\dot{m}_a$ and hence a larger overall compressor power consumption. Obviously the circle offers the best (largest) cross sectional area to girth ratio in this regard. Furthermore it can not be assumed that varying the riser diameter at will (and in a wide range) will not eventually change overall into and out of hopper transport behavior.

Figure 3.28 will at last show two other phenomena, that have been repeatedly mentioned. They are depicted in the same figure as they tend to go hand in hand, at least temporally speaking. Those are the accumulation of large bubbles and impulsive pressure reduction in the riser as a consequence of the breaking loose and then through the bed to it's surface of those first bubbles which involves the risk of a pressure equalization shock (at 63 s).

This shock clears the room below the lower edge of the baffle located at the HEX's entry, while air is flowing with high velocity in the direction of this abruptly occurring pressure gradient and thus neglects the pressure separation between hopper and first HEX segment. Moreover a possible subsequent HEX overflow as a reaction of an immoderate controller reaction should also be taken into account (at 66 s).

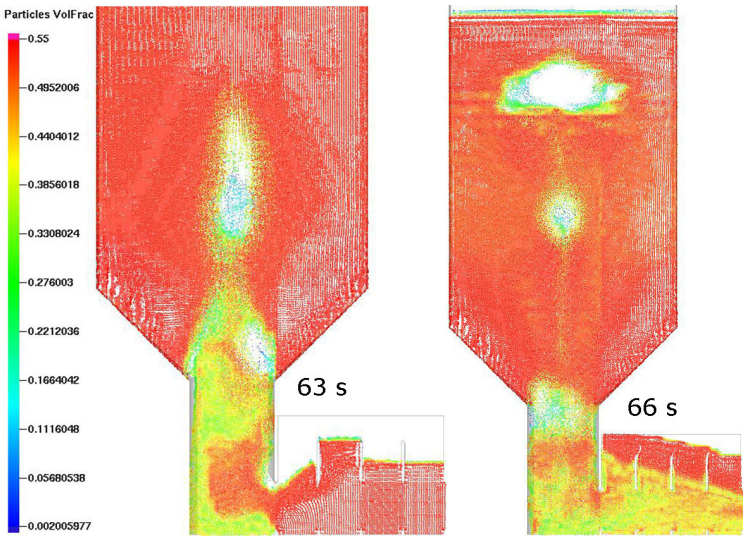

Figure 3.28.: First breaking through of large bubbles and associated risk of a pressure equalization shock (63 s) and possible subsequent HEX overflow with more bubbling (66 s), FG: |12 10 0 10 12| (63 s) respectively |12 10 6 10 12| (66 s)

The smallest particle mass flows to be realized with present HEX geometry and in this thesis are presented in **figure 3.29**. They were largely achieved by coincidence in another (failed) simulation attempt with a dysfunctional pure V_{frac}-controller which led to a successive, slow reduction of pressure gradients and thus particle mass flows $\dot{m}_p$. Fluidization grades were set to FG: |12 10 6 10 12| (which was known to be a rather solid and versatile setting at this point) and the gradients were initialized as Δp: |2000 500 1000| from the time of 82 s. In the interval of 105 to 120 s a mean mass flow of about $\dot{m}_p \approx 1.3\ kg/s$ was observed which calculates to a mass flux of $\Phi_p = 40\ kg/m^2 s$. This mass flow, though oscillating was actually more stable than expected, which again leads to the assumption that flow oscillation might be linked to impulsive change of pressure gradients as well as riser bubbling. If that is true, consequentially adjustments of pressure gradients should be applied in a continuous, smooth manner rather than discrete steps, as have been exercised in most simulations. This

topic is just one more subject requiring further examination.

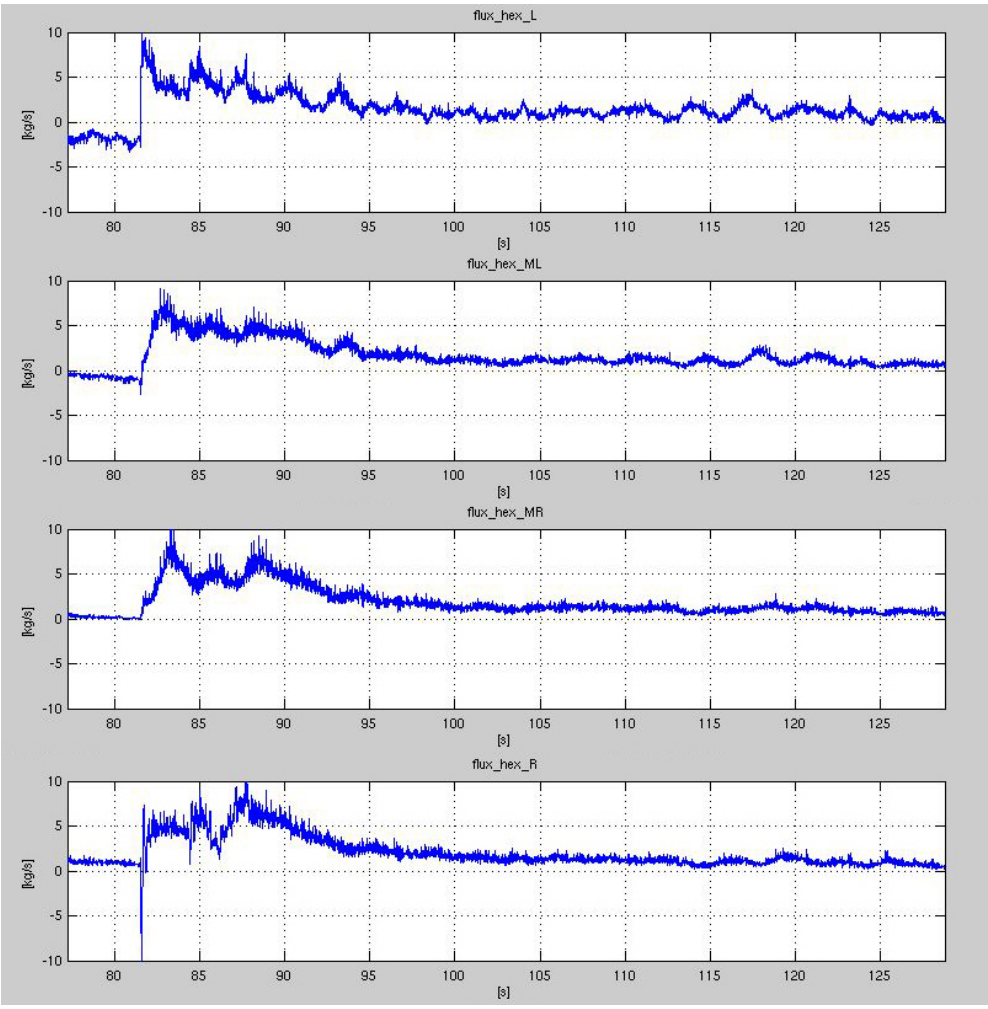

Figure 3.29.: Smallest achieved particle mass flows with corundum, *setup 8*; Δp: |2000 500 1000|, *FG*: |12 10 6 10 12| from 82 *s*

3.3.4. *Setup 8* Simulations - Quartz Sand

Finally, as the decision to run cold bench tests with quartz sand had been met, the first cold simulations were consequently also performed with that sand. Though there was a report addressing the properties of a quartz sand that was expected to be similar to the sand that was utilized in *SandTES* and would be used for the first AR bench tests at least, again no value for the sand's sphericity was offered. After some temporally restricted manufacturer research a value of 0.8 was set for sphericity. As has been stated, quartz sand was expected

to show a similar fluidization and hopper emptying behavior compared to corundum and indeed regarding fluidization it did. FGs that had been shown to be reasonable with corundum powders were now shown to more or less produce the same fluidization results with the sand as should be expected, because they were both placed at the boundary line of A and B particle groups in the Geldart diagram. Unfortunately hopper emptying behavior and thus also transport into and out of hoppers, fluidization (respectively start-up) time and even hopper fluidizability were observed to be quite different.

The *setup 8* simulations utilizing quartz sand were set up with the following initial conditions and properties:

Table 3.3.: *Setup 8*, quartz sand simulations' initial conditions and properties (with the initial hopper bed levels h_{L0} and h_{R0})

T_{iso}	ψ_{bulk}	Min. d_p	Mean d_p	Max. d_p	Sphericity S	h_{L0}	h_{R0}	u_{mf}
37 $°C$	0.53	72 μm	86 μm	100 μm	0.8	$\approx 1.77\ m$	$\approx 0.72\ m$	$\approx 7\ mm/s$

However, before addressing above stated significant problems, the influence of bubbling on the oscillation of particle mass flow absolute values will be considered once more, as there has been performed a simulation solely dedicated to the variation of fluidization grades an their impact. Very low and very high FGs were applied and although no substantial new insights were gained, at least some suspected connections could be confirmed and even better understood. One of those will be presented now. It was achieved while experimenting with very high fluidization grades and consequentially very large and numerous bubbles and a mass flow that was tried to be stabilized. The results are presented with some post processor screenshots in **figure 3.30**. Of course phenomena, due to extreme FGs, as observed with this figure have to be interpreted with some proper care. Nevertheless the central mechanism of several smaller or one large bubbles being shaped in and just above the riser and thus producing frequent short term blockades for the funnel flow can be observed very well. That funnel flow should nominally be able to come to happen in the centre of the hopper, but is compressed and strutted by an uprising bubble until at some point it gives way and the bubble can tear itself loose, puncturing the bed and making way for the funnel flow again. This process is repeated with irregular cycle period.

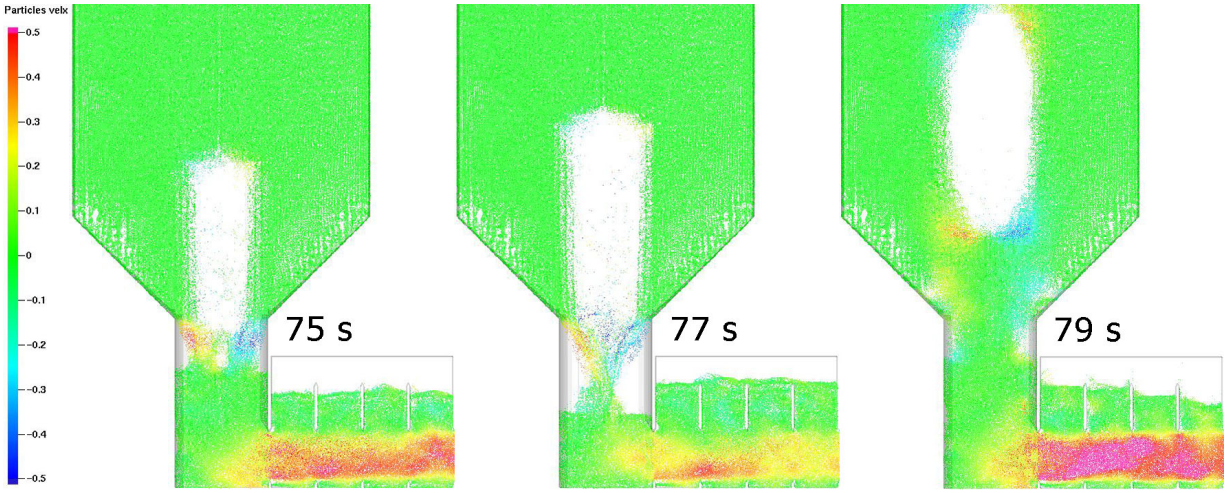

Figure 3.30.: Correlation of heavy bubbling and particle mass flow absolute value oscillation; Δp: |1000 250 200|, FG: |23 10 10 10 11|

Actually one more important thing can be gained from **figure 3.30**, as it seems that no matter what kind of hopper outflow regime was calculated by Dipl.Ing. Sulzgruber (and that calculation's results are not to be challenged here), the flow regime calculated by *Barracuda* seems to be not *funnel* but *mass* flow. Because hopper outflow seems to immediately recover after the bubble tears loose and that should not be possible with *funnel* flow as the centre of the funnel is still blocked and the funnel's walls should be static enabling only the uppermost section of the hopper's fill to slip into said funnel (as depicted in **figure 3.23**). So assuming there is no mistake in the hopper calculation yielding applied hopper exit diameter and neither with *Barracuda*'s solver, as both do seem improbable a remaining error source would be the sphericity set in the simulation. A simple approach would be some (simulation) experiments with a hopper emptying it's fill into a very large (bottomless) space to see which flow mechanism is formed in dependency of sphericity. Such was not performed out of a shortage of time, though such experiments might significantly help understanding the fluidization problems introduced by quartz sand. It is suspected that a mass flow regime in the hopper might even render fluidization in the desired sense impossible as the fluidized bed would be perpetually choked by powders crashing down from all sides. The resulting fluidization regime could well be an irregular series of large bubbles being charged with air guarded by the riser until they develop enough lift to punctuate the bed, which itself immediately fills the space in the bubble's wake.

Another theory explaining the occurrance of what seems like *mass* flow would be the bubble's supportive effect on the powder layers above. This compressed and strutted powder volume might for once carry a significant portion of its weight by itself and is additionally lifted from below effectively reducing the bed level which represents a significant influence on the flow regime, as it defines the powder load compressing the lower layers of a bed. This should probably be considered more closely.

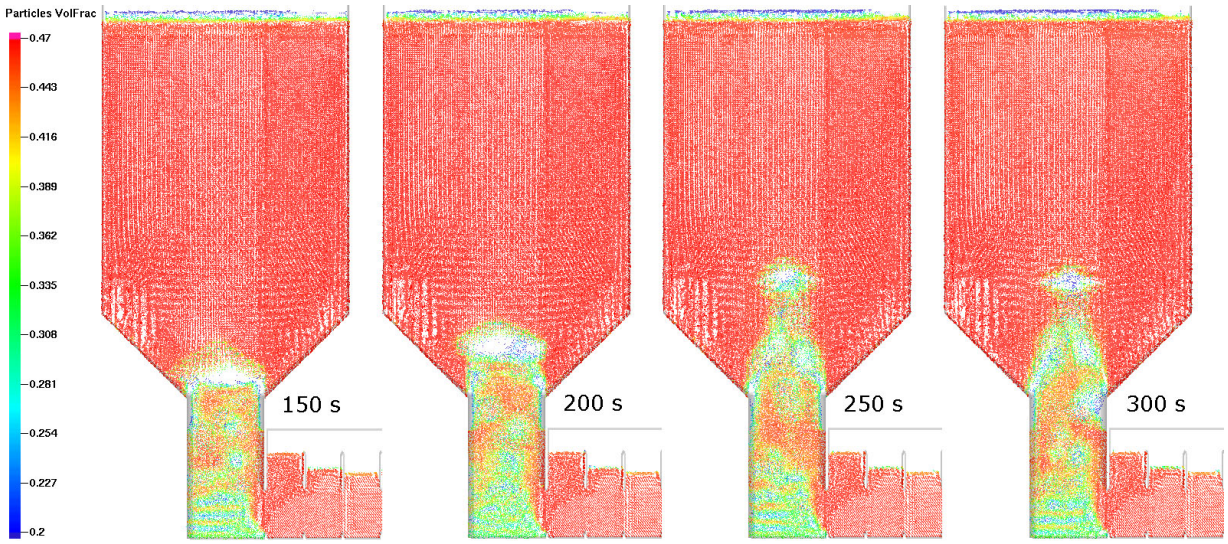

Figure 3.31.: Long term futile full left hand side hopper fluidization efforts with *setup 8* and quartz sand; *FG*: |15 13 0 10 12|

Unfortunately, as had been apprehensive of due to above-mentioned reasons, after an extraordinary long futile start-up duration of 300 *s* (corresponding to roughly one week of real time) applying maximum proven *FG*s, hoppers were found to be not sufficiently or just not fluidizable utilizing said quartz sand with *setup 8*. The ostensible reason would be the stated unexpected occurrence of *mass flow* as a dominant emptying mechanism, because fluidization progress seems to excessively slow down as soon as it first leaves the riser and enters the hopper. This can be observed from **figure 3.31**. As available simulation time was effectively running out at this point, it was decided to attempt some final simulations incorporating several mostly tube-shaped fixtures in a full hopper in an attempt to somehow achieve fluidization with quartz sand after all.

3.3.5. Evolved *Setup 8* Simulations - Quartz Sand

The evolved *setup 8* simulations utilizing quartz sand and above-mentioned tube-shaped fixtures in a full hopper were performed with a sphericity of $S = 1$ and a minimum number of computational particles, in an attempt to minimize computation times. That might not be optimal, though for the excessive shortage of remaining time, it was decided fast qualitatively crude results were preferable to no results. Those simulations were hence set up with the following initial conditions and properties:

Table 3.4.: Evolved *setup 8* quartz sand simulations' initial conditions and properties (with the initial hopper bed levels h_{L0} and h_{R0})

T_{iso}	ψ_{bulk}	Min. d_p	Mean d_p	Max. d_p	Sphericity S	h_{L0}	h_{R0}	u_{mf}
37 $°C$	0.53	72 μm	86 μm	100 μm	1	$\approx 1.77\ m$	$\approx 0.72\ m$	$\approx 7\ mm/s$

Figure 3.32 shows said tube geometries, that were implemented into the hoppers. The first one is a simple full tube without any openings (**1**), the second one features rotationally symmetric circular ring openings (**2**) and the third tube shows asymmetric openings directed away from the usual inflow during fluidization, which is usually displaced outwards from the hopper's centre. Those tubes are being referred to as *tube 1*, *tube 2* and *tube 3* in the following.

The setup with *tube 1* was flawlessly fluidized within a very short time of 33 s, which was expected due to apparent excellent containment and separation to the surrounding powder of the vertical fluidization air mass flow. Nevertheless it was shown to be incapable of genuine transport due to collapse of the right hand side hopper's fluidization and impossibility of its refluidization after a short duration of transport (at 74 s). This phenomenon is depicted in **figure 3.33** and is attributed to much higher pressure loss in the tube compared to the surrounding powder in the right hopper due to the impossibility of an equalization of tube respectively surrounding hopper bed levels with a closed tube. Fluidization grades during start-up were set to FG: |14 13 0 13 14|. During transport they were set to FG: |12 10 6 10 12| and gradients were set to Δp: |1800 100 -800| from 63 s, as the right hopper's fluidization would transport more mass then necessary by itself, because of its low bed level.

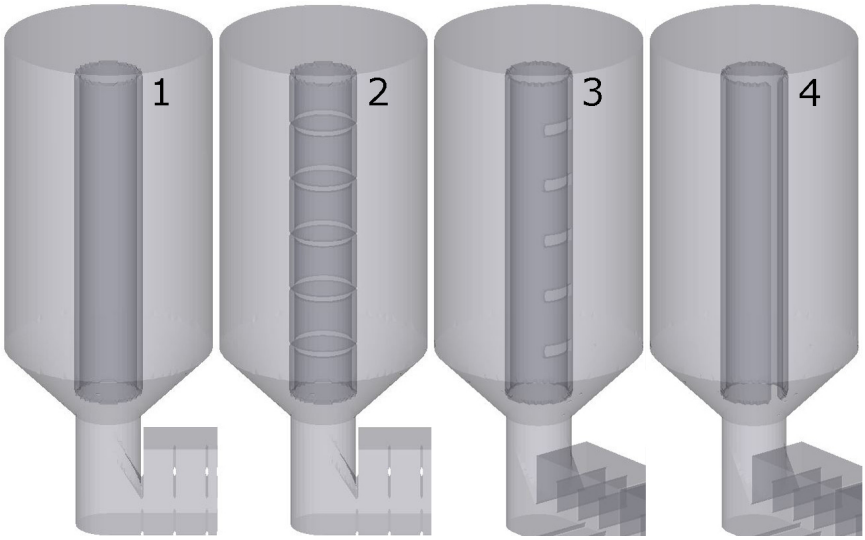

Figure 3.32.: Evolved *setup 8* tube geometries implemented into the left hopper - *tube 1*: full tube without openings (**1**), *tube 2*: rotationally symmetric openings (**2**), *tube 3*: asymmetric openings directed away from inflow (**3**), *tube 4*: vertical slot directed away from inflow (**4**)

Though mechanical closing respectively opening of the circular orifice at the tube's base in the to be charged respectively to be emptied hopper might solve this problem at the price of additional equipment. As the necessity of such additional equipment was undesired, *tube 2* was implemented with the next simulation, introducing rotationally symmetric openings in regular vertical intervals to enable equalization of bed levels.

Unfortunately *tube 2* was again found to be not sufficiently fluidizable after a futile start-up duration of 185 s. The issue is shown with **figure 3.34** and attributed to the powder contained in the tube and located above the bubble to be seen in the figure being compressed and strutted and hence effectively forming a plug due rotationally symmetric frictional locking with the surrounding tube. The fluidization grades were set as FG: |15 13 0 10 12|. As it was hoped that a dismissal of rotational tube symmetry would also disable rotationally symmetric frictional locking respectively permit a zone of less tightly compressed powder, *tube 3* featuring asymmetric openings was implemented with the next simulation.

Tube 3 finally was managed to be fluidized after 110 s of start-up and even a promising phase of transport was achieved (from about 120 s to 213 s). A state of equilibrium featuring very slow mass flows directed from each hopper to the HEX preventing HEX fluidized bed levels

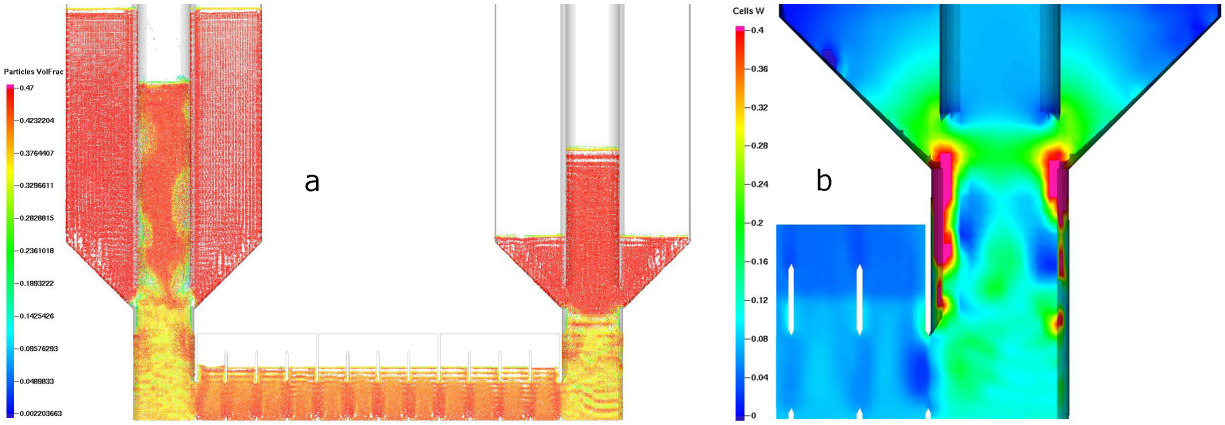

Figure 3.33.: Evolved *setup 8 tube 1* being bypassed and thus rendered incapable of genuine transport after 74 s - V_{frac}, unitless (**a**); positive z-direction fluid velocity bypass, m/s (**b**)

from falling below baffles' edges was found with Δp: |1300 0 -1300|. Thus in the following Δp-values will be given referring to this state. The break-through of first bubbles and the flow of sand through the tube's orifices are shown in **figure 3.35**. A matching controller plot depicting pressure along HEX and particle mass flows is shown with **figure 3.36**.

Applied fluidization grades during start-up were again FG: |15 13 0 10 12|. During the transport shown in **figure 3.35** the following parameters were set: FG: |12 10 7 10 12| and Δp: |1300+160 50 -1300+100| from 144 s to 167 s respectively Δp: |1300+480 100 -1300+300| from 167 s to 213 s. The slow fading of particle mass flow from 184 s is caused by a collapse of the fluidization in the right hopper roughly at the same time. This collapse is attributed to a combination of insufficient FG and again the bypass of fluidization air through the hopper fill surrounding the tube as the equalization of bed levels achieved with *tube 3* is obviously still improvable. Nevertheless this setup reacts quite well to changes of pressure gradients and the controller manages roughly constant mass flow rates (though slowly decreasing over time) with *tube 3* and control intervals of 0.5 s, which is a major breakthrough.

It was observed that a gradient ($\Delta p \approx 1300 + 1700\ Pa$) and subsequent transport directed from a to be fluidized hopper to the HEX applied at just the right moment can significantly speed up startup durations (≈ -45 %) by - it seems - creating space for the rising air respectively lowering V_{frac} of the to be fluidized packed bed. This was only achieved once

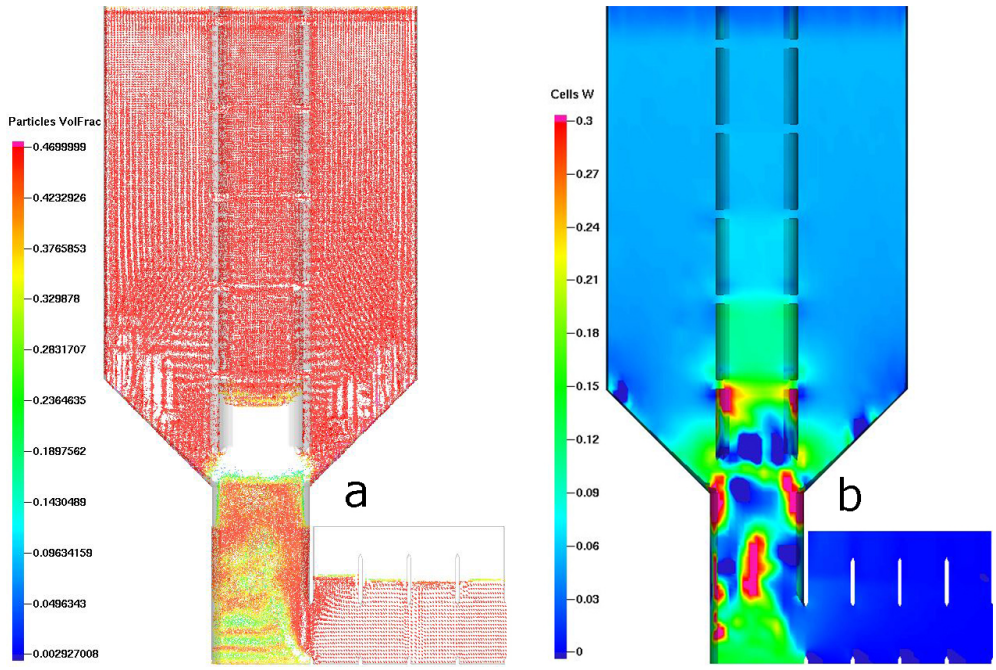

Figure 3.34.: Evolved *setup 8 tube 2* being plugged due to rotationally symmetric frictional locking with the surrounding tube after 185 s - V_{frac}, unitless (**a**); positive z-direction fluid velocity, m/s (**b**)

but should be tested in the cold trials as it may further improve the AR's flexibility taking in account moderate to long startup times as associated with presented tube-in-hopper setups. As an improvement to *tube 3*, especially regarding its still insufficient level equalization behavior, another geometry was implemented. *Tube 4* (see **figure 3.32**) features a vertical slot directed away from inflow and was thus hoped to enable continuous level equalization between the tube's fill and surrounding hopper fill, while improving or at least keeping up genuine controllability as attributed to *tube 3*.

Tube 4 was fluidized within 137 s with FG: |15 13 0 10 12|. Sphericity was again changed to 0.8 to apply more realistic powder properties with this final setup and the longer fluidization time compared to *tube 3* is attributed to this fact. Transport was initialized with FG: |12 10 6 10 12| and Δp: |1300+160 50 -1300+100| at $\approx$ 160 s. As can be observed from **figure 3.38** *tube 4* did actually further improve the quality of mass flow control as the flow is stable for a longer duration of roughly 40 s with the same control intervals of 0.5 s. *Tube 4* seems to produce a higher pressure loss (respectively viscous friction) as the same gradients do yield lower mass flows compared to *tube 3*. This higher pressure loss might

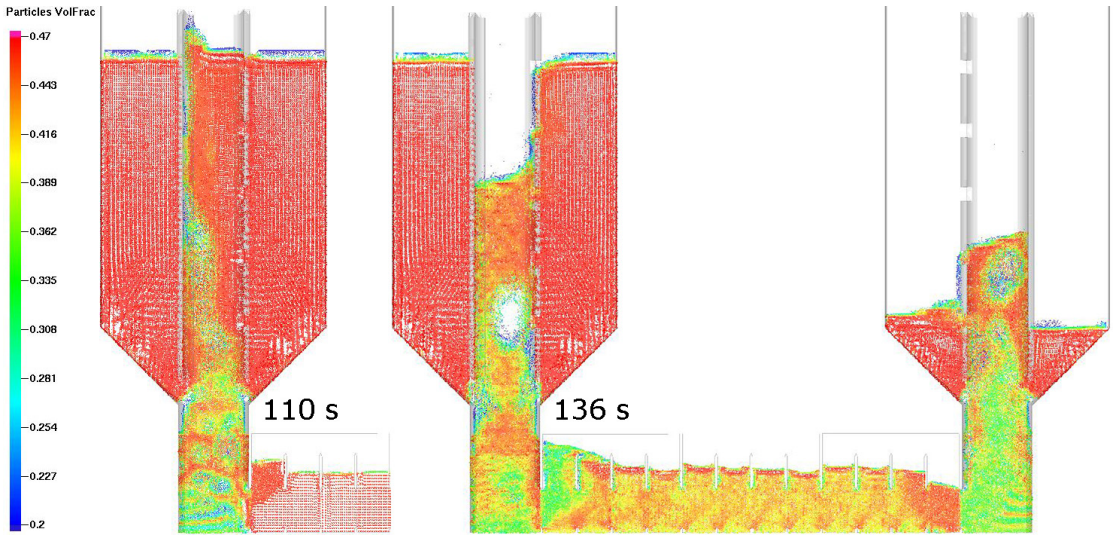

Figure 3.35.: *Setup 8 tube 3* - start-up and transport, V_{frac} - break-through in left hand side hopper at 110 s, sand is flowing through orifices at 136 s

well be the central stabilizing factor regarding transport and should not be observed with too much scepticism as the needed gradients for transport are still very small compared to the hydrostatic pressure increase along the risers. Thus a controlled and mostly stable mass flow around 0.8 kg/s was achieved, although this flow obviously ranges at the lower limits of possible flows with the chosen HEX cross section as significant horizontal (back-) mixing occurs at the HEX's entry an exit (see indigo blue regions in **figure 3.37** and negative mass flows in **3.38**).

Another period of transport with Δp: |1300+480 0 -1300+300| was performed and is shown in **figure 3.39** to verify that horizontal mixing fades with higher $\dot{m}_p$. This can be observed to be the case from the figure. Furthermore the left hopper was totally emptied after a simulation time of roughly 400 s and with maximum FGs of |12 10 6 14 16| (see **figure 3.40**). It seems FGs have to be continuously increased with the level of the to be filled hopper as its fluidization tends to collapse with rising levels. This issue might also be solved by pulsing fluidization air. Fortunately $\dot{m}_p$ seems to be not overly influenced by this increase. Nevertheless this should be investigated in further simulations as higher FGs than achievable with applied valves might be needed. ***Tube 4* or similar installations in the hoppers hence seem to present a genuine solution for the problems associated with quartz sand (and probably also other powders) and the transport into and**

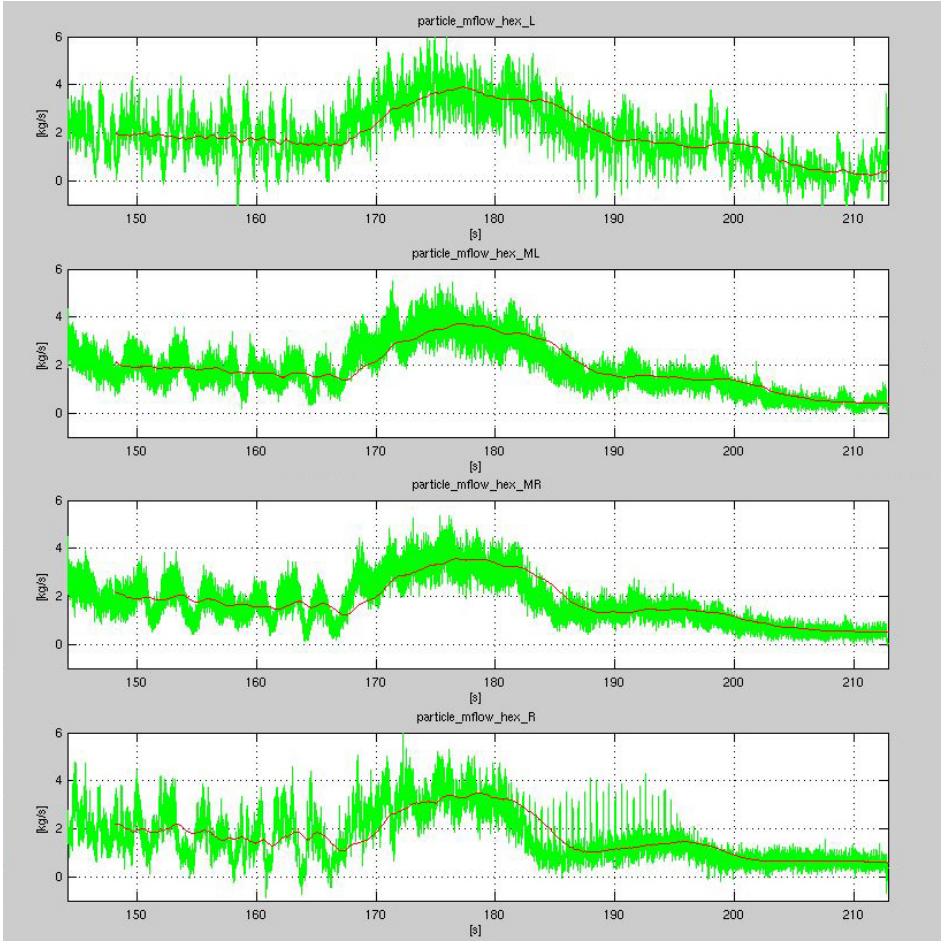

Figure 3.36.: *Setup 8 tube 3 - Matlab* controller plot between 144 s and 213 s depicting controlled particle mass flows (red: mean over ≈ 3 s), FG: |12 10 7 10 12| and Δp: |1300+160 50 -1300+100| from 144 s to 167 s respectively Δp: |1300+480 100 -1300+300| from 167 s to 213 s

out of powder storages located above the level of the HEX. However solutions like e.g. further tube geometries or a setup with submerged pipes located in *closed* tubes reaching to about one third of the tubes in the hoppers and applying fluidization there, thus disabling a bypass, as shown with **figure 3.33**, and combinations of such should also be kept in mind.

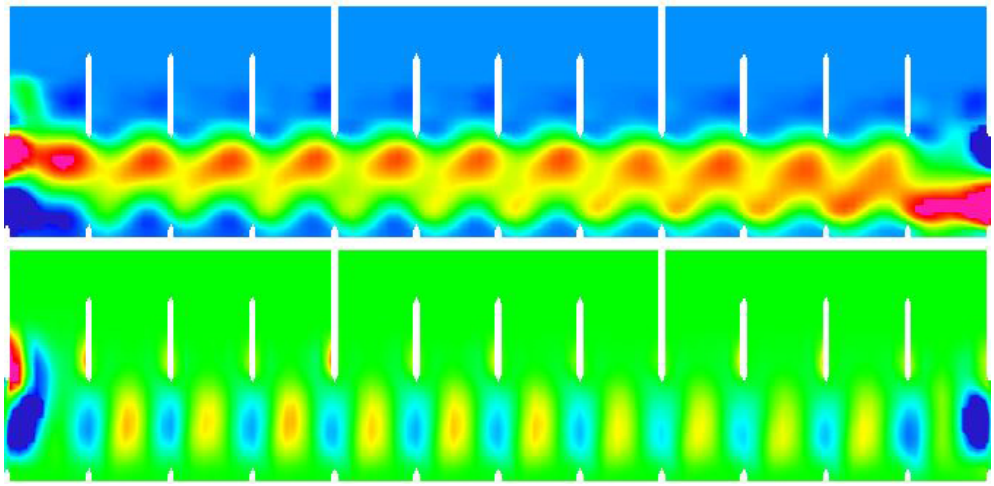

Figure 3.37.: *Setup 8 tube 4* - particle mass flows at 215 s averaged over ≈ 150 s in x- (above, indigo blue regions represent negative flow) and z-direction (below, green areas represent zero flow) to demonstrate plug flow and negligible vertical and back mixing with this final setup and minimal (thus critical) $\dot{m}_p \approx 0.8$ kg/s

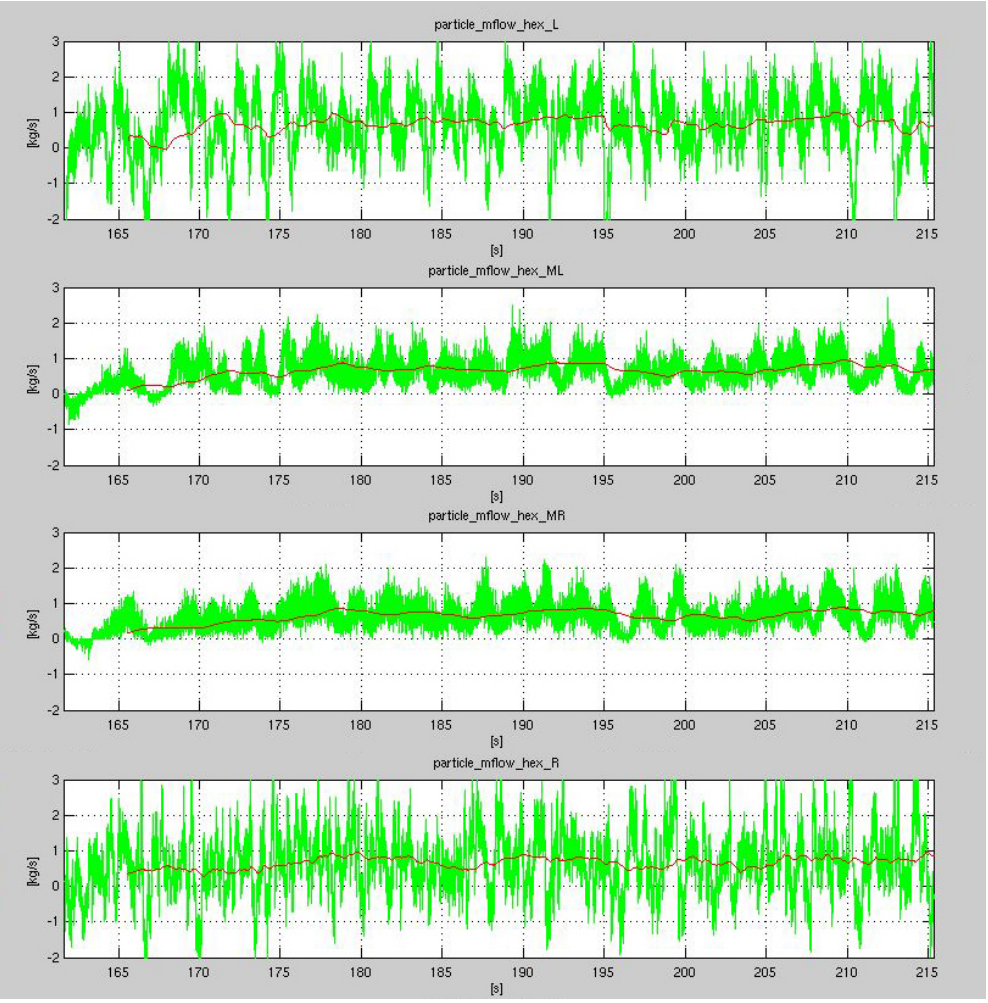

Figure 3.38.: *Setup 8 tube 4 - Matlab* controller plot between 162 s and 215 s depicting controlled particle mass flows (red: mean over ≈ 3 s), FG: |12 10 6 10 12| and Δp: |1300+160 50 -1300+100|

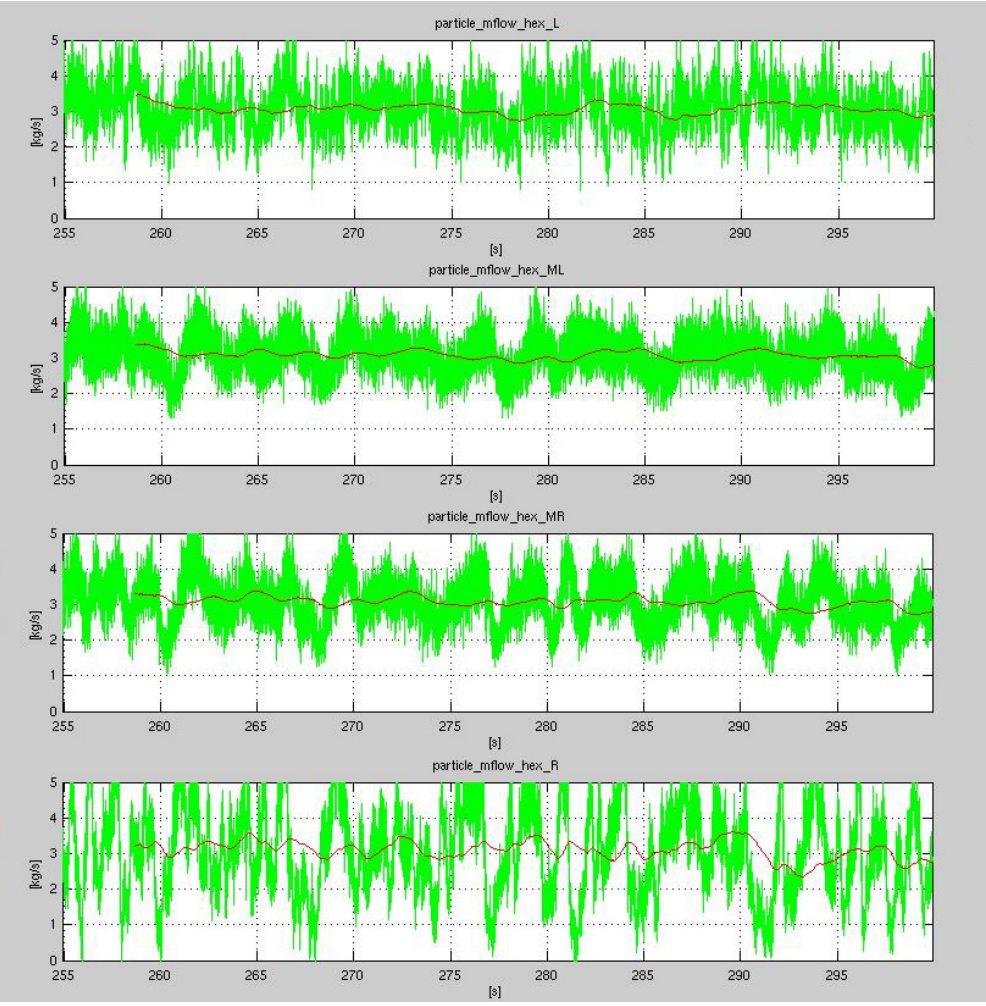

Figure 3.39.: *Setup 8 tube 4 - Matlab* controller plot between 255 s and 300 s depicting controlled particle mass flows (red: mean over ≈ 3 s), FG: |12 10 6 10 12| and Δp: |1300+160 50 -1300+100|

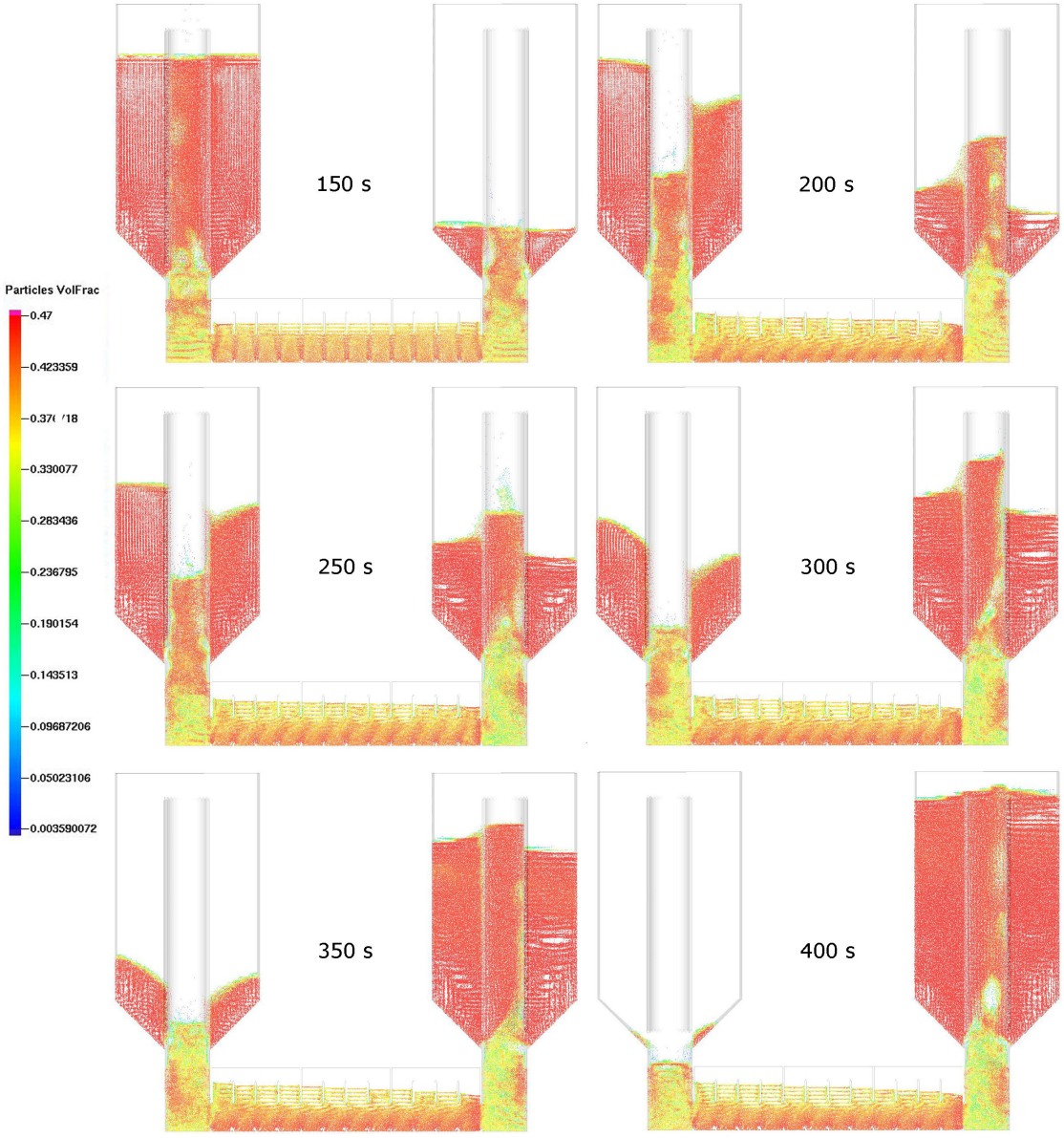

Figure 3.40.: *Setup 8 tube 4* - Total emptying of the left hopper from 150 s to 400 s at controlled mass flows of 3 kg/s respectively 0.8 kg/s

3.4. Summary and Conclusions from Simulations

This section does consist firstly of a detailed summary and secondly a short conclusion regarding performed simulations, as this chapter is the longest and most complex of this thesis. Furthermore a lot of different simulations have been presented with matching boundary conditions and numerous figures and it would thus have been very easy, especially for a reader not familiar with the topic, to be distracted from the most important facts concerning simulations. Those very facts are now to be summarized starting with the first geometry that has been implemented with *Barracuda*. The reader might want to use the embedded links to addressed figures to occasionally refresh her or his memory.

With the obvious disadvantage of *setup 1* being the impossibility of a satisfactory emptying of hoppers, in team work with Dr. Schwaiger an advanced geometry including raised rectangular hoppers with sloped floors was introduced. *Setup 2* augmented this approach with more baffles and rotationally symmetric raised hoppers, enabling better stability under internal pressures. Experimenting with baffles and positioning all upper respectively lower baffle edges at the same height, particle flow oscillation returned, but in a stable, controlled manner (**figure 3.8**) together with better HEX in and especially outflow (*setups 3, 4* and *5*). Additionally HEX mixing was thus reduced to a reasonable amount, mostly enabling a plug flow with little back or vertical mixing concluding overall HEX design. Irregular baffle spacing has been shown to decrease particle flow oscillation (and mixing) though being redundant to the effect of a higher number of baffles.

The introduction of *nozzle rings* with *setup 6* enabled the admission of maximum pressure and the larger part of $\dot{m}_a$ fed to the riser above the level of the HEX, thus using the sand filled lower riser as a buffer and brake (**figure 3.10 (b)**). The fluidization via sinter rings seemed to additionally stabilize fluidized pillars in the hoppers' centres, enshrouding them with a shaping air mantle and reducing viscous friction between pillar and actual hopper fill. *Setup 6* was the first setup to be controlled by the Matlab controller script. Also with *setup 6* utilizing corundum powder the erection of stable fluidized *pillars* within hoppers, able to perform transport into but also out of those storages, without being forced to shut down fluidization in the to-be-emptied hopper's riser and thus suffering long reaction times

when switching direction of transport, was achieved for the first time.

Regarding the stability of and the transport within those *pillars*, problems did occur with larger bed heights ($h_{bed} \geq 0.91\ m$) due to oscillating of the particle mass flows magnitude associated with pillar bubbling. Those larger bed heights are nevertheless to be tested in cold bench trials, as the maximum bed height enabling stable transport is a major limiting factor regarding the AR's application. **Thus broadly speaking the *major challenge* regarding the AR layout in this work is the difficulty of *transportation into and out of powder storages located above the level of the HEX*, necessary to enable total emptying of those storages.**

Equation 3.2 shows the isentropic (and adiabatic) power consumption of a compression of an ideal gas and was utilized to gauge and compare power demand of air compression. For the risers' fluidized beds with given heights (depending on hopper levels) and temperatures (depending on mode) and consequentially given air pressure and density above the distributor floor, the only way of reducing such power consumption is the reduction of air mass flow $\dot{m}_a$. Maintaining desired fluidization grades ($FG = u_t/u_{mf}$) the only way to reduce $\dot{m}_a$ is to reduce the riser footprints as was done. In the HEX, not bed height but its horizontal cross section is given, as desired particle mass flows $\dot{m}_p$ have to be achieved via possible mass fluxes Φ_p dependant on the HEX's cross section in flow direction. Hence HEX compressor power can only be reduced through optimization of the beds' height-to-breadth ratio h_{bed}/b_{bed} as the HEX's length is given by a needed tube bundle's surface and consequentially length. As the staggered tube bundle should consist of at least three vertical layers of a minimum tube diameter (of 25 mm) to later on enable scaling of results (**figure 3.11**), a minimum bed height was deduced. For the AR HEX this procedure resulted in a height-to-breadth ratio $h_{bed}/b_{bed} \approx 0.5$ with a transport cross section of roughly 130 mm x 250 mm. The resulting rectangular riser footstep again led to unfavorable emptying behavior and unstable fluidized pillar geometry as this structure is charged with a surface load. Because a square base would have led to unnecessarily large riser footprints, cylindrical risers were re-introduced with *setup 8*. Thus was completed the *essential setup* of the AR except of installations inside the hoppers addressing emptying and charging issues.

In the theory of storage hopper and silo emptying *two* mechanisms are distinguished - *mass*

flow and *funnel flow* (**figure 3.23** ,[12, 13]). If funnel flow stagnates and forms a stable shaft it is referred to as *ratholing*. For powders with rather narrow d_p-distribution, as utilized in the AR, segregation is not a major concern. Thus a funnel flow would always suffice and be preferred, as in this case the fluidized powder pillar in the centre of the hopper would not interact too much with the large mass of surrounding powder. Consequentially the hoppers for the AR were designed for funnel flow with above mentioned quartz sand, as the properties of this powder were well known. Necessary calculations for hopper emptying design were performed by Dipl.Ing. Verena Sulzgruber in accordance with two different methods. The calculated critical diameters were $\approx 198\ mm$ (*Jenike*, upper bound, [12]) and $\approx 145\ mm$ (*Molerus*, [13]). Those diameters were significantly larger than those associated with *bridging* and thus bridging was eliminated in the same step. The applied hopper exit diameter with the *Advanced Regenerator*'s powder silos is $250\ mm$. With those calculations it has been verified, that the occurrance of *mass flow* would be impossible with said quartz sand and chosen hopper geometry, because the necessary silo cone angle was missed by almost $10\ °$. It is suspected that a mass flow regime in the hopper might render fluidization in the desired sense impossible, as the fluidized bed would be perpetually choked by powders crashing down from all sides. It has been observed in several simulations though, that fluidization does significantly influence emptying behavior (rising air forces a lift upon particles located in the riser). This shows up an additional way of controlling hopper outflow besides applied pressure gradients and also restricts hopper fluidization to certain (unknown) values depending on powder properties and desired emptying mechanism.

Setup 8 was hence observed to offer better hopper emptying behavior, due to that roughly 31 % larger *circular* riser base respectively larger hopper exit diameter of $250\ mm$. A larger diameter does also mean bigger girth causing larger sinter ring $\dot{m}_a$ and also wider base causing larger riser base $\dot{m}_a$, resulting in a larger overall compressor power consumption. Obviously the circle offers the best (largest) cross sectional area to girth ratio in this regard.

Most simulations were carried out utilizing corundum powder, as it offers high densities and very good bulk specific heat and thus excellent bulk energy (respectively heat) densities of around $\epsilon_{bulkAl2O3} \approx 2.7\ MJ/m^3K$ compared to quartz sand $\epsilon_{bulkSiO2} \approx 1.4\ MJ/m^3K$. It was only later decided to run *cold* trials with quartz sand. All simulations were performed

as isothermal simulations, first at minimum storage temperature ($T_{iso} = 650\ °C$) and later on at a temperature in between ambient and approximate blower outlet temperature ($T_{iso} = 37\ °C$).

It has been observed during transport directed from left to right, that right hand side particle mass flow leaving the HEX seems partially dependent on the left hand side, though delayed. This makes sense considering the particle flow's inertia. Moreover total FG regarding the left hand hopper and riser is distinctly lower than right hand side FG and still a higher gradient is needed to transport particles out of the left hopper than into the right one (at similar hopper levels). This is an observation with general validity regarding simulations presented in this work. The fact was attributed to the lift particles receive in the risers, which is a function of the fluidization grade, as this lift is directed against or into direction of transport (too high FG will even carry out particles and render hopper outflow impossible). It showed, that (especially with higher bed levels) minimum FGs (of around 6) were needed to prohibit a collapse of the bed in the to be emptied hopper. Furthermore a pressure gradient applied between HEX segments is not necessarily needed to achieve a smooth overall gradient. It is expected to be obligatory for a longer or curved (for example horseshoe-shaped) HEX though and thus should be implemented for (modular) test benches.

It has been observed, that small particle mass flows (roughly $\leq 2\ kg/s$) are problematic with the chosen HEX cross section. The implementation of a tube bundle might change this. The smallest mostly stable particle mass flow to be realized in this thesis was $\dot{m}_p \approx 1.3\ kg/s$ with a resulting $\Phi_p = 40\ kg/m^2s$ (the largest stable mass flow was $\Phi_p \approx 300\ kg/m^2s$). It was observed, that particle flow amount oscillation might be linked to impulsive change of pressure gradients as well as riser bubbling. Consequentially adjustments of pressure gradients should be applied in a continuous, smooth manner rather than discrete steps, as have been exercised in most simulations. Moreover it seemed that there is a range of reasonable (respectively optimal) mass fluxes Φ_p associated with a chosen HEX cross section (**figure 3.26**) and that cross section should thus be laid out in a way that enables the desired range of nominal mass flows $\dot{m}_p$ to match this very range of fluxes.

An impulsive pressure reduction in the riser as a consequence of the breaking loose and then

through the bed of first bubbles has been noted to possibly result in a pressure equalization shock (**figure 3.28**). Such a shock clears the room below the lower edge of the baffle located at the HEX's entry associated with the concerned hopper, in the direction of this abruptly occurring pressure gradient and neglects the pressure separation between hopper and next HEX segment.

*FG*s that had been shown to be reasonable with corundum powders were shown to more or less produce the same fluidization results with quartz sand as should be expected. Hopper emptying behavior and thus also transport into and out of hoppers, fluidization (respectively start-up) time and even hopper fluidizability were observed to be quite different though. The influence of bubbling on the oscillation of particle mass flow absolute values has been attributed to several smaller bubbles or one large bubble being periodically shaped in and just above the riser before tearing loose and thus producing frequent short term blockades for the funnel flow (**figure 3.30**). This seemed to be a lot more manifest with quartz sand and this fact in unison with observed emptying while funnel flow was still blocked led to the assumption, that against all odds *mass flow* dominated hopper emptying while utilizing quartz sand with *setup 8* in *Barracuda*.

After an extraordinary long futile start-up duration of 300 s applying maximum proven *FG*s, hoppers were decided to be not sufficiently fluidizable utilizing quartz sand with *setup 8* (**figure 3.31**). The assumed reason is the stated unexpected occurrence of *mass flow* in this constellation. As the available time was running out, it was decided to attempt some final simulations incorporating tube-shaped fixtures in a full hopper ((**figure 3.32**)) in a last attempt to achieve fluidization with quartz sand after all.

Tube 1 was flawlessly fluidized within a time of 33 s, expected due to genuine separation to the surrounding powder. It was shown to be incapable of transport though, because of a much higher pressure loss in the tube compared to the surrounding powder in the to be charged hopper after a short duration of transport. The reason is the impossibility of an equalization of tube respectively surrounding hopper bed levels with a closed tube (**figure 3.33**). *Tube 2* was implemented introducing rotationally symmetric openings to enable such equalization of bed levels. This tube was also decided to be not sufficiently fluidizable after a futile start-up duration of 185 s, attributed to the powder contained in the tube

being compressed and effectively forming a plug due to rotationally symmetric frictional locking with the tube (**figure 3.34**).

It was hoped that a dismissal of rotational tube symmetry would also disable rotationally symmetric frictional locking. Hence another tube - *tube 3* - featuring asymmetric openings directed away from the usual orientation of inflow was implemented. This installation was managed to be fluidized after 110 s and a phase of promising transport was achieved (**figure 3.35** and **3.36**). A state of equilibrium was found with Δp: |1300 0 -1300| and a collapse of the fluidization in the right hopper was attributed to a combination of insufficient FG and the bypass of fluidization. The equalization of bed levels achieved with *tube 3* had to be improved still. Nevertheless this setup reacted quite well to changes of pressure gradients and roughly constant mass flow rates (though slowly decreasing over time) were achieved - a major breakthrough. It was observed that a gradient directed from to be fluidized hopper to HEX applied at the right moment can significantly speed up startup durations (≈ -45 %).

As an improvement of still insufficient level equalization *tube 4* (**figure 3.32**) was implemented. It features a vertical slot directed away from inflow and was created for continuous level equalization between the tube's fill and surrounding hopper fill, while further improving controllability. *Tube 4* was fluidized within 137 s. Sphericity was again changed to 0.8 to apply more realistic powder properties with this final setup. Longer fluidization times compared to *tube 3* were attributed to this fact. Mass flow control did further improve with *tube 4* (**figure 3.38**) as the flow was stable for a duration of roughly 40 s. *Tube 4* seemed to produce a higher pressure loss (respectively viscous friction) as the same gradients did yield lower mass flows compared to *tube 3*. This higher pressure loss might well be the central stabilizing factor regarding transport. Needed gradients for transport were still small compared to hydrostatic pressure increase along the risers.

Thus a controlled and mostly stable mass flow around 0.8 kg/s was achieved. This flow ranges at the lower limits of possible flows with the chosen HEX cross section as significant horizontal (back-) mixing occurred at the HEX's entry an exit (**figure 3.37** and **3.38**). Another period of transport was performed to verify that horizontal mixing fades with higher $\dot{m}_p$ (**figure 3.39**). This assumption was verified. The left hopper was totally emptied

after a simulation time of roughly 400 s (**figure 3.40**). It seemed that FGs had to be continuously increased with the level of the to be filled hopper as its fluidization tended to collapse with rising levels. This issue might also be solved by pulsing fluidization air. $\dot{m}_p$ seemed to be not overly influenced by this increase. Nevertheless this should be investigated in further simulations as higher FGs than achievable with applied valves might be needed.

***Tube 4* or similar installations in the hoppers hence seem to present a genuine solution for the problems associated with quartz sand (and probably also other powders) and the transport into and out of powder storages located above the level of the HEX.** However solutions like e.g. further tube geometries or a setup with submerged pipes located in *closed* tubes reaching to about one third of the tubes in the hoppers and applying fluidization there, thus disabling a bypass (**figure 3.33**), and combinations of such should also be kept in mind.

The results of simulations performed in context with this work have thus been summarized and several solutions for the posed problems and issues have been proposed. It is concluded though, taking in account the mass flows and fluidization respectively hopper emptying regimes that were achieved in various simulations utilizing corundum, there should be a way to enable successful operation with *setup 8* and quartz sand (or potentially other powders) by further varying powder properties and hopper exit diameter, effectively influencing emptying behavior. Such success might though require further research and understanding regarding above-mentioned phenomena and processes acquired via further simulations or cold bench tests and the former would be recommended to reduce the risk of premature investments. This might be especially appropriate considering the fact, that a convenient and time efficient method for controlled co-simulation of such processes has been prepared but not exhausted due to a delayed implementation and successive lack of time in this work.

4. Test Bench Layout

This chapter will attempt to implement the evolution of AR geometry and the fluidic and procedural calculations and conclusions from simulations in general, both addressed to in the last chapter and appendices, into an actual constructional layout process. As all of the CAD drawings and drafts, genuine constructional know-how and several calculations (especially those pertaining to process engineering), to be presented in this chapter and associated appendices have been contributed by Dipl.Ing. Verena Sulzgruber, those parts are to be declared as such and do deserve my very special thanks. Thus many figures and calculations as introduced in the following (and in the appendices) will be labeled with her name. Dipl.Ing. Sulzgruber studied process engineering at the TU Vienna, acquiring especially substantiated knowledge in apparatus and fluidized bed engineering and graduated in September 2014. Her master's thesis is listed in the literature to the work on hand, [14].

The processes and challenges in transposing the knowledge and conclusions achieved to this point into an actual constructional layout will not be addressed here in detail, but were achieved in productive teamwork of Dipl.Ing. Sulzgruber and the author to this work. On the contrary only not dimensioned views will be shown in the following figures and constructional aspects and details will mostly be addressed in an exemplary manner. Dimensioned layout drafts can be found in **appendix C**. Furthermore the AR's experimental approach will be addressed with a two-phase concept:

- firstly the *cold* trials (approx. 25 $°C \leq T \leq 350$ $°C$) and
- secondly the *hot* trials (approx. 350 $°C \leq T \leq 850$ $°C$).

Consequentially this chapter is split in the **sections 5.3.1** addressing the *cold* and **5.3.2** addressing the *hot* test rig. Thus **section 5.3.1**, dealing with the cold test facility to

be manufactured in a near future will accomplish a mostly complete procedural and constructional layout, while **section 5.3.2** will only address the most critical components and procedural calculations regarding the hot test rig, that were decided potential financial or procedural bottlenecks. This was decided due to the fact that process factors and results achieved with the cold test bench are meant to be utilized for the hot bench's final layout, as has been mentioned above.

4.1. Cold Test Rig

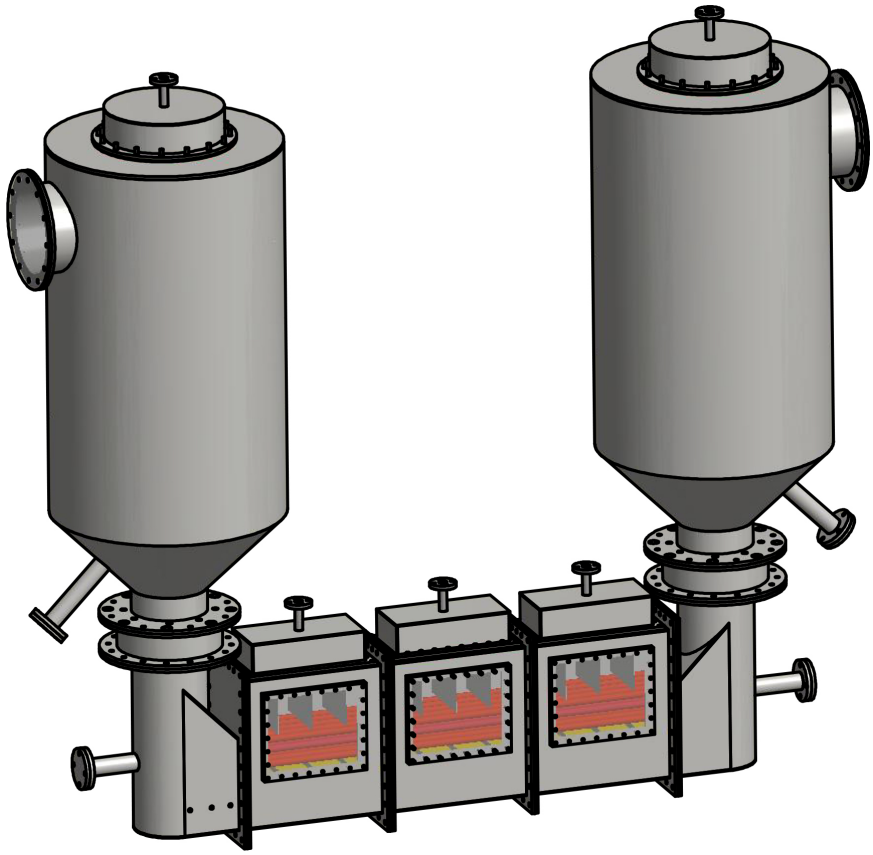

Figure 4.1.: 3D view of the Advanced Regenerator cold test rig, sintered elements are yellow, tube bundle is red; by V. Sulzgruber

First and foremost the rather complex AR geometry referred to as *essential geometry* had to be realized with actual welded steel casings flanged together in a way, that enabled accessibility of all crucial parts without altering the simulated interior seen by the powder in a way that would possibly impede flow and particle transport in general. The **figures 4.1**

and **4.2** depict the AR cold test rig in a 3D view, a frontal sectional view and frontal and horizontal projections. It can be observed, that the *essential geometry* has been slightly modified to enable a modular construction. This modular approach is meant to enable maximum flexibility with cold trials as there can be installed three, two or even only one HEX element and none, only one or both fluidized rings in the risers. Furthermore flanged HEX segments enable total access to the HEX's transport channel to allow installation of various dummy geometries for tube bundles or heating rods (tube bundle as depicted in **figure 3.11** is drawn in red) to test their influence on the inherent flow. Even large fittings shaped as beveled boxes might be installed to change the overall cross section of the channel. Furthermore plexi glass windows are installed in the upper hoppers and the HEX to enable optical observation of the processes taking place within. The hoppers' internal height from the distributor floor to the top is set to roughly 2 m to be able to validate (or refute) even failed simulations. Hopper diameter is 800 mm, the HEX segments are roughly 500 mm long, 630 mm high and 250 mm deep with a channel cross section of about 250 mm x 130 mm (in between baffles), resulting in a footstep of about 2600 mm x 800 mm. Again, actual dimensioned drafts are to be found in **appendix C**.

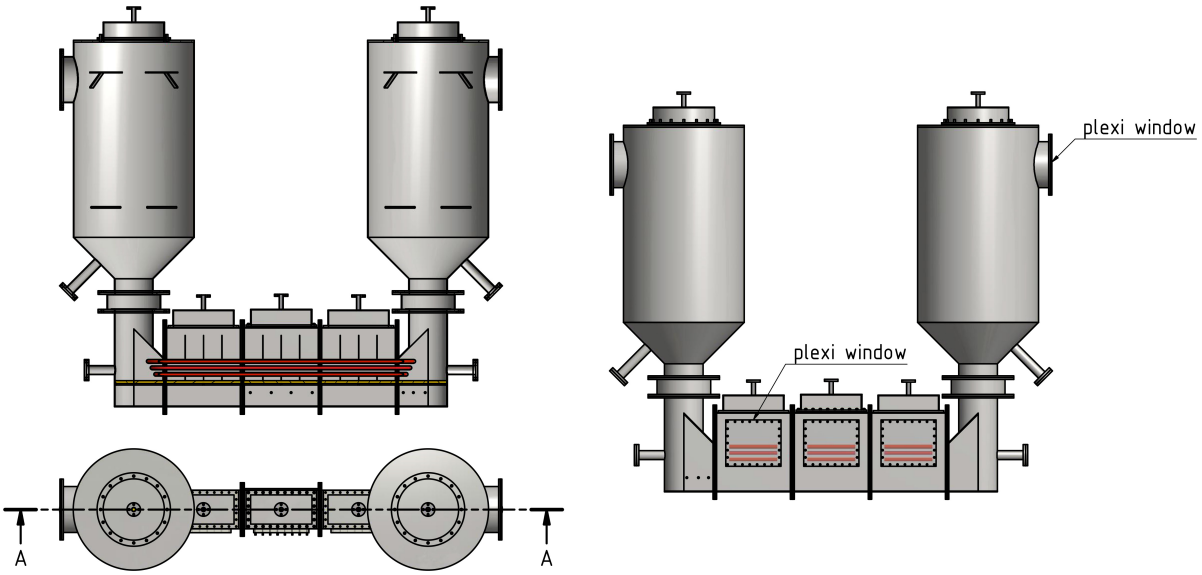

Figure 4.2.: Frontal sectional view and frontal and horizontal projections of the Advanced Regenerator cold test bench, sintered elements are yellow, tube bundle is red; by V. Sulzgruber

Above mentioned slight modification of the AR interior regarding fluidization and particle

flow are for once about 30 mm wide not fluidized stripes transversal to flow direction located along the HEX due to the HEX's flanging. Those are not expected to pose any problems, as the lower baffles in the simulations' geometries are also 10 mm wide and fluidized beds generally tend to expand in positive vertical direction (due to pressure decrease respectively gas expansion). Another variation is the compared to the *essential setup* elongated transition from HEX to riser needed to gain sufficient space for flange accessibility. As this roughly 60 mm long section is fluidized, there are not expected any problems emanating from this variation. Though the risers' distributor floors' fluidization grades FG_{ris} (as said section is located outside the HEX) are to be reduced by a factor A_{old}/A_{new} to achieve the same riser air mass flow $\dot{m}_a$ as applied in the simulations.

Moreover calculations concerning the stability of the cylindrical hoppers taking in account internal pressure and surface load due to the powder fill, steel and especially plexi glass disks under internal pressure and the conical transition from riser to hopper under internal pressure and powder load were performed by Dipl.Ing. Sulzgruber. In this context the standards DIN EN 1991-4:2010-12 and DIN EN 13445-3:2015-12 were utilized. All of above-mentioned elements' thicknesses were shown to be more than sufficient with the only exception of the plexi glass windows, which were dimensioned with a thickness of $s_{plexi} = 20\ mm$ due to their calculation's results regarding minimum thickness.

4.1.1. Sintered Elements

Secondly the distributor floors and rings, assumed as perfectly homogeneously flowed through surfaces to this point had to be realized constructionally. Those elements would have to provide a pressure loss higher than any pressure variation occurring above, while prohibiting particles from intrusion and potentially clogging. Fortunately that problem had already been addressed and the solution been validated in tests during *SandTES*' layout process. This solution are sheets of sintered metal, as they are available with various thicknesses, porosities (average pore diameter in μm) and even as sintered tubes (for the fluidized rings in the risers) enabling various pressure losses (in dependency of transition velocity) and hoped for immunity to clogging (with porosities ranging far below particle diameters to

be applied). Moreover, sintered metal sheets were also applied as particle filters before pressure control valves. See **appendix A.4** for related calculations and **appendix ??** for a data sheet. Detailed views of concerned sections are shown with **figure 4.3**.

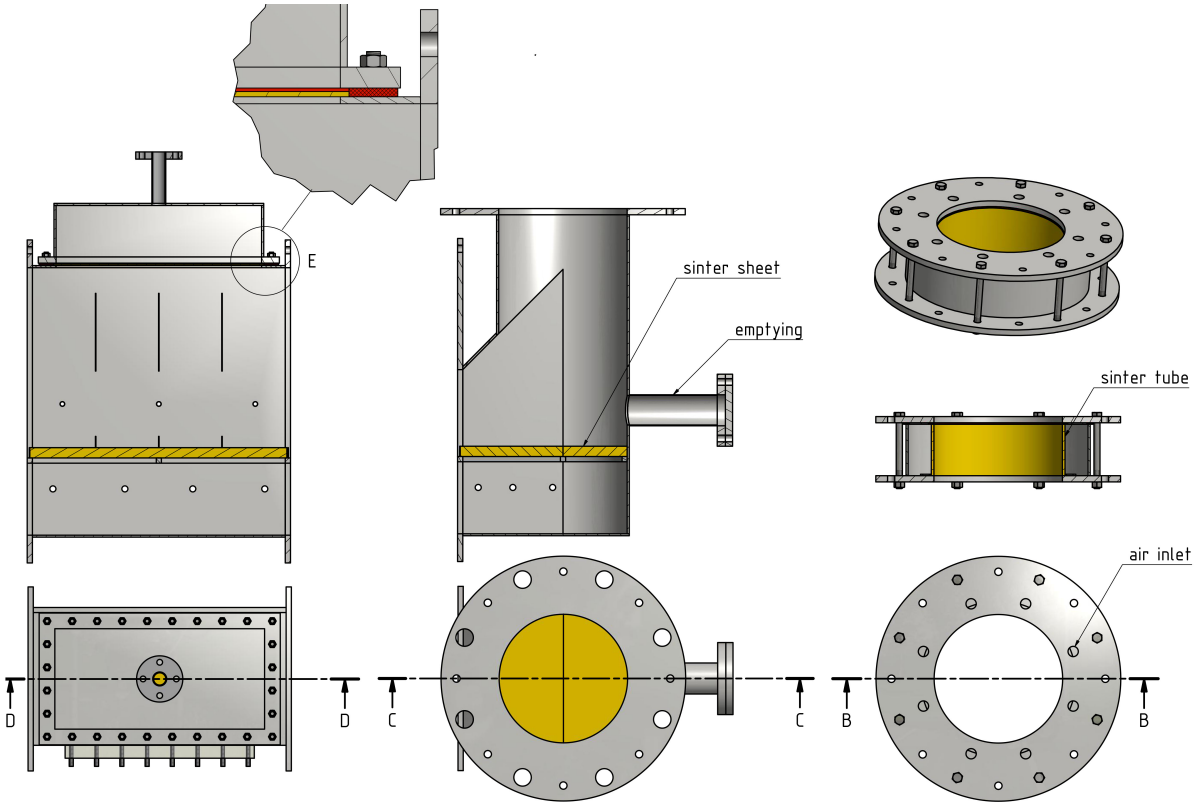

Figure 4.3.: Detailed 3D and sectional views and projections of sintered distributor and filter elements, sintered elements are yellow, seals are red; by V. Sulzgruber

Distributing elements' pressure drops Δp are of course to be calculated with *minimal FG*s, as they are needed to enable homogeneous air flow at any time. The sinter elements' manufacturer and distributor *GKN Sinter Metals* offers the following formula for precise calculation of Δp, [15]:

$$\Delta p = \frac{\dot{V} s}{A} \left(\frac{\mu_a}{\alpha} + \frac{\dot{V} \rho_a}{A \beta} \right) \tag{4.1}$$

where μ_a represents dynamic viscosity and ρ_a the density of applied air. A and s are cross sectional area and thickness of the concerned sintered element in flow direction and α and β are parameters depending on the elements porosity, again given by *GKN*. The particle filters before pressure control valves in air outlet streams were chosen with a porosity of

20 μm, as only about 5 % of applied representative quartz particles are smaller than this (see **figure 2.3**). Apart from that pressure losses were to be kept in check, as they are directly increasing minimum applicable floor pressures and thus decreasing the range of implementable pressures in general. As mentioned above, the maximum utilized pressure (and also the applied blower's maximum pressure) would be limited to 1.5 *bar* in an attempt of avoiding pressure equipment directive. The blower planned for application with the AR is an *AERZEN Delta Blower G5 Type: GM 10 S* with a nominal flow and pressure difference of 810 kg/h respectively 500 *mbar*. A matching data sheet will be found in **appendix ??**.

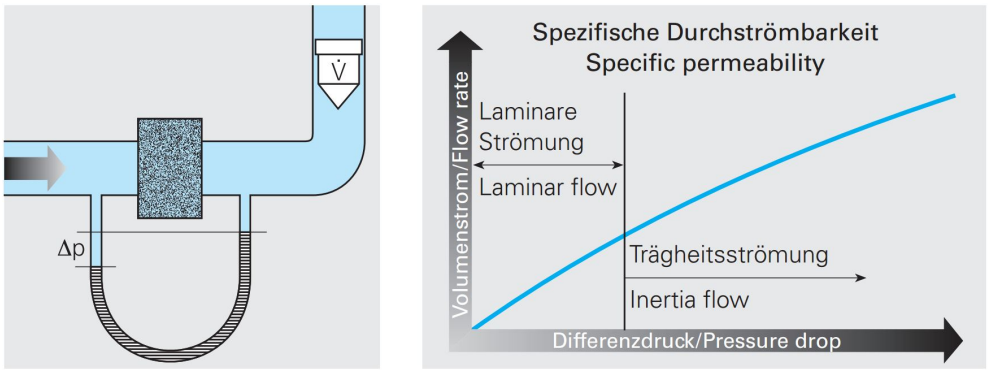

Figure 4.4.: Volume flow $\dot{V}$ in dependence of pressure drop Δp of sintered elements and schematic setup enabling it's determination, as shown by *GKN*, [15]

As mentioned above, a rule of thumb for the necessary pressure loss of a distributor floor is 20 to 40 % of the vertical pressure difference over the fluidized bed's height. But this rule of thumb is just that, nothing more and even so it's applicability for the Advanced Regenerator is somewhat questionable, as this apparatus is different to a common fluidized bed in several aspects (an applied pressure gradient along it's floor and partially horizontal air inlet for example). Thus a second approach enabling a comparison was needed and obviously at this stage of research the only possibility to receive such were again the simulations. Consequentially several simulations incorporating above mentioned quartz sand were scanned for occurring pressure fluctuations across the distributor floors. **Table 4.1** shows a comparison of necessary pressure drops derived from both methods.

Table 4.1.: Necessary pressure losses of distributing elements, as derived from **(a)** rule of thumb and **(b)** scanning of simulations, V. Sulzgruber & D. Wünsch

Element	Δp **(a)**	Δp **(b)**
Riser base fluidization	8416 Pa	4100 Pa
Riser ring fluidization	6546 Pa	5200 Pa
HEX base fluidization	1636 Pa	2500 Pa

4.1.2. Piping and Instrumentation

Thirdly hoses, pipes, sensors and valves had to be considered and arranged in a P&I (*Piping and Instrumentation*) diagram (or P&ID) to realize those boundary conditions regarding flow and pressure so conveniently set in *Barracuda*. If every chamber's fluidization and pressure control was to be realized separately to achieve maximum flexibility in the cold trials, obviously a control valve had to be applied for every such boundary condition. Furthermore all pressure checkpoints depicted in **figure 3.19** had to be realized via absolute pressure sensors and additionally a sensor in every windbox (below distributor floors), below every filter and also directly above every distributor floor had to be applied in order of monitoring the distributing elements pressure drops. $Vfrac$ checkpoints as depicted in **figure 3.19** would have been highly useful for the cold test bench too, but the measuring of $Vfrac$ respectively porosity ψ in a fluidized bed is very challenging in general and would have been far too expensive for this prototype (not to speak of the extreme resolution of checkpoints as depicted in **figure 3.19**).

Air volume flows have to be measured via rotameters before any air in- and after every air outlet valve to monitor fluidization grades and pressure control. With rotameters metering volume flow consequential additional temperature (thermocouples) and pressure checkpoints are necessary before any air in- and after every air outlet valve to obtain the thermodynamic states of measured volume flows, enabling the calculation of mass flows. Finally a bypass (to the environment) before the inlet valves was implemented enabling easy smooth startup operation with already running blower, as to prevent pressure shocks a roughly linear increase of air flow while starting is necessary. It also enables a proportional

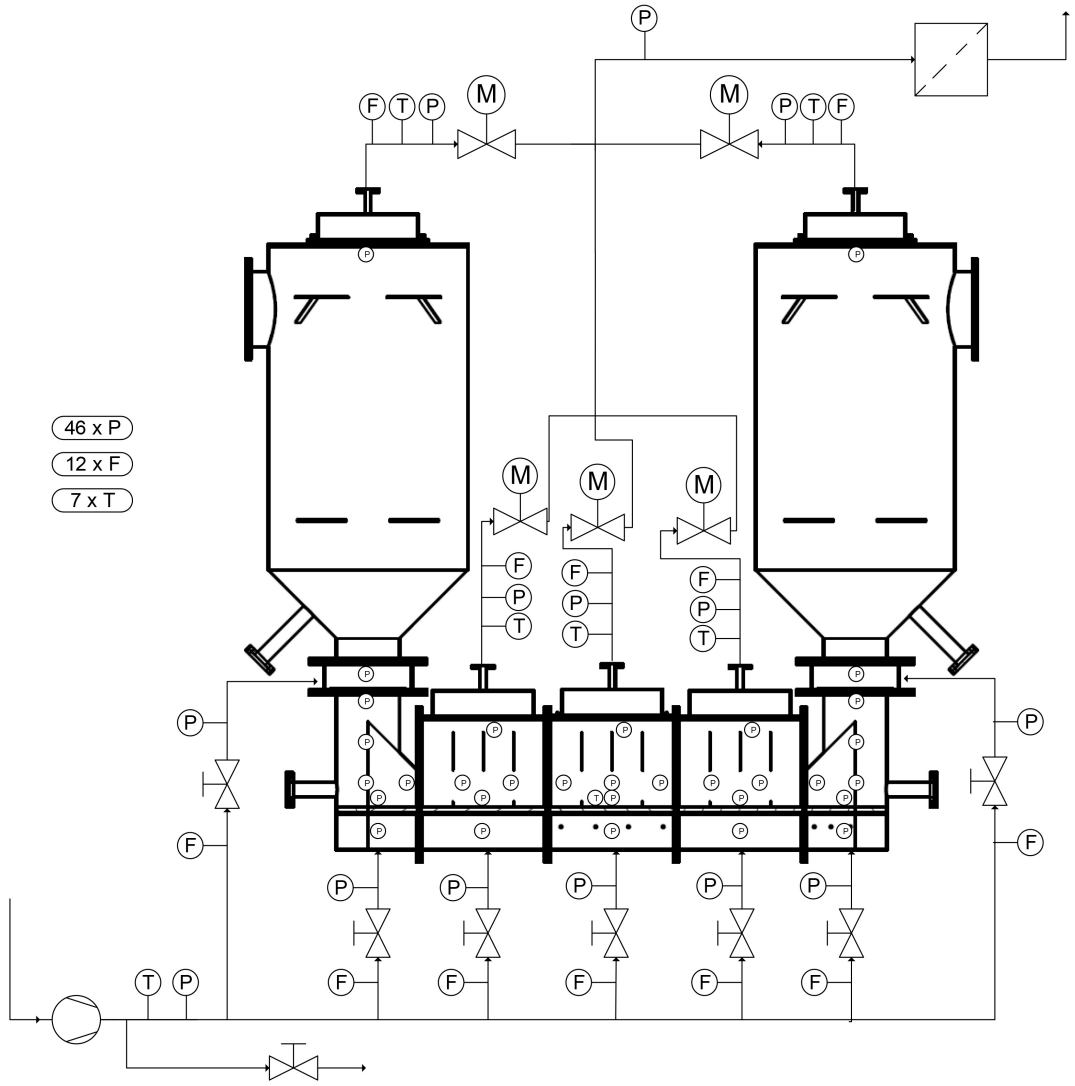

Figure 4.5.: Advanced Regenerator P&I diagram; letters P, F and T represent pressure, flow and temperature checkpoints; V. Sulzgruber and D. Wünsch

overall reduction of FGs if opened during operation. This bypass would not be strictly necessary but it's implementation is rather simple and cheap. The subsequent P&I diagram is depicted in **figure 4.5**.

Another issue regarding measuring instrumentation is the measurement of particle mass flows along the HEX. Measuring particle mass flows is a challenge in general, as precise results would demand very expensive optical methods, which are not worth further consideration, due to their very high price. Unfortunately this leaves only primitive methods focused on gauging hopper levels and potentially precise but highly complicated and susceptible solutions including some kind of weighing of hoppers to deduce transported particle

mass. A method utilizing scales has indeed been applied with another test rig of the *IET* with significant difficulty. Thus a solution including height scales (realized with the help of equidistant steel baffles) arranged opposite to the plexi glass windows included in the upper hoppers is intended. This setup is obviously far from perfect and a more sophisticated, while still inexpensive method would be highly welcome. Hence some further research regarding this topic might be worthwile.

4.1.3. Control Valves

Fourthly the control valves regulating air flow and internal pressure had to be calculated. Valves can generally be defined by giving a K_{vs}-value representing maximum flow and and a control range indicating possible flows lower than the one associated with the K_{vs}-value. For example a control range of 1/10 means any K_v-value in between the K_{vs} (associated with maximum flow at a certain state) and a minimum K_v-value being a tenth of K_{vs} (resembling a tenth of said flow at the same state) can be applied. In the thesis at hand a formula given by *Samson* ([11]) has been applied to calculate K_{vs}-values, as most manufacturers and distributors offer their own versions of this formula and all of those versions do (necessarily) offer similar results:

$$K_v = \frac{\dot{m}_a}{519}\sqrt{\frac{T_1}{p_2\ \rho_{a0}\ \Delta p}} \tag{4.2}$$

with

$K_{vs} = \frac{K_{vmax}}{0.9}$ for actuated valves and

$K_{vs} = \frac{K_{vmax}}{0.75}$ for manual valves and

$$\Delta p = |p_1 - p_2|.$$

The indices 1 and 2 represent states before and after the valve. The index 0 though represents a nominal state at 0 $°C$ and 1.013 bar. Moreover pressures p are to be inserted in bar, the air mass flow $\dot{m}_a$ in kg/h, the temperature T in K and the density ρ in kg/m^3.

Obviously, to find necessary K_{vs}- and minimum K_v-values, minimum and maximum values for both pressures and mass flows would have to be considered. The possible mass flows are relatively easy to deduce from nominal point FGs and desired variations from this point including a margin for unpredicted variations (while trying to keep the spread between minimum K_v and K_{vs} both reasonable and affordable, meaning roughly between 10 and 100 % of K_{vs}). An enhanced margin (-10 % respectively $+10$ %) in $\dot{m}_a$ for unpredicted variations due to air flows possibly partly bypassing pressure barriers (sand level above upper baffles) was set for the pressure control valves. Later on ordered valves would of course enable larger variations, as they would have to offer at least given K_{vs}- and minimum K_v-values and those would not likely be met precisely. The deduced mass flows and needed variations from the nominal point are shown with **table 4.2**.

Table 4.2.: Range of the control valves' desired air mass flows, derived from nominal point FGs and desired variations

Valve Position	Minimum FG	Nominal FG	Maximum FG	Min. $\dot{m}_a$	Nom. $\dot{m}_a$	Max. $\dot{m}_a$
Riser base, fluid.	60 % $\equiv$ 6.6	11	120 % $\equiv$ 13.2	3.42 g/s	5.71 g/s	6.84 g/s
Riser ring, fluid.	50 % $\equiv$ 6.5	13	120 % $\equiv$ 15.6	4.75 g/s	9.52 g/s	11.40 g/s
Riser top, p contr.	-10 %	-	$+10$ %	7.35 g/s	15.23 g/s	20.06 g/s
HEX base, fluid.	71 % $\equiv$ 5	7	120 % $\equiv$ 8.4	5.82 g/s	8.20 g/s	9.84 g/s
HEX top, p contr.	-10 %	-	$+10$ %	5.24 g/s	8.20 g/s	10.82 g/s

To find minimum and maximum values for AR valve pressures there are to be separated two principal cases regarding valves. As can be seen in **figure 4.5** there are seven (manually controlled) valves meant for fluidization respectively air feed into the AR and five (actuated) valves meant for pressure control respectively controlled air discharge. Thus those seven valves do have a constant pressure before the valve and those five after, meaning the pressure *after* the inlet valves (index i) is equal to the pressure *before* the outlet valves (index o) plus the vertical pressure loss of the bed, sintered floor and filter disk. If the bed's pressure loss is approximately (because *total* emptying of the HEX is quite impossible during operation, though the error is small) set to zero the limits of pressure are known. That is because for the inlet valves p_{i1} is constant and equal to ambient pressure p_a plus blower pressure increase p_b ($p_{i1} = p_a + \Delta p_b$) and for the outlet valves p_{o2} is constant and equal to p_a plus the pressure

loss Δp_{out} in tubes and a fine particle filter after those valves ($p_{o2} = p_a + \Delta p_{out}$). Furthermore to render K_{vs} finite (and the spread from minimum K_v to K_{vs} reasonable) a minimum Δp referred to as Δp_{min} had to be set and it was chosen to be $\Delta p_{min} = 0.03\ bar$. Now taking into account all that has been said, for the outlet valves there has to be $p_{o1min} = p_{o2} + \Delta p_{min}$ and consequentially for the inlet valves $p_{i2max} = p_{i1} - \Delta p_{min}$ and finally with approximately zero bed pressure loss one gets $p_{o1max} = p_{i2max} - \Delta p_s$ and $p_{i2min} = p_{o2min} + \Delta p_s$ with the generalized sintered element (distributor floor and filter disk) pressure loss Δp_s.

Table 4.3.: Minimum and maximum occurring valve air flows $\dot{m}_a$ and pressures p with resulting K_{vs}- and minimum K_v-values

Valve Position	Min. $\dot{m}_a$	Max. $\dot{m}_a$	T_a	p_{1min}	p_{1max}	p_{2min}	p_{2max}	K_{vmin}	K_{vs}
Riser base, fluid.	3.42 g/s	6.84 g/s	60 $°C$	1.51 bar	1.51 bar	1.10 bar	1.48 bar	0.57	4.83
Riser ring, fluid.	4.75 g/s	11.40 g/s	60 $°C$	1.51 bar	1.51 bar	1.08 bar	1.48 bar	0.78	8.04
Riser top, p contr.	7.35 g/s	20.06 g/s	60 $°C$	1.05 bar	1.42 bar	1.02 bar	1.02 bar	1.22	14.2
HEX base, fluid.	5.82 g/s	9.84 g/s	60 $°C$	1.51 bar	1.51 bar	1.08 bar	1.48 bar	0.95	6.94
HEX top, p contr.	5.24 g/s	10.82 g/s	60 $°C$	1.05 bar	1.42 bar	1.02 bar	1.02 bar	0.86	7.68

The results of those considerations and calculations are shown with **table 4.3** for an exemplary particle and blower outlet temperature of 60 $°C$. Although blower outlet temperature might well reach about 90 $°C$ on a hot summer's day, the resulting variation in K_{vs} is almost negligible concerning the cold test rig (about 5 % per 40 $°C$). Furthermore it should be considered to buy control valves with an especially large range of possible K_v-values respectively control ranges (like 5 or even 2 to 100 % K_{vs} respectively 1/20 or even 1/50), as it would be very reasonable to try for maximum flexibility regarding a range of powders possible to be fluidized with the AR cold testing bay. Because K_v is linearly dependent on $\dot{m}_p$ which is linearly dependent on u_{mf} (if temperatures and pressures are set constant, which can be done with little error regarding cold bench tests) minimum K_v-values stated above should be reduced by a percentage calculated from u_{mf} ratios. Considering $u_{mfAl2O3} \approx 5.3\ mm/s$ (with $\rho_{Al2O3} = 3965\ kg/m^3$ and $d_{pmAl2O3} = 60\ \mu m$, placing the corundum powder on the border line between groups A and B in the Geldart diagram, see **figure 2.2**) and $u_{mfSiO2} \approx 7\ mm/s$ for example, a ratio of $u_{mfAl2O3}/u_{mfSiO2} \approx 0.76$ is obtained, which means minimal K_v-values shown below would have to be reduced by ≈ 24 % respectively multiplied by 0.76 to enable corundum to be fluidized with the AR. Another example would

be a very interesting phase change material (PCM) with $u_{mfPCM} \approx 2.5\ mm/s$, though it would need minimum K_v-values to be reduced by ≈ 64 %, which is a lot. Obviously this method will also apply for powders with higher u_{mf} by multiplying below shown K_{vs}-*values* with an obtained u_{mf} ratio.

4.1.4. Process Layout

Fifthly and finally a performance calculation was done to gauge overall process parameters like total AR powder volume and mass, dead volume ratio (HEX and lower risers), maximum and minimum duration of transport, theoretically storable heat and theoretical thermal power, utilizing known geometry, powder properties and experimental values for particle mass fluxes Φ_p obtained from the simulations.

The maximum utilizable hopper volume is $V_{hopper} \approx 0.6\ m^3$ (for one hopper being full or two hoppers half full) and a reasonable total HEX volume (including lower risers) would be $V_{HEX} \approx 0.09\ m^3$. Reasonable in this context means the HEX is filled to a level above the upper baffles' lower edges and below those baffles' upper edges, as an actually full HEX would obviously be useless in terms of transportation and even problematic in terms of potentially clogging filters. Above stated volumes yield a dead volume percentage of about 13 %. With the densities of utilized powders being stable and constant to very high temperatures, this consideration does also fit mass % and the derived masses for quartz sand (with a density of $\rho_{SiO2} = 2650\ kg/m^3$ and a bulk porosity of 53 %) are $m_{hopper} \approx 750\ kg$ and $m_{HEX} \approx 110\ kg$. For corundum powder (with a density of $\rho_{SiO2} = 3965\ kg/m^3$ and a bulk porosity of 45 %) the masses are $m_{hopper} \approx 1300\ kg$ and $m_{HEX} \approx 200\ kg$.

To calculate theoretically storable heat, thermal power and also minimum and maximum duration of transport systems utilizing quartz or corundum had obviously to be treated separately. With corundum powder minimum respectively maximum mass fluxes of $\Phi_p \approx 40\ kg/m^2s$ and $\Phi_p \approx 300\ kg/m^2s$ were achieved in *Barracuda*. If those are applied on the HEX's cross section of 250 mm x 130 mm with a tube bundle (as will be utilized for heat transfer estimations below) blocking 33 % of that area mass flows of $\dot{m}_p \approx 0.9\ kg/s$ respectiveley $\dot{m}_p \approx 6.5\ kg/s$ are obtained. With those mass flow rates a minimum and

maximum duration of transport can be calculated ($t = m_{hopper}/\dot{m}_p$). Those are $t_{min} \approx 3.3\ min$ and $t_{max} \approx 25\ min$. As the hot test bench and prototypes are planned and calculated for hot and cold hopper temperatures of $T_h = 850\ °C$ and $T_c = 650\ °C$ producing a temperature difference of $\Delta T = 200\ K$, a theoretical maximum heat stored ($Q_{stored} = m_{hopper} c_p \Delta T$) and theoretical thermal powers of the HEX ($P_{th} = \dot{m}_p c_p \Delta T$) can be deduced for both the cold and the hot test rig. The heat capacity is derived from a polynomial yielding a mean value of $c_{pm} \approx 1230\ J/kgK$ in the temperature range of interest. The maximum heat to be stored utilizing corundum thus calculates to $Q_{stored} \approx 90kWh$ and the minimum and maximum thermal power are $P_{th-min} \approx 212\ kW$ and $P_{th-max} \approx 1.6\ MW$.

Utilizing quartz sand on the other hand, minimum respectively maximum mass fluxes of $\Phi_p \approx 23\ kg/m^2s$ and $\Phi_p \approx 170\ kg/m^2s$ were derived from values observed with corundum. Applied on the HEX's cross section of 250 mm x 130 mm again with a tube bundle blocking 33 % of the area mass flows of $\dot{m}_p \approx 0.5\ kg/s$ respectiveley $\dot{m}_p \approx 3.8\ kg/s$ are calculated. The minimum and maximum duration of transport calculate to $t_{min} \approx 3.3\ min$ and $t_{max} \approx 25\ min$. Maximum heat stored and thermal powers of the HEX are $Q_{stored} \approx 48kWh$ and $P_{th-min} \approx 116\ kW$ respectively $P_{th-max} \approx 870\ kW$. The most important results presented above are also shown in **table 4.4**.

Table 4.4.: Process calculation results for the cold test rig

Powder	m_{hopper}	m_{HEX}	$\dot{m}_{min}$	$\dot{m}_{max}$	t_{max}	t_{min}	P_{th-min}	P_{th-max}	Q_{stored}
Corundum	1300 kg	200 kg	0.9 kg/s	6.5 kg/s	25 min	3.3 min	212 kW	1.6 MW	90 kWh
Quartz	750 kg	110 kg	0.5 kg/s	3.8 kg/s	25 min	3.3 min	116 kW	870 kW	48 kWh

A thermal power range of $P_{th-min}/P_{th-max} \approx 13$ % to 100 % can be deduced. Moreover some thought has to be put on the heat transfer in an AR HEX, as above mentioned high thermal powers will have to be matched by cooling respectively heating power of a fluid flowing in the HEX's tube bundle or resistive heating rods in the rather limited HEX cross section of 250 mm x 130 mm. Further calculations and estimations will be necessary to show if such is possible or a longer HEX has to be applied. Some considerations regarding those are to be found with the hot test rig's layout in **section 4.2.3**. The *Mathcad* calculations underlying above stated values can be found in **appendix A**.

And last but not least an auxiliary power consumption for the AR is gauged by calculating the isentropic (and adiabatic) power consumption of a compression of an ideal gas, as the compressor power needed for fluidization represents the major part regarding auxiliary power, barring electric power consumption of the valve actuators, which is expected to be very low. This isentropic power is the reversible equivalent of the power consumed by the *Aerzen* blower and dependent on the air's heat capacity $c_{pm.a} \approx 1006\ J/kgK$, the ambient temperature T_1, the pressure ratio $\pi = p_2/p_1$, the isentropic exponent κ and of course the air mass flow $\dot{m}_a$:

$$P_s = \dot{m}_a c_{pm.a} T_1 \left(\left(\frac{p_2}{p_1} \right)^{\frac{\kappa-1}{\kappa}} - 1 \right) \tag{4.3}$$

To calculate isentropic power consumption during start-up a maximum air mass flow in the risers and hoppers will be applied ($\dot{m}_{a.start} \approx 36.5\ g/s$, HEX is not fluidized) together with the maximum available pressure ratio $\pi_{max} = 1.5\ bar/1\ bar = 1.5$ and an ambient temperature of $T_1 = 25\ °C = 298.15\ K$. The isentropic auxiliary compressor power during start-up thus calculates to $P_{s.start} \approx 1344\ W$. For nominal operation obviously the nominal air mass flow was applied. Summarizing values presented in **section 4.1.3** this mass flow is $\dot{m}_{a.nom} \approx 55.1\ g/s$. The associated nominal pressure ratio is $\pi_{nom} \approx 1.33\ bar/1\ bar = 1.33$, while the ambient temperature stays the same and an isentropic nominal compressor power of $P_{s.nom} \approx 1400\ W$ is derived. Both are conveniently low, which is an essential advantage of the AR concept and will be even lower at actual operating temperatures, as needed fluidization air to realize the same state of fluidization decreases with rising process temperature and dynamic air viscosity μ_a respectively falling u_{mf} and ρ_a (see also **section 4.2.1**).

4.2. Hot Test Rig

A detailed layout of the hot AR test bench will be performed only after basic cold bench tests have been run and at least most critical results concerning e.g. minimum applicable particle mass flows, transport into and out of hoppers utilizing quartz sand, validation of

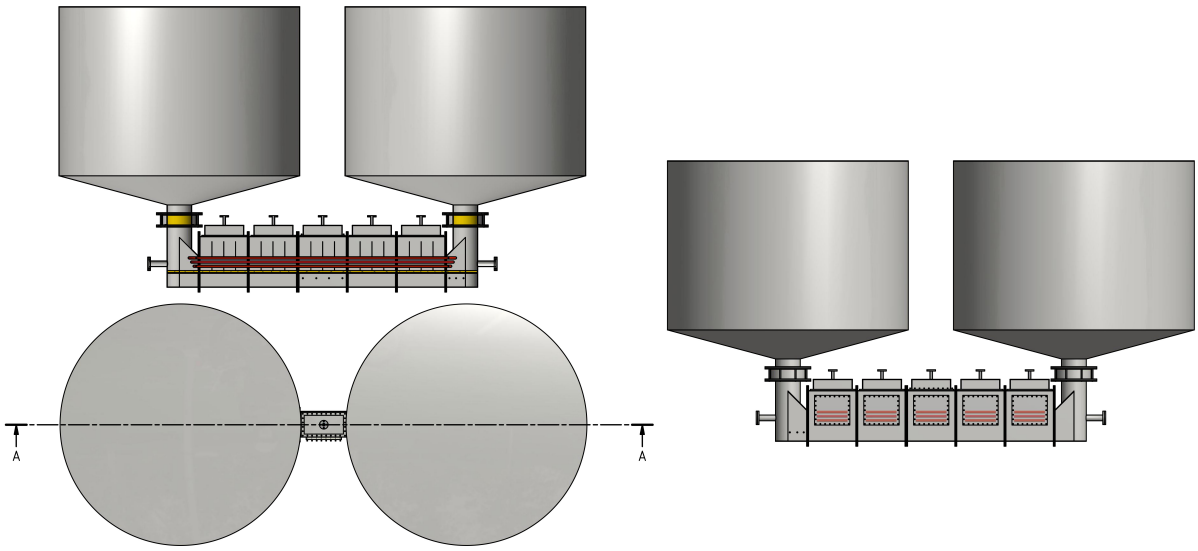

Figure 4.6.: Frontal sectional view and frontal and horizontal projections of the Advanced Regenerator hot test bench, sintered elements are yellow, exemplary tube bundle is red; by V. Sulzgruber

pressure control or transport in a HEX equipped with a tube bundle are obtained. Until then only the most critical components and performance calculations regarding the hot test rig, that were decided potential financial or performance bottlenecks will be addressed. This was decided due to the fact that process factors and results achieved with the cold test bench are meant to be utilized for the hot bench's final layout, as has been mentioned above.

The AR hot test bench does to this point only exist as a rough sketch. **Figure 4.6** depicts the AR hot test rig in a frontal sectional view and frontal and horizontal projections. Again a modular construction is applied to enable high flexibility. Obviously the test rig is shown without it's thermal insulation to enable a better overview. The biggest evident differences to the cold test rig are the very large hoppers and a longer HEX, consisting of at least 5 segments (compared to 3 with the cold test bench). The hoppers' size was so drastically increased to enable long transport durations and test realistic storage durations (of 8 h plus) and associated heat losses. The HEX will have to include an actual functional tube bundle (or even the option for several bundle geometries) to test heat exchange with various heat transfer media. Moreover a construction to enable the application of resistive heating elements will have to be designed to test electric heating of applied powders. The hoppers'

internal height from the distributor floor to the top is again set to roughly 2.5 m to be able to validate (or refute) even failed simulations. Hopper diameter is 2500 mm, the HEX segments are roughly 500 mm long, 630 mm high and 250 mm deep with a channel cross section of about 250 mm x 130 mm (in between baffles), resulting in an insulated footstep of about 6500 mm x 3500 mm.

The hot P&I diagram is quite similar to the cold one (see **section 4.1.2**) with the exception of additional heat exchangers, transferring the waste heat from air leaving the AR with air entering the AR, so called recuperators. Those are to be further addressed in context with the hot gas valves in **section 4.2.1**. Sintered elements will be almost identical to those shown with the cold test rig (see **section 4.1.1**), barring any grave insights, that might be obtained from cold bench tests. Resistive heating Rods for the hot rig were estimated to be proven technology, as they are available in many variations for reasonable prices. Especially promising assortments were found with the manufacturers *Kanthal* (see their heating wires with very flexible applicability) and *Watlow* (they have elements enabling various temperatures along the rods). Unfortunately both did not react to my inquiries regarding possible heating solutions for the AR to this point.

The hot gas valves on the other hand are definitely decided to be a potential (economical) bottle-neck and will be addressed below. Another additional component is the thermal insulation. As it is expected to play a critical role for the AR's overall feasibility, it will also be considered below. Finally another procedural layout will be presented to gauge overall process parameters of a hot AR prototype.

4.2.1. Control Valves

The hot test rig will have to enable stable fluidization not only at operating temperatures but also while starting up cold. This means an even wider range of air mass flows have to be controlled and especially small flows at the maximum temperature as hot nominal $u_{mf} \approx 4\ mm/s$ is lower compared to nominal $u_{mf} \approx 7\ mm/s$ at 60 $°C$ (mostly due to higher μ_a) with air densities being also significantly lower at elevated temperatures. Those mass flows and temperatures are shown with **table 4.5** for an exemplary riser base

fluidization control valve, as minimum K_{vs}-values will occur with that valve and those are most problematic because the lower K_{vs}-values, that will be needed are already aproaching the purchasable minimum for this temperature range. An actual layout calculation for all valves will be performed, when cold trials are running and results regarding fluidization grades and to be applied powders can be deduced.

Table 4.5.: Range of the riser base's control valve's desired air mass flows, derived from nominal point FGs and desired variations

Valve Position	Minimum FG	Nom. FG	Maximum FG	Min. T	Nom. T	Max. T	Min. $\dot{m}_a$	Nom. $\dot{m}_a$	Max. $\dot{m}_a$
Riser base, fluid.	60 % ≡ 6.6	11	120 % ≡ 13.2	60 °C	750 °C	850 °C	0.672 g/s	1.45 g/s	11.1 g/s

Indeed control valves that are able to precisely adjust very low mass flows between 60 °C and (estimated) 550 °C for fluidization valves respectively 850 °C for pressure control valves represent high tech equipment and are very expensive. Additionally a large control range of roughly 1/20 is needed if only quartz sand is to be fluidized. K_{vs}-values again obtained exemplarily for riser base's control valves are presented with **table 4.6**.

Table 4.6.: Minimum and maximum applied air flows $\dot{m}_a$ and pressures with resulting K_{vs}- and minimum K_v-values for for riser base's control valves

Valve Position	Min. $\dot{m}_a$	Max. $\dot{m}_a$	p_{1min}	p_{1max}	p_{2min}	p_{2max}	K_{vmin}	K_{vs}
Riser base, fluid.	3.42 g/s	6.84 g/s	1.51 bar	1.51 bar	1.10 bar	1.48 bar	0.57	4.83

There were found only two suppliers offering valves enabling stated mass flows and control range for the desired temperature span, namely *Ringo* and *Cera Valve*, both daughters of the *Samson Group*. *Ringo* was quickly eliminated because their valves were currently not built small enough and the only price that was received from them were 24500 *Euro* for one such valve. *Cera Valve* on the other hand has the additional benefit of ceramic fittings for their ball valves offering advanced wear resistance in combination with small particles (as particles with $d_p \leq 20\ \mu m$ might pass sintered filter sheets) and genuine thermal shock resistance ($\leq 450\ K$ with SiC and $\leq 550\ K\ Si_3N_4$). Their most expensive valve in $X-HT$ version (type $KAL\text{-}HT$ DN 15-15-15) would enable a maximum temperature of 950 °C, but

even this valve would need a special profile ceramic ball to enable precise control of minimum $\dot{m}_a$. The casing is manufactured of $1.4876H$ steel. Unfortunately such a valve would cost roughly 11000 *Euro* (including a motor-actuator), a price that might still endanger the whole AR project's feasibility, as a minimum of 3 such valves would be needed (and a maximum of more than 5, if HEX segments were to be controlled separately).

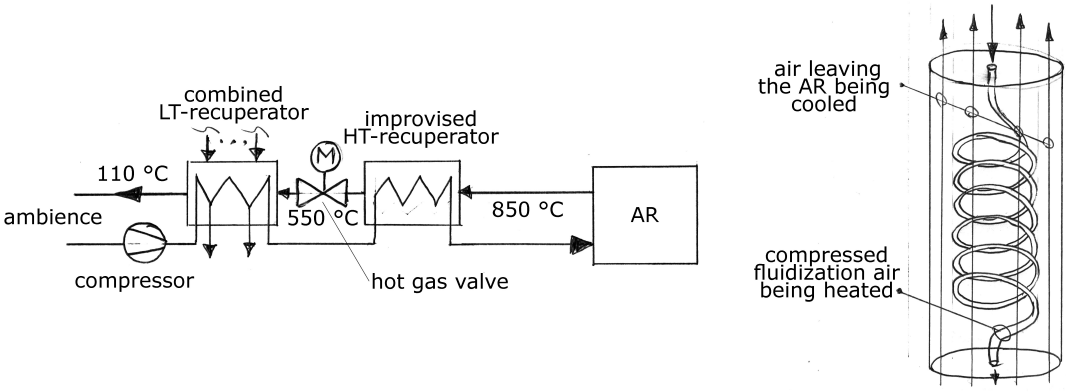

Figure 4.7.: Schematic depiction of an excerpt P&ID and an improvised recuperator, enabling cooling of air *before* outlet valves; HT ... high temperature, LT ... low temperature

Thus other ways to reduce the hot gas valves' prices should be taken in account. For example a recuperation of hot air *before* pressure control valves could cool down the gas temperature below 550 $°C$. **Figure 4.7** depicts such a setup with two stage recuperation and a schematic sketch of an improvised low cost recuperator. There would be needed a minimum of 3 (or more than five ...) such small HT-recuperators (or a bank with combined to be heated but separated to be cooled streams) and the savings generated from lower gas temperatures in the valves would obviously only provide a gain in feasibility if those recuperators are sufficiently inexpensive. Moreover fluidization air has to be compressed before heating as the exergy demand of a cold compression is significantly lower. The combined LT-recuperator would then exchange the remaining heat in the hot air stream leaving pressure control valves with the compressed air for fluidization and thus further improve the exergy balance.

Generated savings (with 550 $°C$ max. valve T) would be at least $2000-2500$ *Euro* per valve due to cheaper steel and another 1200 *Euro* applying a less expensive ceramic material too (ZrO_2 instead of SiC, thermal shock resistance $\leq 250\ K$). Those measures yield overall

savings of roughly 3500 *Euro* respectively a price of roughly 7500 *Euro* per valve. This problem will have to be addressed in more detail with the final hot bench constructional layout (after performing cold bench tests).

4.2.2. Thermal Insulation

As the maximum (and even minimum) design bed temperatures applied in this work are rather high (max. temperature $T_h = 850\ °C$), thermal insulation is another critical parameter regarding the hot test rig's layout and is thus considered in detail in the following. If, in a simple approach, the hot storage hopper's steel cylinder's outward temperature is set to $T_h = 850\ °C$ (the error is roughly 2 K), the outside insulation surface temperature is set to $T_W = 60\ °C$ and an ambient temperature of $T_a = 20\ °C$ is assumed, a minimum zylindrical insulation layer thickness of $s_{cyl} \approx 474\ mm$ is derived (see **appendix A.3** for the *Mathcad* calculation and the *VDI Heat Atlas* [16]). This layer consists of an outer layer of minimum 321 *mm ProRox WM 960* rock wool and a more expensive inner layer of minimum 153 *mm RHI Pyrostop L23* fibre blankets. Associated high temperature hopper heat losses are $\dot{Q}_{loss} \approx 6200\ W$ which resembles a specific loss of $\dot{q}_{loss} \approx 161\ W/m^2$. Stated brand materials are just examples, as they are rather common products. For the bottom and cover of the hopper, utilizing the same materials, minimum outer and inner layers of 361 *mm* respectively 202 *mm* (overall 563 *mm*) have to be applied to achieve the same temperatures as stated above. Consequentially, as the insulated temperature difference is very high ($\approx 790\ K$), a large bulk of insulation material will be needed, though it has to be kept in mind, that in between hoppers a thinner layer of high temperature insulation materials (like *RHI Pyrostop L23*) only will be needed, as the temperature difference between hoppers is $850\ °C - 650\ °C = 200\ K$.

Nevertheless, this approach might be too simple, because considering the actual transient heat conduction process it should be taken in to account that the outer layers of the cylindrical bulk hopper fill itself will represent additional layers of insulation, as soon as the hopper's steel wall's temperature (and subsequently the outer bulk's temperature) falls below the temperature of its core. This is due to the fact the heat conductivity λ_{bed} of the bulk

itself is expected to be rather low, as it forms a porous medium consisting of greater than 50 % air ($\lambda_{SiO2-850°C} = 3.771\ W/mK$ and $\lambda_{air-850°C} = 0.07477\ W/mK$). The only problem regarding this assumption is to find a λ_{bed}-value for this additional layer of insulation.

The prediction of thermal conductivities of packed beds has been a topic of intensive research for more than one century. A genuine examination of methods that can be applied is again found with the *VDI Heat Atlas* [16]. Apparently primary parameters regarding λ_{bed} have to be the bed's porosity ψ, the conductivity of the particles λ_p and the conductivity of the fluid in between the particles λ_f. There are three basic types of approaches regarding this problem:

- *Type I* is to directly solve the *Laplace* equation for heat conduction for the bed's conductivities and geometry, which is obviously extremely complex and will have to involve numerical methods in most cases.
- *Type II* introduces thermal resistances in both phases and tries to combine them in a way that would represent wanted correlations (Ohmic analogs), for example series or parallel arrangements of phases.
- *Type III* methods calculate the thermal conductivity of a unit cell, which is decided representative for the whole bed. This can be seen as a compromise between the other two types and will yield sufficiently precise results at reasonable expenses.

It seems a Type III method will be needed to approach the problem at hand. One such method of this kind is the model of Zehner, Bauer and Schlünder, which introduces a unit cell consisting of a cylindrical core containing solid particles and a fluid-filled section around that core. It's most basic version will be introduced in the following, as it is decided sufficiently precise for *mostly spherical* particles in a *packed* bed, like those to be found in the AR's hoppers and will not go beyond the scope of this work. Nevertheless a more detailed examination of the topic including all the more complex variations of this model and possibly also others to compare obtained results is recommended.

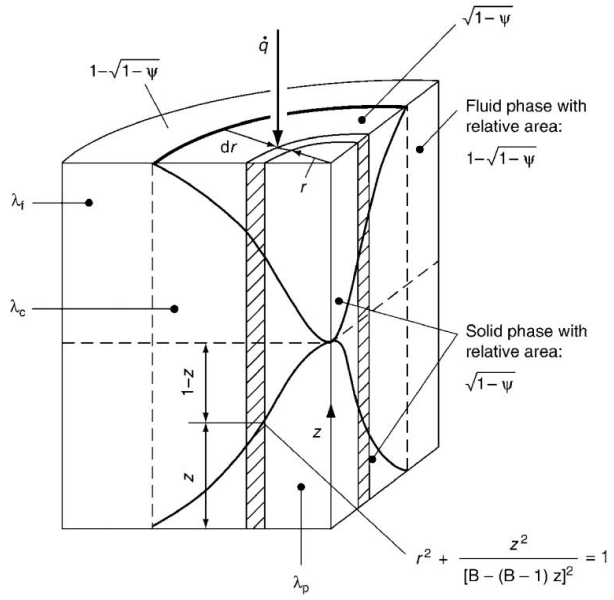

Figure 4.8.: Unit cell of the model of Zehner, Bauer and Schlünder, *Type III* method, [16]

The basic model of Zehner, Bauer and Schlünder includes the following equations:

$$k_{bed} = \frac{\lambda_{bed}}{\lambda_f} = 1 - \sqrt{1-\psi}\,(1+k_c) \tag{4.4}$$

$k_c = \lambda_c/\lambda_f$, where λ_c is the thermal conductivity of the unit cells core and can be calculated:

$$k_c = \frac{2}{N}\left(\frac{B}{N^2}\frac{k_p-1}{k_p}\,ln\frac{k_p}{B} - \frac{B+1}{2} - \frac{B-1}{N}\right) \tag{4.5}$$

$$N = 1 - \frac{B}{k_p},\ k_p = \frac{\lambda_p}{\lambda_f} \tag{4.6}$$

B is a deformation parameter and for spherical particles:

$$B \approx 1.25\left(\frac{1-\psi}{\psi}\right)^{10/9} \tag{4.7}$$

If those equations are evaluated for both quartz sand and corundum powder the biggest (or even only grave) disadvantage regarding the utilization of corundum powders with the AR to this point is revealed. Obtained conductivities for SiO_2 are $\lambda_{bedSiO2.850°C} = 0.352\,W/mK$

and $\lambda_{bedSiO2.650°C} = 0.285\ W/mK$, while the conductivities of Al_2O_3 are $\lambda_{bedAl2O3.850°C} = 0.663\ W/mK$ and $\lambda_{bedAl2O3.650°C} = 0.513\ W/mK$.

Apparently the thermal conductivity of a packed bed composed of corundum powder is almost twice the value of a conductivity of a bed of quartz sand, in the temperature range of interest, which is especially interesting as corundum's thermal conductivities are thrice the values of quartz and more. This might substantially benefit quartz sand as a storage medium for longer storage durations, although further examinations regarding actual transient hopper temperature profiles (preferably in cylinder coordinates) and resulting conductivities and heat losses over time will be necessary. **Nevertheless the quartz sand bed's thermal conductivities are roughly only twice as high as conductivities of a common insulation material at the same temperatures, which means that the bed is half as good an insulation as the insulation itself, as conduction is linearly dependant on λ. This is a very promising result.**

Further considerations and calculations regarding actual transient hopper temperature profiles (preferably in cylinder coordinates) and resulting heat losses over time should be performed. This should be achieved via a transient solution of the Laplace equation for a cylinder utilizing λ_{bed}-values obtained with the model of *Zehner*, *Bauer* and *Schlünder*.

4.2.3. Process Layout

Finally another procedural calculation was performed to gauge overall process parameters for the AR hot test bench, though several calculated values will match those from above, as the same HEX segment geometry is applied (with two more segments compared to the cold test rig). Maximum utilizable hopper volume is a lot larger though $V_{hopper} \approx 9\ m^3$ (again for one hopper being full or two hoppers half full) and a reasonable total HEX volume (including lower risers) would be $V_{HEX} \approx 0.13\ m^3$ (the HEX is filled to a level above the upper baffles' lower edges and below those baffles' upper edges). Above stated volumes yield a dead volume percentage of about 1.5 % this time, which is rather good. Again, this consideration does also fit mass % and the derived masses for quartz sand (with a density of $\rho_{SiO2} = 2650\ kg/m^3$ and a bulk porosity of 53 %) are $m_{hopper} \approx 10.1\ ton$ and

$m_{HEX} \approx 160\ kg$. For corundum powder (with a density of $\rho_{SiO2} = 3965\ kg/m^3$ and a bulk porosity of 45 %) the masses are $m_{hopper} \approx 17.7\ ton$ and $m_{HEX} \approx 280\ kg$. The hot test bench is planned and calculated for hot and cold hopper temperatures of $T_h = 850\ °C$ and $T_c = 650\ °C$ producing a temperature difference of $\Delta T = 200\ K$. Those temperatures are rather high to enable high efficiencies (about 30 %) with state-of-the-art Stirling engines (e.g. produced by the Austrian manufacturer *Frauscher Thermal Motors*) for (P2)H2P applications.

Again taking in account minimum respectively maximum mass fluxes of $\Phi_p \approx 40\ kg/m^2s$ and $\Phi_p \approx 300\ kg/m^2s$ achieved with corundum powder, area mass flows of $\dot{m}_p \approx 0.9\ kg/s$ respectiveley $\dot{m}_p \approx 6.5\ kg/s$ are obtained. Minimum and maximum duration of transport are $t_{min} \approx 50\ min$ and $t_{max} \approx 5.5\ h$. The desired hot and cold storage temperatures (of 850 $°C$ respectively 650 $°C$) are high to achieve high efficiencies (about 30 %) with state-of-the-art Stirling engines (e.g. produced by the Austrian manufacturer *Frauscher Thermal Motors*) for (P2)H2P applications. Mean heat capacity is $c_{pm} \approx 1230\ J/kgK$ in the temperature range of interest. The maximum heat to be stored utilizing corundum thus calculates to $Q_{stored} \approx 1.3\ MWh$ and the minimum and maximum thermal powers are $P_{th-min} \approx 212\ kW$ and $P_{th-max} \approx 1.6\ MW$.

Utilizing quartz sand on the other hand, minimum respectively maximum mass fluxes of $\Phi_p \approx 23\ kg/m^2s$ and $\Phi_p \approx 170\ kg/m^2s$ were derived from values observed with corundum. Applied on the HEX's cross section of 250 mm x 130 mm again with a tube bundle blocking 33 % of the area mass flows of $\dot{m}_p \approx 0.5\ kg/s$ respectiveley $\dot{m}_p \approx 3.8\ kg/s$ are calculated. Mean heat capacity is $c_{pm} \approx 1150\ J/kgK$ in the temperature range of interest. The minimum and maximum duration of transport calculate to $t_{min} \approx 50\ min$ and $t_{max} \approx 5.5\ h$. Maximum heat stored and thermal powers of the HEX are $Q_{stored} \approx 650\ kWh$ and $P_{th-min} \approx 116\ kW$ respectively $P_{th-max} \approx 870\ kW$. The most important results presented above are also shown in **table 4.7**.

With above stated very high thermal powers P_{th} and consequent power densities of the AR's HEX one has to ponder a reduction of it's scale as many decentralized AR applications, for example as a pure heat storage in energy intensive industries or as a thermal battery (P2H2P) with a Stirling, would utilize lower powers. A Stirling engine of *Frauscher Thermal*

Table 4.7.: Process calculation results for the hot test rig

Powder	m_{hopper}	m_{HEX}	$\dot{m}_{min}$	$\dot{m}_{max}$	t_{max}	t_{min}	P_{th-min}	P_{th-max}	Q_{stored}
Corundum	17.7 ton	280 kg	0.9 kg/s	6.5 kg/s	5.5 h	50 min	212 kW	1.6 MW	1.3 MWh
Quartz	10.1 ton	160 kg	0.5 kg/s	3.8 kg/s	5.5 h	50 min	116 kW	870 kW	650 kWh

Motors e.g. could absorb a thermal power of roughly 15 to 25 kW per unit. Of course if needed tube bundle (and thus HEX) length for cooling/heating is met the HEX cross section can be reduced to a certain degree, hence reducing overall power and shifting the range of power ($P_{th-min}/P_{th-max} \approx 13$ %) to more feasible areas. Nevertheless further simulations and bench tests should inter alia focus on a validation of the possibility of lower mass fluxes and flows with the AR. *Mathcad* calculations underlying above stated values can be found in **appendix A.1**.

As announced above, some thought has to be put on the heat transfer in an AR HEX, as above mentioned high thermal powers will have to be matched by cooling respectively heating power of a fluid flowing in the HEX's tube bundle or resistive heating rods in the rather limited HEX cross section of 250 mm x 130 mm. Some further calculations and estimations should be performed to show if such is possible or a longer HEX has to be applied. Heat transfer in a bubbling fluidized bed HEX is rather complex and several heat transfer media would have to be considered, to cover possible AR applications like P2H2P, evaporation and super heating of water, pre-heating of powders to be applied in reactors or even heating of supercritical CO_2 and many more. Unfortunately such calculations and considerations could only partly be performed (for helium as HTF, as utilized with *Frauscher* Stirling engines) within the limits of this work. They are also to be found in **appendix A.1**.

5. Summary and Conclusions

This chapter will finally attempt to as shortly and completely as possible summarize the results and conclusions concerning the work on hand, as it would have been very easy, especially for a reader not familiar with the addressed topics, to be distracted from the most important facts concerning this work. Some conclusions, that have not been drawn to this point will be included. In an attempt to offer better transparency chapters addressed above will each receive a separate section here. As a detailed summary and a conclusion regarding performed simulations have been presented with **section 3.4**, they will not be repeated here. Conclusions, that have not been already drawn will be presented at the end of each section. Moreover a list presenting tasks for future work, that have not or not sufficiently been addressed in this thesis can be found at the end of this chapter. The reader might want to use the embedded links to addressed figures and sections to occasionally refresh her or his memory.

5.1. The Advanced Regenerator - a Project

The German *Renewable Energy Sources Act* of 2000, being later followed by the European Union's *Energy Efficiency Directive* (2012/27/EU) and the resolution of the two-degrees-scenario (2DS) in 2015 encouraging respectively forcing efficiency increases and efforts to reduce emissions on the European energy intensive industries have been declared major motivators regarding improvement of heat recovery and integration in those industries. All of this will have to be achieved, while world wide electrical energy consumption is ever increasing at high rates (**figure 1.2**), thus a grave technological and economical impact is to be expected, no matter if those goals will be actually accomplished or not.

In other words, renewables would have to become more continuously available, reliable and cost efficient, while conventional sources and large consumers (industries) of heat and electricity would need to be more flexible and energy efficient - in turn relieving sources - to overcome this energy revolution. Simple and compact devices like the *Advanced Regenerator* in decentralized setup - being included in every energy- and especially heat-intensive industry, storing heat (or P2H while electricity prices are low) and again returning heat to temporally displaced processes or returning electricity, where heat is not needed - could well achieve that.

Thus process and constructional layouts of that concept called the AR (**figure 1.3**) - a short to long term, low to medium capacity heat storage with fast reaction times, enabling minimal losses, high energy densities, a countercurrent HEX and optional P2H2P operation in combination with Stirling engines - have been performed in this thesis.

Furthermore a method enabling a convenient co-simulation of the *Advanced Regenerator* with a controller script and a CPFD software has been developed. The focus was put on the fluidic, procedural and constructional layout of a test bench geometry for cold experimental validation of the AR concept as well as simulation results and said convenient method for co-simulation enabling future work by colleagues, as a lot of work concerning the final research product of a working hot AR prototype remains to be done. The means for those steps performed were analytic process and thermodynamic rough layout calculations, *Computational Particle Fluid Dynamics* (CPFD) software and the programming languages *Matlab* and *Python* for coding.

A similar technology has been researched and a prototype for bench tests has been developed during the last years at the *Institute for Energy Systems and Thermodynamics* (IET) at the *Technical University of Vienna* under the project title *SandTES* (**figure 1.4**, [3], [4], [6], [7] and [8]). Indeed this masters thesis would not have been possible in the relatively short time period of hardly six months without the preceding hard work of the *SandTES* team.

Thus the *concept*, mostly consisting of a genuine idea and a schematic patent sketch from Dr. Schwaiger (**figure 1.3**), referred to as *Advanced Regenerator* has been transposed into

a *project* and a significant amount of work has been performed on the way to its completion. Nevertheless from the perspective of this thesis it can know be stated that a probably even larger quantum of work remains before the final goal of this project - a fully functional hot prototype demonstrating its qualities - will be achieved. This is partially due to issues regarding the transportation of a fluidized powder into and out of elevated storages located above the level of a fluidized bed heat exchanger that have been discovered and addressed in the process. However a solid foundation for the execution of further partially automated and controlled simulations (co-simulations) incorporating *Matlab* and *Barracuda* and successive cold bench tests has been laid to address those issues and also future problems that might arise.

5.2. Method

Analytic calculations have been performed, primarily concerning the process and constructional AR layout, as the fluidic design of the HEX and hopper geometry concerning the processes taking place in the fluidized domain *inside* the AR are highly complex and could not be addressed with an analytic or known empirical approach. Those very processes are dimensioning necessary fluidization grades FG, pressure gradients Δp and manageable particle mass fluxes Φ_p, as well as the continuous pressure variations above the distributor floors. Those tasks were addressed by utilization of a rather powerful CPFD software referred to as *Barracuda*.

Mathcad calculations are utilized for the determination of some important baseline boundary conditions, primarily regarding the geometry, including a fair amount of educated guesses and experimental values from *sandTES* but also economic positions. From those early assumptions and calculations first simulations have been deduced, validating guesses and experimental values but also step by step enabling the definition of a crude geometry. After achieving said basic geometry first more detailed simulations were performed. Those were subject of the actual concept - the method - to this work: They were monitored by a *Matlab* controller by writing any data of interest to log files with *Barracuda* and then reading those files with *Matlab*. Exchanged data involved: pressures (p) at simulation's pressure

checkpoints, particle volume fractions ($V_{frac} = 1 - \psi$) again from checkpoints and effective particle mass flows from flux planes' set up with *Barracuda*. Thus conditions needed for both the simulation and the *Matlab* calculation (like particle and fluid properties etc.; e.g. for calculation of u_{mf}) had to be exchanged - manually - at least once per simulation. Additionally some parameters like desired pressure gradients, fluidization grades or modes of calculation and output were set by the user.

The controller itself had the tasks of continuously reading and interpreting said data from simulations and given by the user. First the controller read and processed (simple calculations to convert data to needed formats and expressions) the data from said log files and plotted part of the acquired information for the user (most importantly p, V_{frac} and $\dot{m}_p$). Then it calculated u_{mf} from particle and fluid parameters to later translate given FGs into air mass fluxes through distributor floors set in *Barracuda*'s so called *flow boundary conditions* (at the bottom of each AR chamber). The next step performed by the controller was the calculation and setting of *Barracuda*'s *pressure boundary conditions*, defining to be controlled pressures at the top of each AR chamber. Those were derived from the desired pressure gradients set by the user and corrected with varying hopper pressure differences (due to varying fluidized bed levels in the hoppers). Finally the controller wrote the exact simulation time at the start of it's execution to another log file to enable comparison of the current simulation time in Barracuda with the time of the last controller execution for co-simulation.

To enable actual co-simulation, meaning the control of Barracuda by the *Matlab* controller based on above mentioned parameters set by the user a *Python* script then read the current simulation time from a *Barracuda* log and compared it to the time of last execution written by the controller. When a certain ΔT (again given by the user) was exceeded it called *Matlab*, executing the controller, again closed it and then initiated a new read-in of boundary conditions by *Barracuda*. To achieve said co-simulation, this process was repeated continuously. In the case of successful simulation, data like achieved minimum or maximum mass flow respectively thermal power, modified FGs or startup durations were again (manually) passed back to Mathcad for further calculations closing the cycle.

To output data from barracuda many *transient data points* (virtual checkpoints) for volume

fraction respectively pressure logging and several flux planes had to be defined within *Barracuda*. The data points would then directly output V_{frac} and pressure data and the flux planes would output flux data to be multiplied with the matching cross sections later on. As explained above, this data was then written to log files, read by the *Matlab controller* script and processed for rewriting *Barracuda*'s BCs to achieve actual control of the simulation and finally plotted for the user. The relation between hopper (and HEX) pressures has been set up as

$$p_{hopR} = p_{hopL} + \Delta p_{hopL} - \Delta p_{edgeL} - 2\Delta p_{HEX} - \Delta p_{edgeR} - \Delta p_{hopR} \tag{5.1}$$

where p_{hopL} and p_{hopR} represent the pressures at the tops of the storage hoppers measured by the uppermost pressure checkpoints depicted in **figure 3.19**. Thus p_{hopL} or p_{hopR} respectively is always to be set to the minimal pressure allowed to occur (p_{min}) in terms of calculating the other. Δp_{hopL} and Δp_{hopR} are the pressure drops in said hoppers' fluidized beds obtained from matching pressure checkpoints. For a pure V_{frac}-control, Δp_{hopL} and Δp_{hopR} would be calculated from mean V_{frac} along the hopper height (e.g. $\Delta p_{hopL} = V_{frac\Delta hL}\Delta h_L(\rho_p - \rho_a)g$). Δp_{edgeL}, Δp_{HEX} and Δp_{edgeR} are the desired gradients set by the user, from left hopper to HEX, from one HEX segment to the next and again from HEX to the right hopper in this order. **Equation 5.1** presents the same pressure gradient Δp_{HEX} twice, though two different values could also be applied.

Unfortunately, at the point said co-simulation was actually achieved and the efficiency of simulations was thus multiplied as they could now run with scheduled BCs and minimal maintenance enabling simulations during nights and over weekends the time assigned to this work had almost run out. It was thus intended to enable further simulations with the presented co-simulation method by successors addressing issues that had not sufficiently been able to be researched within this thesis *before* running the first bench tests. Those issues are again to be shortly addressed below and finally listed in **section 5.4**.

5.3. Layout

The processes and challenges in transposing the knowledge and conclusions achieved to this point into actual constructional cold and hot test bench layouts have been achieved in teamwork of Dipl.Ing. Sulzgruber and the author to this work. The AR's experimental approach will be addressed with a two-phase concept:

- firstly the *cold* trials (approx. 25 $°C \leq T \leq 350$ $°C$) and
- secondly the *hot* trials (approx. 350 $°C \leq T \leq 850$ $°C$).

One major reason for this two step bench layout is, that process factors gauged from the cold test bench will be utilized for the hot bench's final layout, as it will be much more expensive. Thus considerations and calculations dealing with the cold test facility to be manufactured in a near future have accomplished a mostly complete procedural and constructional layout, while the hot prototype's layout has been addressing the most critical components and procedural calculations, that were decided potential financial or procedural bottlenecks only.

5.3.1. Cold Test Rig

The geometry referred to as *essential geometry* (**figure 3.13**) has been realized with welded steel casings flanged together in a way, that accessibility of all crucial parts without significantly altering the interior is possible. It had to be modified to enable a modular construction though. This modular approach is meant to enable maximum flexibility with cold trials as there can be installed three, two or even only one HEX element and none, only one or both fluidized rings in the risers. Flanged HEX segments enable total access to the HEX's transport channel to allow installation of various dummy geometries for tube bundles (**figure 3.11**) or heating rods to test their influence on the inherent flow. Large fittings shaped as beveled boxes might be installed to change the cross section of the channel. Plexi glass windows are located in the upper hoppers and the HEX to enable visual observation. See the **figures 4.1** and **4.2**. Dimensioned drafts are to be found in **appendix**

C. The elongated transition from HEX to riser, needed to gain sufficient space for flange accessibility is important because the risers' distributor floors' fluidization grades (as said section is located outside the HEX) are to be reduced by a factor A_{sim}/A_{test} to achieve the same riser air mass flow $\dot{m}_a$ as applied in the simulations.

Calculations concerning the stability of the cylindrical hoppers taking in account internal pressure and surface load due to the powder fill, steel and especially plexi glass disks under internal pressure and the conical transition from riser to hopper under internal pressure and powder load were performed by Dipl.Ing. Sulzgruber. The standards DIN EN 1991-4:2010-12 and DIN EN 13445-3:2015-12 have been applied. All of above-mentioned elements' thicknesses were shown to be more than sufficient with the only exception of the plexi glass windows, which were dimensioned with a thickness of $s_{plexi} = 20\ mm$.

The distributing elements, enabling homogeneous fluidization would have to provide a pressure loss higher than any pressure variation occurring above, while prohibiting particles from intrusion and potentially clogging. That problem had already been addressed during *SandTES*' layout process. The solution were sheets of sintered metal, as they are available with various thicknesses, porosities and even as sintered tubes (for the fluidized rings in the risers). Sintered metal sheets were also applied as particle filters to protect the pressure control valves. Detailed views of sintered elements are shown with **figure 4.3**. Distributing elements' pressure drops Δp are to be calculated with *minimal* volume flows, as they are needed to enable homogeneous air flow at any state. A formula offered by the elements' manufacturer and distributor *GKN Sinter Metals* was utilized. The particle filters before pressure control valves in the air outlet streams were chosen with a porosity of 20 μm, as only about 5 % of applied representative quartz particles are smaller than this (**figure 2.3**) and pressure losses were to be kept in check. The blower planned for application with the AR is an *AERZEN Delta Blower G5 Type: GM 10 S* with a nominal flow and pressure difference of 810 kg/h respectively 500 $mbar$.

A rule of thumb for the necessary pressure loss of a distributor floor is 20 to 40 % of the vertical pressure difference over the fluidized bed's height. A second approach enabling a comparison was needed and at this stage the only possibility to receive such were simulations. Several simulations incorporating above mentioned quartz sand were scanned for

occurring pressure fluctuations across the distributor floors. **Table 4.1** shows a comparison of necessary pressure drops derived from both methods.

Hoses, pipes, sensors and valves had to be considered and arranged in a P&I diagram to realize boundary conditions regarding flow and pressure set in *Barracuda*. As every chamber's fluidization and pressure control was planned to be realized separately to achieve maximum flexibility in the cold trials a control valve had to be applied for every such boundary condition. Furthermore all pressure checkpoints depicted in **figure 3.19** had to be realized via absolute pressure sensors and additional sensors in every windbox and also directly above every distributor floor had to be applied to monitor the distributing elements' pressure drops. To measure air volume flows, rotameters would have to be installed before any air in- and after every air outlet valve to monitor fluidization grades and pressure control. Additional temperature (thermocouples) and pressure checkpoints were necessary before any air in- and after every air outlet valve to obtain thermodynamic states of the measured volume flows, enabling the calculation of mass flows. A bypass (to the environment) before the inlet valves was implemented. The P&I diagram is depicted in **figure 4.5**.

The measurement of particle mass flows along the HEX was decided a challenge, as precise results would demand very expensive optical methods, leaving only primitive alternatives focused on gauging hopper levels and potentially precise but complicated and susceptible solutions including weighing of hoppers to deduce transported particle mass. A solution including height scales realized with equidistant steel baffles arranged opposite to the hoppers' plexi glass windows was planned. This solution is far from perfect and a more sophisticated, still inexpensive method is needed.

The throttle valves were defined by giving a K_{vs}-value representing maximum air flow and a minimum K_v-value representing minimum flow. A formula given by *Samson* ([11]) has been applied for calculation. To find necessary K_{vs}- and minimum K_v-values, minimum and maximum values for both pressures and mass flows had to be considered. Mass flows were easily deduced from nominal point FGs and desired variations including a safety for unpredicted variations. Resulting mass flows were shown with **table 4.2**. Minimum and maximum occurring air flows and pressures with resulting K_{vs}-values were shown with **table 4.3** for an exemplary temperature of 60 $°C$.

It should be considered to buy control valves with an especially large range of possible K_v-values respectively control ranges (like 5 or even 2 to 100 % K_{vs} respectively 1/20 or even 1/50) though, as it would be very reasonable to try for maximum flexibility regarding a range of powders possible to be fluidized with the AR cold testing bay considering associated investments.

A procedural calculation was performed to gauge overall process parameters. The maximum utilizable hopper volume was calculated to $V_{hopper} \approx 0.6\ m^3$ and a reasonable HEX powder volume (including lower risers) would be $V_{HEX} \approx 0.09\ m^3$. Stated volumes yielded a dead volume respectively mass percentage of about 13 %. The derived masses for quartz sand were $m_{hopper} \approx 750\ kg$ and $m_{HEX} \approx 110\ kg$. For corundum powder they were $m_{hopper} \approx 1300\ kg$ and $m_{HEX} \approx 200\ kg$.

Utilizing corundum powder minimum respectively maximum mass fluxes of $\Phi_p \approx 40\ kg/m^2s$ and $\Phi_p \approx 300\ kg/m^2s$ were achieved in *Barracuda*. With a tube bundle blocking 33 % of the HEX's cross section matching mass flows of $\dot{m}_p \approx 0.9\ kg/s$ and $\dot{m}_p \approx 6.5\ kg/s$ were obtained. Minimum and maximum duration of transport calculated to $t_{min} \approx 3.3\ min$ and $t_{max} \approx 25\ min$. As the hot prototype is planned and calculated for hot and cold hopper temperatures of $T_h = 850\ °C$ and $T_c = 650\ °C$ theoretical maximum heat stored ($Q_{stored} = m_{hopper} c_p \Delta T$) thermal powers of the HEX ($P_{th} = \dot{m}_p c_p \Delta T$) can be deduced for both the cold and the hot test rig. Corundum's heat capacity is derived from a polynomial. Maximum heat to be stored was thus calculated to $Q_{stored} \approx 90kWh$ and the minimum and maximum thermal powers were $P_{th-min} \approx 212\ kW$ and $P_{th-max} \approx 1.6\ MW$.

Utilizing quartz sand, minimum respectively maximum mass fluxes of $\Phi_p \approx 23\ kg/m^2s$ and $\Phi_p \approx 170\ kg/m^2s$ were derived. Resulting mass flows of $\dot{m}_p \approx 0.5\ kg/s$ respectively $\dot{m}_p \approx 3.8\ kg/s$ were calculated. The minimum and maximum duration of transport calculated to $t_{min} \approx 3.3\ min$ and $t_{max} \approx 25\ min$. Maximum heat stored and thermal powers of the HEX were $Q_{stored} \approx 48kWh$ and $P_{th-min} \approx 116\ kW$ respectively $P_{th-max} \approx 870\ kW$. A thermal power range of $P_{th-min}/P_{th-max} \approx 13$ % to 100 % has been deduced. *Mathcad* calculations underlying above stated values can be found in **appendix A**.

The auxiliary power consumption for the AR is gauged by calculating the isentropic (and

adiabatic) power consumption of a compression of an ideal gas, as the compressor power needed for fluidization represents the major part. Isentropic auxiliary compressor power during start-up thus calculated to $P_{s.start} \approx 1344\ W$. An isentropic nominal compressor power of $P_{s.nom} \approx 1400\ W$ was derived. Both are conveniently low, which is an essential advantage of the AR concept and they would be even lower at actual operating temperatures, as needed fluidization air to realize the same state of fluidization decreases with rising process temperature and dynamic air viscosity μ_a respectively falling u_{mf} and ρ_a.

5.3.2. Hot Test Rig

Again a modular construction was applied to enable high flexibility. The biggest differences to the cold test rig were the very large hoppers and a longer HEX, consisting of at least 5 segments (**Figure 4.6**). Larger hoppers enable realistic transport and storage durations (of 8 h plus) and associated heat losses. A functional tube bundle to test heat exchange with various heat transfer media wold have to be included. A construction to enable application of resistive heating elements would have to be designed to test electric heating of applied powders. The hot test rig would have an insulated footstep of about 6500 mm x 3500 mm. The hot P&I diagram would be quite similar to the cold one with the exception of additional recuperators, transferring the waste heat from air leaving the AR with air entering the AR. Sintered elements would be almost identical to those shown with the cold test rig. Resistive heating Rods for the hot rig were decided not critical, as they are available in many variations for reasonable prices. The hot gas valves were decided a potential (economical) bottle-neck. Another additional component was the thermal insulation expected to play a critical role for the AR's overall feasibility.

The hot test rig would have to enable stable fluidization not only at operating temperatures but also while starting up cold. This meant an even wider range of air mass flows and especially small flows at the maximum temperature. Resulting mass flows and FGs were shown with **table 4.5** for an exemplary riser base fluidization control valve. The lower K_{vs}-values, that would be needed were already aproaching a purchasable minimum for this temperature range. Actual layout calculations for all valves would be performed, when cold

trials are running and results regarding fluidization grades and to be applied powders can be deduced. Control valves being able to precisely adjust very low mass flows between 60 $°C$ and (estimated) 550 $°C$ for fluidization valves respectively 850 $°C$ for pressure control valves were realized to represent high tech equipment and thus very expensive. A large control range of roughly 1/20 would be needed if only quartz sand was to be fluidized. K_{vs}-values again obtained exemplarily for riser bases' control valves were presented with **table 4.6**.

There were found only two suppliers offering valves enabling needed mass flows and control range for the desired temperature span. One was quickly eliminated because their valves were currently not built small enough and the only price that was received from them were 24500 *Euro* for one such valve. The other supplier - *Cera Valve* - had the additional benefit of ceramic fittings for their ball valves offering advanced wear resistance in combination with small particles and genuine thermal shock resistance. Those valves would enable a maximum temperature of 950 $°C$, but would additionally need a special profile ceramic ball to enable precise control of minimum $\dot{m}_a$. One such valve would cost roughly 11000 *Euro* (including a motor-actuator), a price that might endanger the whole AR project's feasibility, as a minimum of 3 such valves would be needed (and a maximum of more than 5, if HEX segments were to be controlled separately).

Ways to reduce the hot gas valves' prices were thus considered. For example a recuperation of hot air *before* pressure control valves could cool down the gas temperature below 550 $°C$. A setup with two stage recuperation and a schematic sketch of an improvised low cost recuperatorhas been shown in **figure 4.7**. The air for fluidization would have to be compressed before heating as the exergy demand of a cold compression is significantly lower. A combined LT-recuperator would then exchange remaining heat left in the hot air stream leaving the pressure control valves with the compressed air for fluidization. Recuperation was decided necessary to improve the AR's exergy balance. Generated savings (with 550 $°C$ max. valve T compared to 850 $°C$) would be at least $2000 - 2500$ *Euro* per valve due to cheaper steel and potentially significantly more applying a less expensive ceramic material (e.g. ZrO_2).

As maximum (and even minimum) design bed temperatures applied in this work are high, thermal insulation is another critical parameter regarding the hot test rig's layout. A

minimum cylindrical hopper insulation layer thickness of $s_{cyl} \approx 474\ mm$ has been calculated (see **appendix A.3**). For the bottom and cover of the hopper a minimum layer of 563 mm would have to be applied. Associated high temperature hopper heat losses were $\dot{Q}_{loss} \approx 6200\ W$, resembling a specific loss of $\dot{q}_{loss} \approx 161\ W/m^2$.

This approach might be too simple though, because the outer layers of the cylindrical bulk hopper fill itself would represent additional layers of insulation, as soon as the hopper's steel wall's temperature (and subsequently the outer bulk's temperature) would fall below the temperature of its core. The heat conductivity λ_{bed} of this bulk has been expected to be low, as it forms a porous medium consisting of greater than 50 % air. A method for calculating λ_{bed}-values were found with the *VDI Heat Atlas* [16]. A basic version of the model of *Zehner*, *Bauer* and *Schlünder* was decided sufficiently precise for *mostly spherical* particles in a *packed* bed. When the equations were evaluated for both quartz sand and corundum powder the only disadvantage regarding the utilization of Al_2O_3 with the AR to this point was revealed - the thermal conductivity of a packed bed composed of corundum powder was found to be almost twice the value of the conductivity of a bed of quartz sand. The conductivities for SiO_2 were calculated to $\lambda_{bedSiO2.850°C} = 0.352\ W/mK$ and $\lambda_{bedSiO2.650°C} = 0.285\ W/mK$, while the conductivities of Al_2O_3 were $\lambda_{bedAl2O3.850°C} = 0.663\ W/mK$ and $\lambda_{bedAl2O3.650°C} = 0.513\ W/mK$. **These facts might substantially benefit quartz sand as a storage medium for longer storage durations, as the quartz sand bed's thermal conductivities were found to be only about twice as high as common conductivities of insulations - the bed would be half as good an insulation as the insulation itself. This is a very promising result.**

Another process calculation was performed to gauge overall process parameters for the hot test bench, though several calculated values were identical, because the same HEX segment geometry was applied. Maximum utilizable hopper volume was a lot larger though $V_{hopper} \approx 9\ m^3$ and a reasonable total HEX volume (including lower risers) was found to be $V_{HEX} \approx 0.13\ m^3$. The dead volume respectively mass percentage was calculated to very good 1.5 %. The derived masses for quartz sand were $m_{hopper} \approx 10.1\ ton$ and $m_{HEX} \approx 160\ kg$. For corundum powder the masses were $m_{hopper} \approx 17.7\ ton$ and $m_{HEX} \approx 280\ kg$. The hot prototype is planned and calculated for hot and cold hopper temperatures of $T_h = 850\ °C$

and $T_c = 650\ °C$. Those temperatures are rather high to enable high efficiencies (about 30 %) with state-of-the-art Stirling engines (e.g. produced by the Austrian manufacturer *Frauscher Thermal Motors*) for (P2)H2P applications.

Again taking in account minimum respectively maximum mass fluxes of $\Phi_p \approx 40\ kg/m^2s$ and $\Phi_p \approx 300\ kg/m^2s$ achieved with corundum powder, area mass flows of $\dot{m}_p \approx 0.9\ kg/s$ respectively $\dot{m}_p \approx 6.5\ kg/s$ were obtained. The minimum and maximum durations of transport were $t_{min} \approx 50\ min$ and $t_{max} \approx 5.5\ h$, the maximum heat to be stored calculated to $Q_{stored} \approx 1.3\ MWh$ and the minimum and maximum thermal powers were $P_{th-min} \approx 212\ kW$ and $P_{th-max} \approx 1.6\ MW$.

Utilizing quartz sand, minimum respectively maximum mass fluxes of $\Phi_p \approx 23\ kg/m^2s$ and $\Phi_p \approx 170\ kg/m^2s$ were derived yielding mass flows of $\dot{m}_p \approx 0.5\ kg/s$ respectively $\dot{m}_p \approx 3.8\ kg/s$. The minimum and maximum duration of transport calculated to $t_{min} \approx 45\ min$ and $t_{max} \approx 5.6\ h$. Maximum heat stored and thermal powers of the HEX were $Q_{stored} \approx 650\ kWh$ and $P_{th-min} \approx 116\ kW$ respectively $P_{th-max} \approx 870\ kW$.

With above stated high thermal powers P_{th} and consequent power densities one has to ponder a reduction of it's scale as many decentralized AR applications, for example as a pure heat storage in energy intensive industries or as a thermal battery (P2H2P) with a Stirling, would utilize lower powers. If needed tube bundle (and thus HEX) length for cooling/heating is met the HEX cross section can be reduced to a certain degree, hence reducing overall power and shifting the range of power ($P_{th-min}/P_{th-max} \approx 13$ %) to more feasible areas. *Mathcad* calculations underlying above stated values are found in **appendix A.1**.

5.4. Future Work

Finally a list of important tasks for future work will be presented. This list is separated in three sections: *calculations*, *simulations and trials* and *miscellaneous*. Every section will list tasks in order of decreasing importance.

5.4.1. Calculations

- The geometry of a tube bundle enabling a heat transfer matching the maximum heating respectively cooling power of the HEX should be designed and recalculated for several possible heat transfer media (HTF) to obtain needed tube bundle respectively HEX length in dependance of HTF. Possible AR applications like P2H2P, evaporation and super heating of water, pre-heating of powders to be applied in reactors or even heating of supercritical CO_2 etc. should be covered. A tube bundle for cold bench tests with a geometry enabling later on scale-up of test results and a tube bundle for helium as HTF have been laid out in this work.
- Further considerations and calculations regarding actual transient hopper temperature profiles (preferably in cylinder coordinates) and resulting conductivities and heat losses over time should be performed utilizing the model of *Zehner*, *Bauer* and *Schlünder*. Also the share of heat transfer due to free convection has to be considered (the ideal outcome would be a negligibly small percentage).
- The more complex variations of the model of *Zehner*, *Bauer* and *Schlünder* incorporating more parameters should be utilized to recalculate above-stated thermal conductivities of packed beds to compare values and validate sufficient precision of the basic version regarding AR hopper beds.

5.4.2. Simulations and Trials

- Further simulations and tests should be performed to validate the possibility of fluidization and stable transport of quartz sand by varying hopper geometry and powder properties. If those trials fail, a setup including a *tube 4* geometry (**figure 3.32**) or similar installations in the hoppers should be tested in detail, as this geometry seems to yield the most stable transport conditions to date. A setup with submerged pipes located in *closed* tubes reaching to about one third of the tubes in the hoppers and applying fluidization there, thus disabling a bypass, as shown with **figure 3.33** should also be taken into account.

- As fluidization does significantly influence emptying behavior, this shows up an additional way of controlling hopper outflow besides applied pressure gradients and also restricts hopper fluidization to certain (unknown) values depending on powder properties and desired emptying mechanism. This correlation should thus be investigated in further simulations and bench tests or a way to negate this influence has to be found. The importance of this point could be essential.

- It seems that FGs have to be continuously increased with the level of the to be filled hopper as its fluidization tends to collapse with rising levels. This issue might also be solved by pulsing fluidization air. $\dot{m}_p$ seemed to be not overly influenced by this increase. Nevertheless this should be investigated in further simulations as higher FGs than achievable with currently applied valves might be needed.

- Further simulations and bench tests should inter alia focus on a validation of the possibility of lower mass fluxes and flows, than were achieved in this work, to be performed with the AR HEX.

- Simulations and or experiments with a hopper emptying it's fill into a very large (bottomless) space to see which flow mechanism is formed in dependence of sphericity should be performed to better understand hopper emptying and associated occurrance of what seems like mass flow in *setup 8* simulations utilizing quartz sand.

- Thermal simulations (which will incorporate significantly lower computation rates) including a tube bundle should be performed to learn more about the heat transfer but also the particle mass flow in a hot AR fluidized bed HEX. Know-how from the *sandTES* and especially Dr. Schwaiger might significantly accelerate the process.

- It seems that mass flow rate oscillation along the HEX might be linked to impulsive change of pressure gradients as well as riser bubbling. If that is true, consequentially all adjustments of pressure gradients should be applied in a continuous, smooth manner rather than discrete steps, as have been exercised in most simulations.

- Particle mass flow oscillation in vertical direction while passing through the HEX is suspected to be induced by hopper-HEX transition and HEX-baffles themselves and seems related to (or actually the reason for) vertical mixing and should thus be further

examined in trials and simulations.

- It was observed that a gradient (and subsequent transport) directed from to be fluidized hopper to HEX applied at the right moment can significantly speed up startup durations (≈ -45 %). This was only achieved once but should be tested in the cold trials as it may further improve the AR's flexibility taking in account longer startup times associated with tube-in-hopper setups.

- If the approaches listed above fail, essentially different AR geometries like the setup presented in **figure 3.14** should be tested in further simulations.

- Poles located in the hoppers centres in early simulations seem to benefit transport out of but especially into the hoppers, as the rising particle mass flow circulates and adheres around them forming some kind of more intensly fluidized boundary layer. This phenomenon, if further investigated via simulations could be potentially helpful.

5.4.3. Miscellaneous

- For measurement of particle mass flows a solution including height scales (realized with the help of equidistant steel baffles) arranged opposite to the plexi glass windows included in the upper hoppers is intended. This setup is far from perfect and a more sophisticated, while still reliable and inexpensive method would be direly needed, preferably before the cold test rig is assembled.

- It should be considered to buy control valves with an especially large range of possible K_v-values respectively control ranges (1/20 or even 1/50 of K_{vs}) for test rigs, as it would be very reasonable to try for maximum flexibility regarding a range of powders possible to be fluidized with the AR cold test rig. Minimum K_v-values stated above can be reduced by a percentage calculated from u_{mf} ratios. This will also apply for powders with higher u_{mf} by multiplying K_{vs}-*values* with thus obtained u_{mf} ratios.

- With hot gas throttle valves being very expensive, the AR project's feasibility is endangered. Further ways to reduce the hot gas valves' prices (like the recuperation respectively cooling of hot air *before* pressure control valves suggested above) would

be considerably valuable.

- As the AR will be a very versatile machine further potential fields of application should be pondered and researched in addition to those mentioned in the work on hand, as such applications could be critical for a successful economical implementation.
- The *major challenge* in designing an AR is the difficulty of *transportation into and out of powder storages located above the level of the HEX*, necessary to enable total emptying of those storages. Any ideas in context with this challenge are per se valuable for this project.

Bibliography

[1] International Energy Agency. Energy Technology Perspective 2015. Technical report, IEA, 2015.

[2] International Energy Agency. Energy Technology Perspective 2012. Technical report, IEA, 2012.

[3] K. Schwaiger. A Simulation Tool for a Thermal Energy Storage Based on Sand. Master's thesis, Vienna University of Technology, 2011.

[4] K. Schwaiger. *Development of a Novel Particle Reactor/Heat-Exchanger Technology for Thermal Energy Storages*. PhD thesis, Vienna University of Technology, 2016.

[5] D. Wuensch. *Active Fluidization Storage sandTES: Alternative Speichermedien*. BSc thesis, Vienna University of Technology, 2014.

[6] K. Schwaiger, M. Haider, M. Haemmerle, D. Wuensch, M. Obermaier, M. Beck, A. Niederer, S. Bachinger, D. Radler, C. Mahr, R. Eisl, and F. Holzleithner. sandTES - An Active Thermal Energy Storage System Based on the Fluidization of Powders. *Energy Procedia*, 49:983–992, 2014.

[7] K. Schwaiger, M. Haider, F. Holzleithner, and R. Eisl. sandTES - A novel Thermal Energy Storage Sytem based on Sand. In *Eurotherm Seminar*, number 93, Bordeaux, France 2011.

[8] M. Haider, K. Schwaiger, F. Holzleithner, and R. Eisl. A Comparison between Passive Regenerative and Active Fluidized Bed Thermal Energy Storage Systems. Technical report, Institute of Energy Systems and Thermodynamics, Vienna University of Technology and ENRAG GmbH, 2012.

[9] ed. by Y. Wen-Ching. *Handbook of Fluidization and Fluid-Particle Systems*. New York, NY [a.o.] : Dekker, CRC Press, 2003.

[10] I. E. Idel'čik. *Handbook of hydraulic Resistance*. Boca Raton, Fla. [a.o.] : CRC Press, 1994.

[11] Samson AG. *Arbeitsblatt zur Ventilberechnung - Kv-Wert - Ventilauslegung - AB05*, March 2012.

[12] D. Schulze. *Pulver und Schüttgüter - Fließeigenschaften und Handhabung*. Berlin, Heidelberg : Springer Berlin Heidelberg, 2014.

[13] O. Molerus. *Schüttgutmechanik*. Berlin [a.o.] : Springer, 1985.

[14] V. Sulzgruber. Aufbau einer Mehrbett-Wirbelschicht-Versuchsanlage . Master's thesis, Vienna University of Technology, 2014.

[15] GKN Sinter Metals Filters GmbH. *Filter-Elements - High porosity sintered parts SIKA-R...AX and SIKA-B*, withdrawn, on request.

[16] VDI-Gesellschaft Verfahrenstechnik und Chemieingenieurwesen Verein Deutscher Ingenieure. *VDI Heat Atlas*. Heidelberg [a.o.] : Springer, 2010.

List of Figures

List of Tables

Unfortunately due to reasons of confidentiality the appendices are not available in the public version of this master's thesis. However those chapters can be reviewed at the *Institute for Energy Systems and Thermodynamics* at the *Vienna University of Technology* with the approval of Professor Haider.